

University of California
Santa Barbara

Antimonide-Based Compound Semiconductors for Quantum Computing

A dissertation submitted in partial satisfaction
of the requirements for the degree

Doctor of Philosophy
in
Materials

by

Borzoyeh Shojaei

Committee in charge:

Professor Christopher J. Palmstrøm, Chair
Professor S. James Allen
Professor Arthur C. Gossard
Professor Chris G. Van de Walle

December 2016

The Dissertation of Borzoyeh Shojaei is approved.

Professor S. James Allen

Professor Arthur C. Gossard

Professor Chris G. Van de Walle

Professor Christopher J. Palmstrøm, Committee Chair

August 2016

Antimonide-Based Compound Semiconductors for Quantum Computing

Copyright © 2016

by

Borzoyeh Shojaei

Acknowledgements

First and foremost, I would like to thank my advisor, Professor Chris Palmstrøm. As a mentor Chris teaches by example. His enthusiasm for research never fails to bring him to the lab, and thereby he imparts his knowledge of MBE and UHV to students in a way that could not be done remote from the experiment, in an office. His experience with MBE and insight into its application for studying novel materials has led to an incredible UHV facility, a playground for crystal growth and surface science, and a powerful tool for taking on challenging experiments.

I owe thanks to my committee for their guidance on the work presented in this thesis, for their support in various ways outside of their role as committee members, and also for being great role models. I thank Professor Art Gossard for organizing the weekly MBE meeting, which has allowed me to learn from the work of colleagues and researchers working at the UCSB MBE facilities and has provided a platform in addition to conferences for me to share my work. Professor Jim Allen, like Chris, enjoys the experimental setting for a good portion of any given day, and I was fortunate to use a cryostat in a facility where Jim was often present and always happy to share his insights regarding an experiment. I thank Professor Chris Van de Walle for three terrific courses, and for teaching me to always strive for deep theoretical understanding.

My first day as a graduate student, Dr. Brian Schultz introduced me to Chris's lab. My first experiment was conducted with Brian's help. My first chamber maintenance (and many more thereafter) was guided by Brian. His presence during the first two years was critical to both maintaining the experimental equipment and breaking ground on experiments that would be built upon into the work that is in this thesis.

I thank John English for helping out for the Palmstrøm crew on top of everything else that needed to be done.

I have had the pleasure of working with great fellow Palmstrøm and MBE former and present group members. Their friendship and collaboration makes the lab a fun place to be: Anthony McFadden, Sahil Patel, Mihir Pendharkar, Joon Sue Lee, Jason Kawasaki, Rachel Koltun, Javad, Shabani, Trevor Buehl, Anthony Rice, Nate Wilson, Alex Young, Ken Ohno, Anthony Megrant, Jacqueline Hall, Alex Kozhanov, Shinobu Ohya, Qi Hu, Sean Harrington, Jay Logan, Dan Pennachio, Tobias Brown-Heft, Anisa Myzaferi, Steve Brown, Hong Lu, Shawn Mack, Alan Liu, Justin Norman. I thank the many people who were involved in the move of the lab from Minnesota to UCSB. Much of the system was in place when I joined. It was a pleasure to work with several visiting master's and undergraduate researchers over the years: Asbjørn Drachmann, Marlee Motes, Gerard Leyva, Ryan McMorris, and Eric Ling.

I thank Professor John Martinis, Dr. Pedram Roushan, and Dr. Peter O'Malley for their collaboration on the Station Q projects which broke ground on experiments that would be built upon into the work that is in this thesis.

I thank Professor Peter Krogstrup for teaching me about VLS nanowire growth, and for many fun evenings and insightful discussions.

I thank Tim Murphy, Ju-Hyun Park and Glover Jones at the National High Magnetic Field Lab for running and maintaining the DC Field facility, and Tony, Mihir, Joon Sue and Javad for many fun evenings at the facility.

I thank Professor David Awschalom for providing me access to his group's PPMS and for Dr. Andrew Yeats for training me to use and maintain the instrument.

Much of the work in this thesis was enabled by support from the staff in the California NanoSystems Institute, the Materials Research Lab, the UCSB Nanofabrication Facilities, and the Physics Department machine shop. I owe them my thanks.

I thank Dr. Neil Dilley at Quantum Design for providing me with materials necessary to build a custom probe for a PPMS free of charge, except for my sharing the design of

the probe.

Microsoft and IARPA have funded this work, and they each had organized a series of program reviews that gave insight into what problems needed to be pursued. I thank Professor Chetan Nayak and Dr. Roman Lutchyn of Station Q, who have been great collaborators and mentors.

I thank Ian Walton, Dr. Bill Doering, and Dr. Michael Natan who were great mentors at Cabot prior to my arriving at UCSB, and who, thereafter, continued to be great part-time mentors and passed along interesting projects now and then, until CSMI was shipped off to Europe.

I thank my family for their support over the years: my mom, Nooshin, my dad, Hamid, and my brother Radoyeh. I thank the Lauer family and my fiancée, Emily, for their love and encouragement. I thank my grandparents EN and HZ for their support from afar.

Curriculum Vitæ

Borzoyeh Shojaei

Education

PhD in Materials, 2016
University of California, Santa Barbara
Advisor: Christopher J. Palmstrøm

BSc in Mechanical Engineering, 2007
University of California, Berkeley

Professional experience

Cabot Security Materials Inc.
Research and Development, part-time, July 2010 - January 2013
Mountain View, California USA

Cabot Security Materials Inc. (*Formerly Oxonica Materials Inc. and Oxonica Inc.*)
Research and Development, July 2007 - July 2010
Mountain View, California USA

Publications relevant to this thesis

B. Shojaei, A. P. McFadden, J. S. Lee, M. Pendharkar, M. E. Flatté, and C. J. Palmstrøm, *Materials considerations for forming the topological insulator phase in InAs/GaSb bilayers* (in preparation)

B. Shojaei, A. C. C. Drachmann, M. Pendharkar, D. J. Pennachio, M. P. Echlin, P. G. Callahan, S. Kraemer, T. M. Pollock, C. M. Marcus, and C. J. Palmstrøm, *On the limits to mobility in InAs quantum wells with nearly lattice-matched barriers* (in preparation)

B. Shojaei, P. J. J. O'Malley, J. Shabani, P. Roushan, B. D. Schultz, R. M. Lutchyn, C. Nayak, J. M. Martinis, and C. J. Palmstrøm, *Demonstration of gate control of spin splitting in a high-mobility InAs/AlSb two-dimensional electron gas*, Phys. Rev. B 93, 075302 (2016).

B. Shojaei, A. Mcfadden, J. Shabani, B. D. Schultz, and C. J. Palmstrøm, *Studies of scattering mechanisms in gate tunable InAs/(Al,Ga)Sb two dimensional electron gases*, Appl. Phys. Lett. 106, 222101 (2015).

Other publications

J. Shabani, A. P. McFadden, B. Shojaei, and C. J. Palmstrøm, *Gating of high-mobility InAs metamorphic heterostructures*, Appl. Phys. Lett. 105, 2014 (2014).

C. L. Zavaleta, B. R. Smith, I. Walton, W. Doering, G. Davis, B. Shojaei, M. J. Natan, and S. S. Gambhir, *Multiplexed imaging of surface enhanced Raman scattering nanotags in living mice using noninvasive Raman spectroscopy*, Proc. Natl. Acad. Sci. U.S.A. 106, 13511 (2009).

Patents

B. Shojaei and G. H. Chan, *Nanoparticle separation methods and compositions*, U.S. Patent US20120132570 A1, publication date May 31, 2012

Abstract

Antimonide-Based Compound Semiconductors for Quantum Computing

by

Borzoyeh Shojaei

Quantum information science has made significant progress over the last several decades, but the eventual form a quantum computer will take has yet to be determined. Several physical systems have been shown to operate as quantum bits, or qubits, but each faces a central challenge: the qubit must be sufficiently isolated from its environment to maintain quantum coherence while simultaneously having sufficient coupling to the environment to allow quantum mechanical interactions for manipulation and measurement. An approach to achieve these conflicting requirements is to create qubits that are insensitive to small perturbing interactions within their environment by using topological properties of the physical system in which the qubits are formed. This dissertation presents studies on low-dimensional semiconductor heterostructures of InAs, GaSb and AlSb fabricated by molecular beam epitaxy with focus on relevant properties for their utilization in forming a topologically protected (TP) qubit.

The theoretical basis regarding the semiconductor characteristics suitable for realizing TP qubits stipulates the need for strong spin-orbit coupled semiconductors with high carrier mobility. A comparative study of InAs/AlSb heterostructures wherein structure parameters were systematically varied led to a greater understanding of the limits to mobility in InAs quantum wells. Magnetotransport measurements using a dual-gated device geometry and a comparison of experiment to models of carrier mobility as a function of carrier density were used to identify dominant scattering mechanisms in these heterostructures.

The development of dual-gated devices and high quality InAs channels with AlSb barriers led to a demonstration of the gate control of spin-orbit coupling in a high mobility InAs/AlSb quantum well in which the gate-tuned electron mobility exceeded $700,000 \text{ cm}^2/\text{V}\cdot\text{s}$. Analysis of low temperature magnetoresistance oscillations indicated the zero field spin-splitting could be tuned via the Rashba effect while keeping the two-dimensional electron gas charge density constant.

Findings from the work on InAs quantum wells were applied to investigations on InAs/GaSb bilayers, a system predicted to be a two-dimensional topological insulator (TI). The temperature and magnetic field dependence of the resistance in dual-gated InAs/GaSb heterostructures gate-tuned to the predicted TI regime were found consistent with conduction through a disordered two-fluid system. The impact of disorder on the formation of topologically protected edge states and an insulating bulk was considered. Potential fluctuations in the band structure for realistic levels of disorder in state-of-the-art heterostructures were calculated using a gated heterostructure model. Potential fluctuations were estimated to be sufficiently large such that conduction in the predicted TI regime was likely dominated by tunneling between localized electron and hole charge fluctuations, corresponding to a symplectic metallic phase rather than a topological insulator. The implications are that future efforts must address defects and disorder in this system if the TI regime is to be achieved.

Contents

Curriculum Vitae	vii
Abstract	ix
1 Materials Aspects of Quantum Information Processing	1
1.1 Why a <i>Topological</i> Quantum Computer?	2
1.2 Molecular Beam Epitaxy: An Enabling Technology	4
1.3 Heterostructures and Quantum Confinement	9
1.4 Energy Landscapes at Ever Finer Scales	13
1.5 The Contents of This Thesis	15
1.6 Permissions and Attributions	17
2 Growth of AlSb, GaSb, InAs, and Their Heterostructures by Molecular Beam Epitaxy	20
2.1 A Historical Perspective	20
2.2 An Overview of the Structures Studied in this Thesis	22
2.3 The Growth of an InAs/GaSb Interface Studied by Scanning Tunneling Microscopy	33
3 The Electronic Properties of InAs, GaSb, and AlSb Heterostructures	38
3.1 The Electronic Structure of InAs/GaSb/AlSb Heterostructures	38
3.2 Spin-Orbit Coupling in Two Dimensional Electron Systems	42
3.3 Two-Dimensional Carriers in Magnetic Fields	43
4 Scattering Mechanisms and the Limits to Mobility in InAs Quantum Wells with Nearly Lattice Matched Barriers	45
4.1 The effect of dislocations on the transport properties of InAs quantum wells	46
4.2 On the Limits to Mobility in InAs Quantum Wells with Nearly Lattice Matched Barriers	58
4.3 Acknowledgements	75

5	Gate Control of Spin Orbit Coupling in a High Mobility InAs Quantum Well	76
5.1	Introduction	77
5.2	Executive summary	79
5.3	Results and discussion	79
5.4	Conclusion	92
5.5	Acknowledgements	93
6	Materials Considerations for Forming the Topological Insulator Phase in InAs/GaSb Heterostructures	94
6.1	Introduction	95
6.2	Executive Summary	96
6.3	Results and Discussion	96
6.4	Conclusion	108
6.5	Acknowledgements	108
7	Concluding Remarks and Outlook	109
7.1	A Summary of This Work	109
7.2	Future Work	110
A	Calculating Mobility in InAs Quantum Wells	113
A.1	Section Title	113
B	MBE Apparatus and Several In-situ Techniques	118
B.1	Overview of the III-V VG V80H	118
B.2	Installation of a 2" substrate manipulator	119
B.3	Finding small leaks	120
B.4	Installation of the valved-cracker source for antimony	122
B.5	A note on outgassing cells	123
B.6	Integrated MBE and characterization facility	123
C	Device Fabrication on InAs/AlSb/GaSb Heterostructures	124
C.1	Fabrication of dual-gated devices by optical lithography	124
D	Cryogenic Measurements	129
D.1	A custom probe for a Quantum Design PPMS	129
D.2	Adiabatic demagnetization refrigeration for mK measurements	134
E	Analysis of Shubnikov de Haas oscillations.	136
E.1	Fourier analysis of Shubnikov de Haas oscillations	136

F	Growth of GaAs/AlGaAs Two-dimensional Electron Systems for Quantum Computing Applications	138
F.1	The growth and transport properties of GaAs/AlGaAs heterostructures for spin qubits	138
G	Material Parameters for Band Structure Calculations	141
G.1	Band parameters	141
	Bibliography	143

Chapter 1

Materials Aspects of Quantum Information Processing

Quantum information science has made significant progress over the last several decades, but the eventual form a quantum computer will take has yet to be determined. Several physical systems have been shown to operate as quantum bits, or qubits, but each faces a central challenge: the qubit must be sufficiently isolated from its environment to maintain quantum coherence while simultaneously having sufficient coupling to the environment to allow quantum mechanical interactions for manipulation and measurement. An approach to achieve these conflicting requirements is to create qubits that are insensitive to small perturbing interactions within their environment by using topological properties of the physical system in which the qubits are formed. This dissertation presents studies on low-dimensional semiconductor heterostructures of InAs, GaSb and AlSb fabricated by molecular beam epitaxy with focus on relevant properties for their utilization in forming a topologically protected qubit.

1.1 Why a *Topological* Quantum Computer?

Quantum information science predicts that harnessing quantum phenomena such as superposition and entanglement to process information will enable calculations believed to be impossible for ordinary computers [1]. The potential for significant impact of a quantum computer for real-world applications is due to this advantage over select but critical problems. Many encryption algorithms would be vulnerable because of a quantum computers ability to break large numbers into their component factors in a reasonable length of time[2]. Quantum computers can better simulate quantum systems[3]. The ability to simulate quantum phenomena would increase the predictive powers of simulations of materials and chemical reactions to great benefit for a broad range of fields, including facilitating the discovery new chemical compounds, or the discovery of more energy efficient chemical processes for the manufacture and processing of materials.

The key to a quantum computers ability over that of the ordinary computer is it operates on information represented as quantum bits, or qubits, instead of bits. An ordinary computer's bit can either be 0 or 1, and the machinery in the form of transistors within microprocessors enforces the bit's behavior. The qubit, until it is read, exists in a superposition of the state 0 and the state 1, which means it is part 0 and part 1 with some weighting, and the weighting determines the probability of measuring 0 or 1 when the qubit is read. Quantum algorithms are designed assuming that qubits can be created and allowed to quantum mechanically interact with each other.

Qubits are typically made of certain quantum properties of particles such as individual ions or electrons whose physical locations can be controlled. In such forms, a qubit's superposition states are fragile, and in environments where a useful number of qubits can be created and allowed to interact, they can be disrupted by unintentional interactions with their environment. This process is known as decoherence and is a hur-

due to the implementation of semiconductor spin qubits and superconducting qubits, two quantum computation platforms that promise scalability. Much effort has been spent on minimizing the interactions of the qubits with their environment, and in systems where interactions could cause errors in qubit readings at a rate of less than about 1 in 10,000 error correction procedures can be implemented to correct for the decoherence of individual qubits. In this case, multiple physical qubits are required to represent one logical qubit that can be relied upon to participate in a computation[4].

However, a different approach to building a quantum computer exists. In this approach, the quantum states that make the qubit depend on topological properties of the physical system [5, 6]. Topology is the mathematical study of properties that are unchanged when a system under consideration undergoes smooth deformations. A topological qubit subject to small perturbing interactions with its environment does not alter its state.

The physical systems predicted to have properties that would enable topological quantum computation are certain fractional quantum Hall states [7], a one dimensional semiconductor nanowire with strong spin-orbit coupling in proximity to an s-wave superconductor[8], and a two-dimensional topological insulator in proximity to a superconductor[9]. Each system predicts the formation of quasiparticles useful for playing a part in a topologically protected qubit. Quasiparticles, sometimes referred to as a collective excitations, are entities produced from quantum mechanical interactions among constituents within a microscopically complex system which may hold properties not inherent to the constituents from which they are composed. The quasiparticles that form in the above mentioned systems (when in the right environment, i.e. at low temperature and/or in a finite magnetic field) are nonabelian anyons, meaning the wavefunctions of the quasiparticles pick up a complex phase when the particles are moved around one another, and the order in which they are moved matters. Each system is physically made of, in

part or in whole, heterostructures, or heterogeneous semiconductor structures built from two or more different semiconductors [10]. This thesis addresses the properties of the semiconductor heterostructures required for realizing the latter two proposals for creating topologically protected states of matter.

1.2 Molecular Beam Epitaxy: An Enabling Technology

Control of the microstructure and in turn electronic energy levels in heterostructures can be achieved to a high degree of precision using various crystal growth techniques [11], the most accurate of which is molecular beam epitaxy, or MBE for short. MBE is performed in the lowest achievable pressure environment, and current vacuum technologies achieve routine system pressures in the ultra-high vacuum (UHV) range, or pressures lower than 10^{-9} mbar. Within this environment, Fig. 1.1, molecular beams of constituent atoms are directed toward a substrate. The mean free path of a gas molecule in this environment is of the order of forty thousand meters, and therefore, gaseous atoms and molecules traveling as a molecular beam one meter from their heated Knudsen cells to the substrate undergo no interactions or collisions with each other or residual impurity gases. Interactions and chemical bonding take place on the substrate.

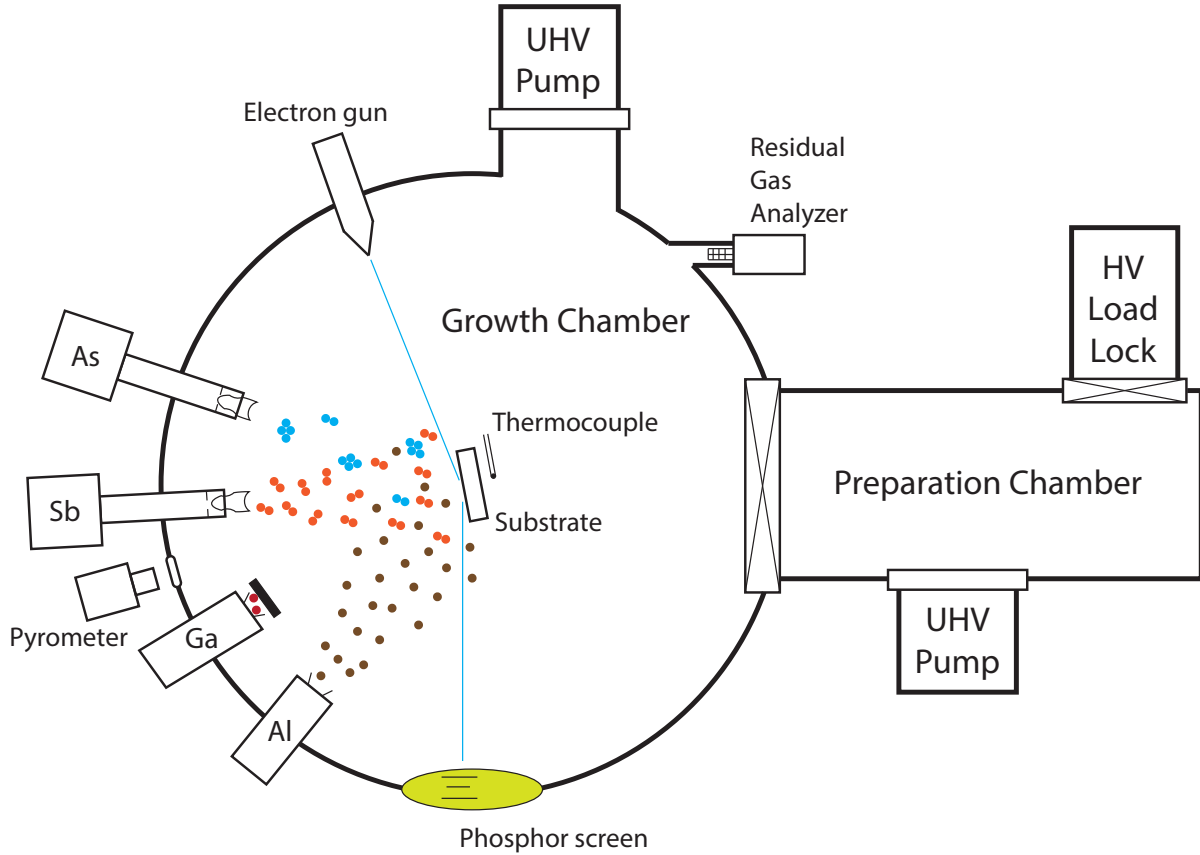


Figure 1.1: A schematic of a molecular beam epitaxy (MBE) system.

The substrate is typically a single crystal foundation upon which subsequent crystals are grown. The subsequent crystals are referred to as epitaxial layers and often maintain a well defined relation to the crystal structure of the substrate. In epitaxy of GaSb, atomic Ga and molecular Sb_2 beams condense from the vapor phase on a heated substrate of single crystal GaSb to form solid, crystalline $\langle \text{Ga}_{0.5}\text{Sb}_{0.5} \rangle_c$ (using Kubaschewski's notation[12]). Condensation of the vapor into other condensed phases such as a $\{\text{Ga}_{1-x}\text{Sb}_x\}$ liquid phase or an alternative solid phase, $\langle \text{Ga}_{1-x}\text{Sb}_x \rangle_\alpha$, must be avoided. Avoiding such condensation can be accomplished if the two-phase mixture $\langle \text{Ga}_{0.5}\text{Sb}_{0.5} \rangle_c$ and the gas phase, $(\text{Ga}_{1-x}\text{Sb}_x)$, minimizes the molar Gibbs free energy. MBE is thermodynamically favorable if it occurs at an overall system composition,

temperature and pressure for which the equilibrium mix of phases is $\langle \text{Ga}_{0.5}\text{Sb}_{0.5} \rangle_c$ and $(\text{Ga}_{1-x}\text{Sb}_x)$. This defines the MBE “growth window” [13].

The constituents of the molecular beams become adatoms as they condense on the substrate, Fig. 1.2a. As adatoms on the surface they migrate for a time scale set by surface energetics before re-evaporating or minimizing their free energy by crystallizing into the zinc blende structure, Fig. 1.2b, set by the GaSb substrate. Growth kinetics are adjusted by changes in the substrate temperature and atomic fluxes, and can be set such that adatoms are sufficiently mobile to find their lowest energy configuration in an atomic layer-by-layer process, such as the step-flow or island growth modes [14].

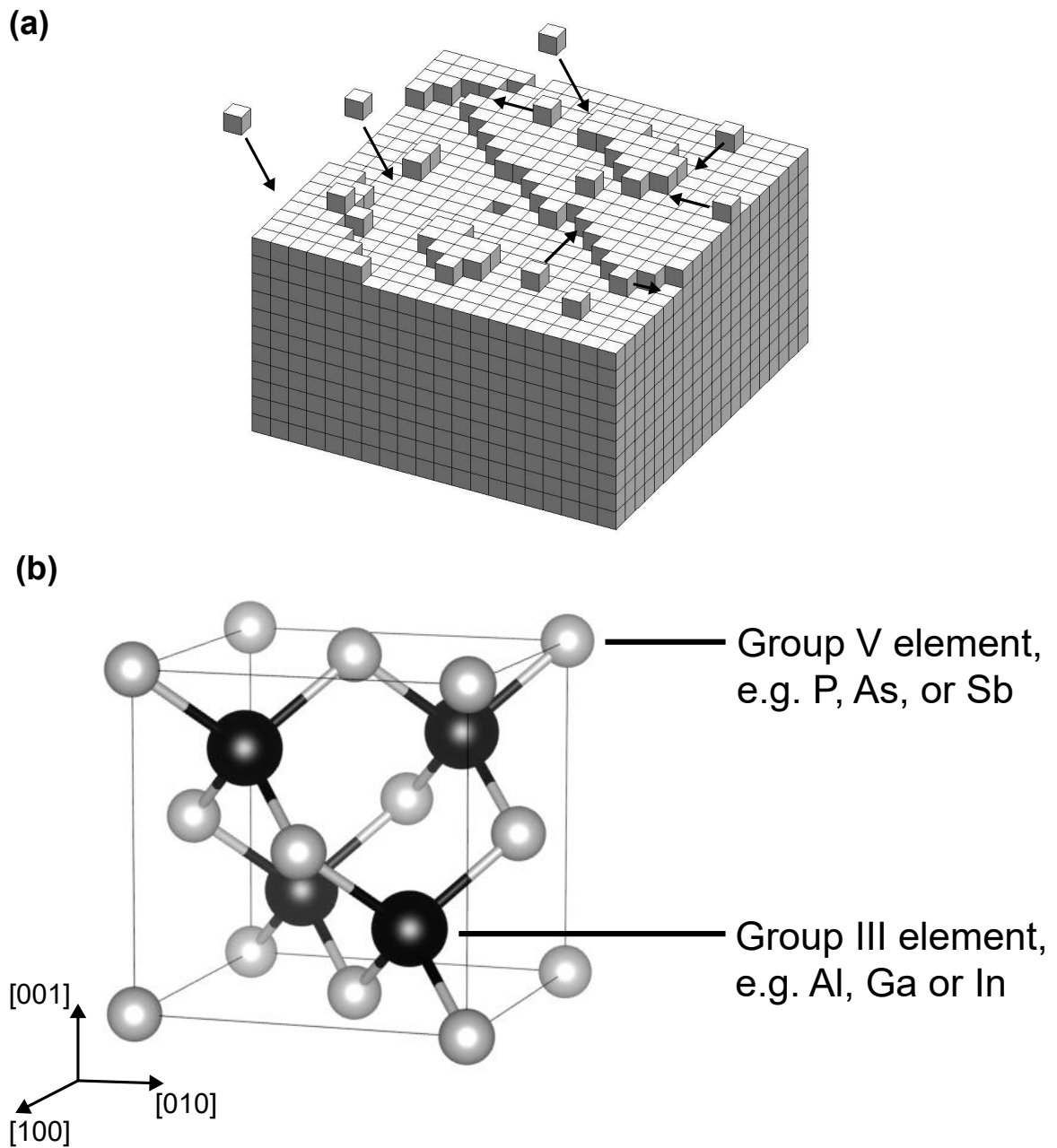


Figure 1.2: (a) Model of layer by layer crystal growth. (b) The conventional unit cell of the zinc blende crystal structure.

The free surface typically exhibits a surface reconstruction in which the equilibrium positions of the atoms at the surface assume positions and bonding configurations different from that in the bulk. The reconstruction may be determined by reflection high

energy electron diffraction (RHEED), a technique that employs diffraction of grazing incidence electrons to determine the periodicity of the surface atomic structure along crystallographic directions parallel to the electron beam. RHEED provides a qualitative determination of surface roughness and the degree of crystallinity of epilayers. Surface reconstructions are phases governed by thermal and kinetic parameters and provide a means of substrate temperature calibration.

In heteroepitaxy of materials with similar lattice constants and identical crystal structures, such as AlSb and GaSb, heterointerfaces of high crystal quality can be created across which chemical composition may change but crystalline defects are small in number. Crystalline quality can be maintained so long as epilayers are grown below a critical thickness beyond which the strain energy of the film makes favorable the formation of extended crystalline defects to relax the epilayer toward its natural lattice constant. Strain also alters the band-structure with respect to the electronic structure of the relaxed material. Growth rates are measured by RHEED intensity oscillations, and are typically of the order one monolayer (ML) per second. Molecular beams can be shuttered to control thicknesses with sub-monolayer precision.

A critical feature of MBE is the cleanliness of the environment in which crystal growth takes place. Residual partial pressures of atmospherics such as nitrogen, oxygen, water vapor, and hydrocarbons are typically far lower than 10^{-11} mbar, and their unintentional incorporation into the growing crystal is far less than other crystal growth techniques. High purity source materials are necessary to reduce unintentional impurity incorporation.

1.3 Heterostructures and Quantum Confinement

MBE allows routine production of heterostructures where composition changes over atomic length scales. The interface of a heterostructure may serve as a barrier to electrons and/or holes because of the change in band gap and the nature of the band alignments. Semiconductor alloys can have band gaps and alignments spanning their constituent semiconductor components. The band gap, E_g , is plotted against the lattice parameter for several semiconductors and their alloys in Fig. 1.3. The data is taken from reference [15].

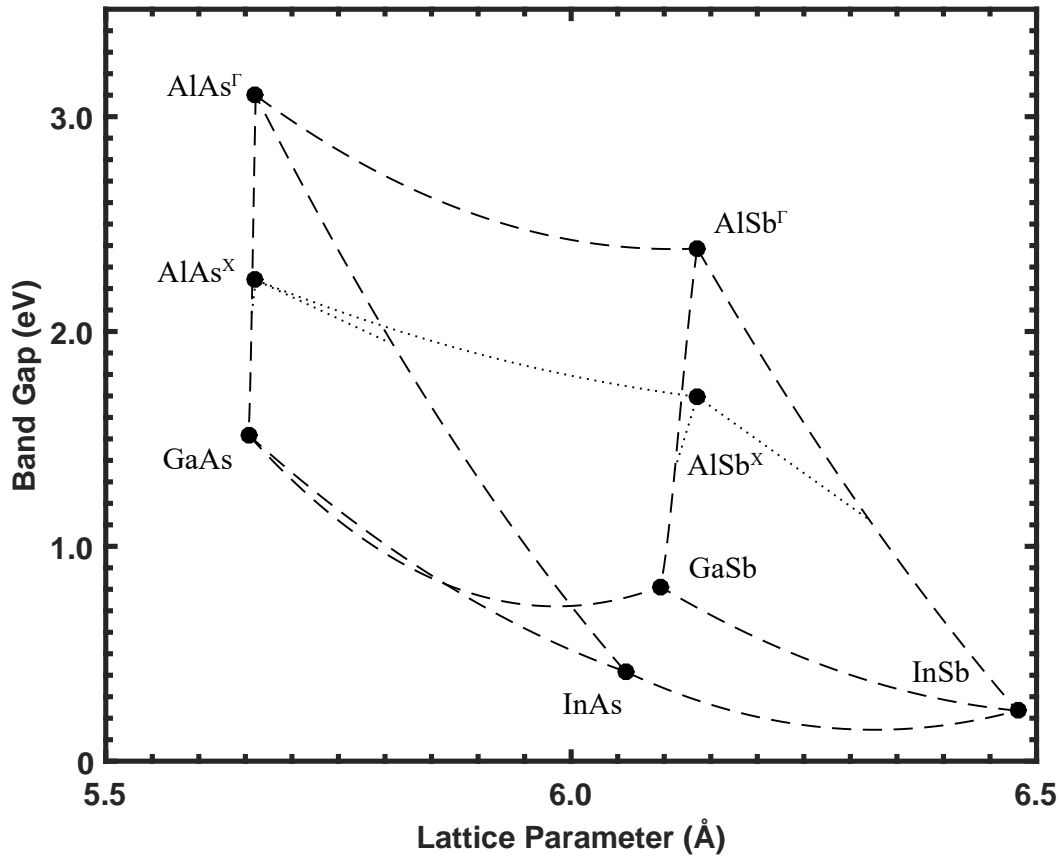


Figure 1.3: Band gap and lattice constants of several compound semiconductors and their ternary alloys. Band parameters were taken from Vurgaftman et al.[15].

The functional dependence of band parameters on chemical composition is not necessarily linear as suggested by Vegard's law. Bowing of band parameters is accounted for in the curves representing the band gaps of semiconductor alloys.

When a thin narrow band gap material is sandwiched between wider band gap materials electrons or holes may be confined within the narrow gap material if the alignment of conduction or valence bands produce a potential well[16]. The carriers become trapped in the confining potential; their motion along the growth direction is restricted and the continuous band is quantized into sub-bands. Their motion in the plane of the well is unrestricted, and they behave two-dimensionally. Quantum wells (QWs) are critical structures in many electronic and opto-electronic devices. They are also important in the field of condensed matter research, where they provide a system in which carrier density, density of states, confinement energy, band structure and spin-orbit coupling can be controlled and modified.

Quantum mechanics predicts the properties of particles confined to quantum heterostructures. Solving the Schrodinger equation for a one dimensional particle in an infinitely deep well of width a produces energy eigenvalues,

$$E_n = \frac{1}{2m} \left(\frac{\hbar n \pi}{a} \right)^2, \quad (1.1)$$

where $m = m^*m_e$, and m^* is the effective mass. In reality confinement potentials have finite barrier heights, as in the case of an AlSb/InAs/AlSb heterostructure, Fig. 1.4a. The confinement potential for electrons is the conduction band offset between InAs and AlSb. The bound-state electron wavefunctions are able to penetrate the finite potential barriers and a change in the energy levels with respect to the infinitely deep well of the same width is observed. The energy levels and wavefunctions are determined numerically by a self-consistent solution of the Schrodinger-Poisson equations [17]. The band edges

and wavefunctions are shown in Fig. 1.4b. The conduction sub-band dispersion relation, Fig. 1.4c, describes the allowed quantum mechanical states as a function of in-plane wavenumber (momentum), $k_{x,y}$,

$$E(k) = E_n + \frac{\hbar^2(k_x^2 + k_y^2)}{2m}, \quad (1.2)$$

for electrons confined in the growth direction but free in the plane of the quantum well.

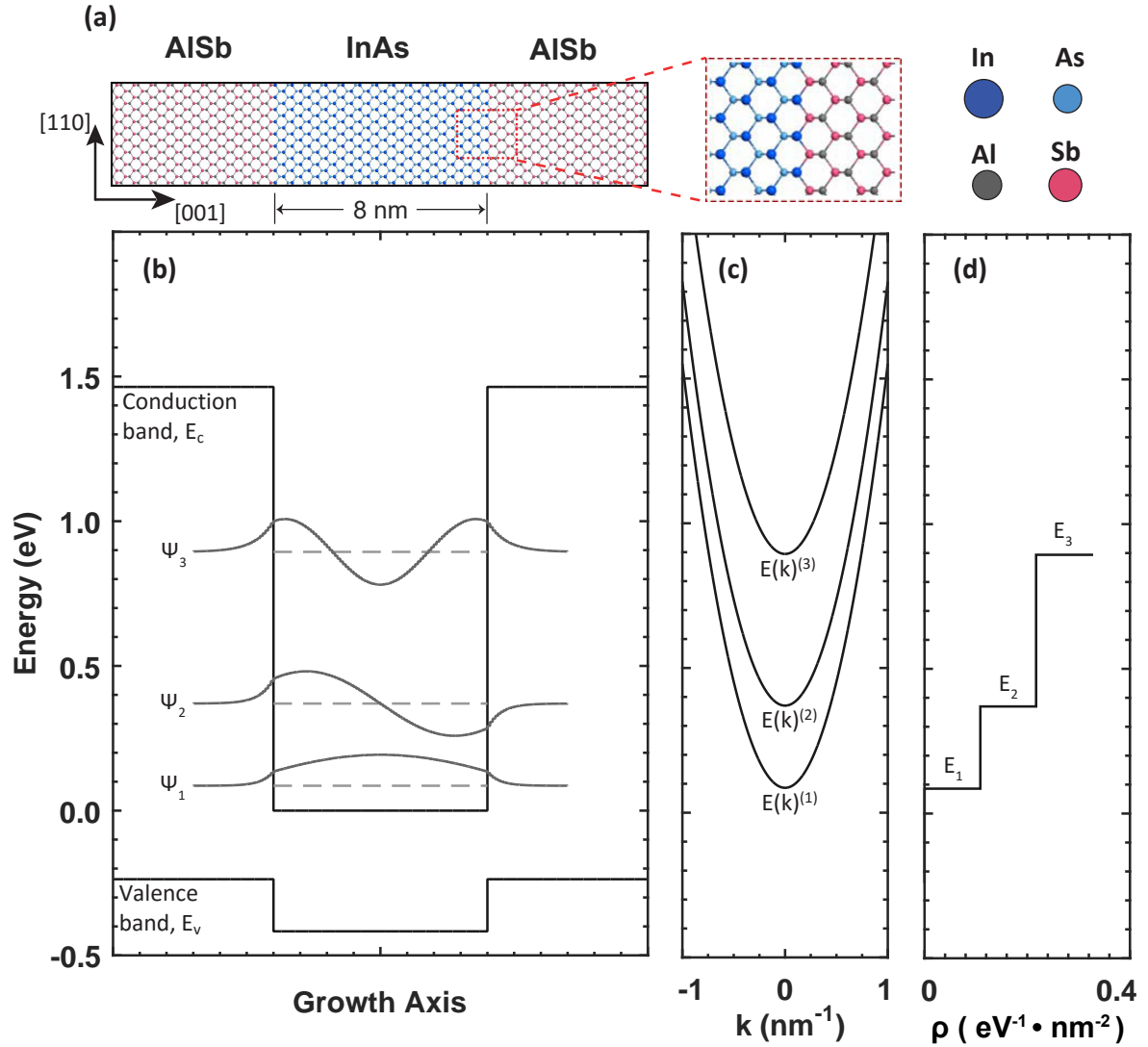


Figure 1.4: (a) An AISb/InAs/AISb heterostructure viewed along the $[110]$ crystallographic direction. (b) The band structure along the $[001]$ growth axis of the heterostructure shown in (a), the bound state energy levels and wavefunctions. (c) The electronic subband dispersion of the bound states (d) The two-dimensional density of states.

Confinement alters the density of states from the parabolic form for three dimensional electrons to a step-like density of electronic states of the form $m/\pi\hbar^2$, starting at E_n , shown in 1.4d. The number of occupied subbands depends of the density of electrons and the temperature.

1.4 Energy Landscapes at Ever Finer Scales

The ability to control the carrier density, density of states, confinement energy, band structure and spin-orbit coupling in heterostructures are critical reasons for their use in creating topologically protected states. Controlling these parameters reduces to controlling the energy level of quantized states and the chemical potential of charge carriers with respect to the energy levels of those states. An example follows illustrating this process.

Heterostructures of InAs, GaSb and an electrically insulating barrier, for example AlSb, are predicted to form a two dimensional topological insulator phase (a quantum spin Hall phase), when the electronic conduction sub-bands in InAs form below the electron valence sub-bands in GaSb. Quantum mechanical coupling between these states result in a hybridization gap in the dispersion, which is spanned by spin-polarized counter-propagating edge states[18]. When the InAs/GaSb heterostructure is made the conduction channel of a dual-gated Hall bar, as shown in Fig. 1.5(a), the sub-band structure and Fermi-level can be independently tuned by the action of the two gates, on which electrostatic potentials are applied relative to the conduction channel.

A measurement of the longitudinal resistance in an InAs/GaSb heterostructure under an applied bias that approximately keeps the sub-band structure constant while changing the Fermi level is shown in Fig. 1.5(b). This structure and additional transport measurements will be discussed in greater detail in Ch. 6. A calculated in-plane two dimensional dispersion and schematic helical edge-states are shown in Fig. 1.5(c). The corresponding two dimensional density of states are shown in Fig. 1.5(d). The colored bars track the approximate position of the Fermi level under applied bias and along the dispersion and density of states.

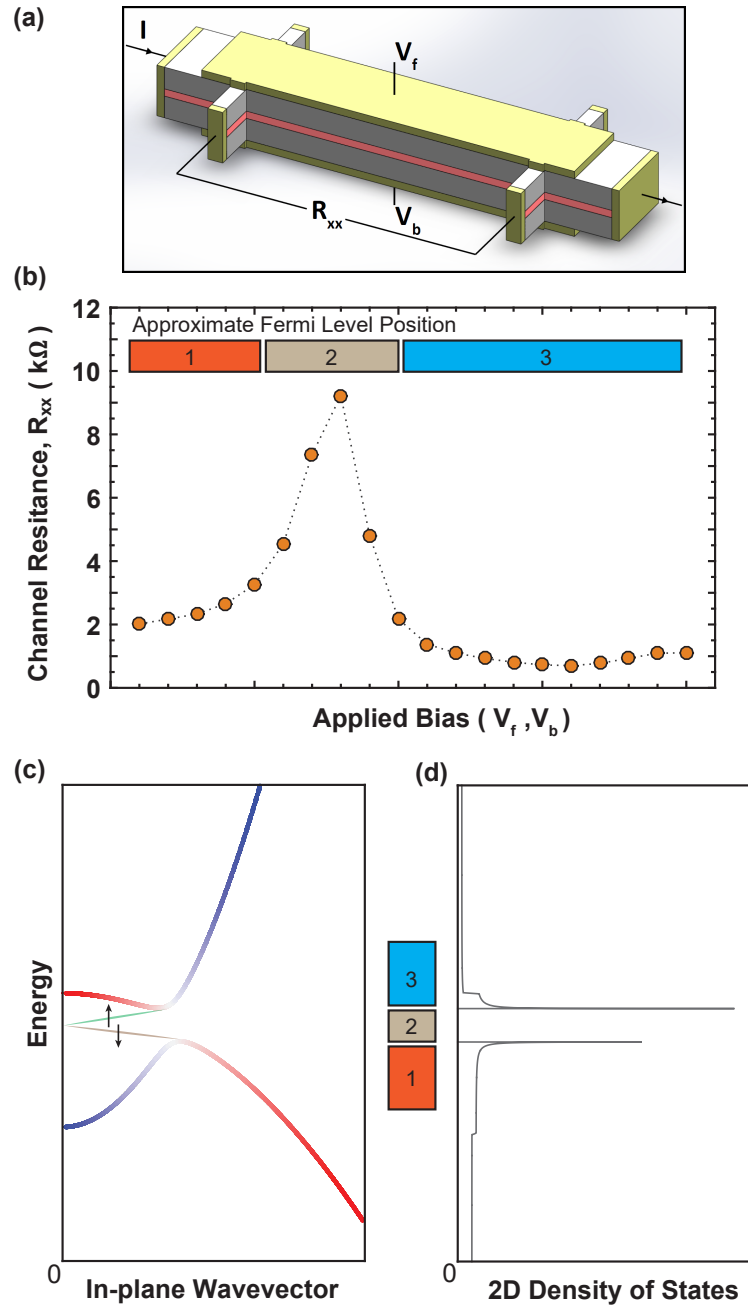


Figure 1.5: (a) The dual-gated Hall bar structure discussed in the text. (b) The channel resistance measured in an InAs/GaSb heterostructure along a line of applied bias by the front a back gate that maintains an approximately constant electric field over the heterostructure but varies the Fermi level. This data will be revisited in Ch. 6. (c) A calculated two-dimensional dispersion of an InAs/GaSb bilayer structure with schematic spin-polarized edge states. (d) The calculated two-dimensional density of states.

Theoretical and experimental estimates of the gap size range between 1-10 meV. To utilize the topologically protected edge states in a topological qubit, the ability to form the hybridization gap and maintain the position of the Fermi level within the gap over device length scales (on the order of 1 μm) must be maintained. In the presence of disorder this is not a trivial task.

1.5 The Contents of This Thesis

In Ch. 2 an introduction and review of the growth of InAs, AlSb and GaSb based heterostructures by molecular beam epitaxy is presented. The focus is on structures for quantum transport applications. Some experimental results are presented in the context of the growths and heterostructures used in the later chapters.

In Ch. 3 the electronic structure of the heterostructures is discussed, as well as the impact of defects on electronic properties and the application of these heterostructures for their use in topological qubits. Spin orbit coupling in InAs quantum wells is introduced, as is electron-hole hybridization and the predicted topologically insulating (quantum spin Hall insulator) phase in InAs/GaSb bilayers.

The primary results of this thesis are in Ch. 4, 5 and 6 wherein investigations of mobility limiting defects in the heterostructures, the control of spin orbit coupling in InAs/AlSb quantum wells, and the impact of defects on the formation of the topological insulator phase and an insulating bulk in gate-tunable InAs/GaSb bilayers are presented.

In chapter 4 scattering mechanisms and the limits to mobility in InAs quantum wells are investigated by a comparative study of heterostructures with varying threading dislocation densities, well thicknesses, and interface growth procedures, and modeling the dependence of mobility on carrier density for individual scattering mechanisms. Magneto-transport experiments using a dual gated Hall bar device geometry was demonstrated to

be a powerful tool for studying scattering mechanisms in these heterostructures. Dislocations were the dominant scattering mechanism limiting electron mobility in heterostructures grown on lattice mismatched substrates. In heterostructures where dislocation density was low evidence was found for coulomb scattering limited the mobility at low electron density while interface roughness and alloy scattering limited mobility at high electron density and within the first occupied subband.

A demonstration of the gate control of spin-orbit coupling in a high mobility InAs quantum well is presented in Ch. 5. Magnetotransport experiments showed clean Shubnikov-de Haas oscillations down to low magnetic fields, and the gate-tuned electron mobility exceeded $700,000 \text{ cm}^2/\text{V}\cdot\text{s}$. A clear beating effect was observed in magnetoresistance oscillations at large potential asymmetry between gates. Beat patterns due to zero field spin-splitting and other classes of transverse magnetoresistance oscillations were distinguished by temperature dependent magnetoresistance measurements. Analysis of the magnetoresistance oscillations indicated the zero field spin-splitting could be tuned via the Rashba effect while keeping the two-dimensional electron gas charge density constant.

In Ch. 6 the impact of disorder on the formation of topologically protected edge states and an insulating bulk in InAs/GaSb bilayers is investigated. The temperature and magnetic field dependence of the resistance in dual-gated InAs/GaSb heterostructures gate-tuned to the predicted TI regime were found consistent with conduction through a disordered two-fluid system. The impact of disorder on the formation of topologically protected edge states and an insulating bulk was considered. Potential fluctuations in the bandstructure for realistic levels of disorder in state-of-the-art heterostructures were calculated using a gated heterostructure model. Potential fluctuations were estimated to be sufficiently strong such that conduction in the predicted TI regime is likely dominated by a symplectic metallic phase rather than a TI phase. The implications are that future efforts must address disorder in this system and focus must be placed on the reduction

of defects and disorder in these heterostructures to realize the TI phase.

1.6 Permissions and Attributions

1. Of the content of Ch. 4, one article has previously appeared in the journal Applied Physics Letters in the article titled *Studies of scattering mechanisms in gate tunable InAs/(Al,Ga)Sb two dimensional electron gases* by B. Shojaei, A. McFadden, J. Shabani, B.D. Schultz, and C.J. Palmstrøm.[19]. In this work I planned the study, fabricated the heterostructures by MBE, characterized the morphology and defect densities of the heterostructures by AFM and EPD measurements, fabricated gated Hall bar devices on the heterostructures, performed the low temperature magnetotransport measurements, analyzed the experimental data by calculating the dependence of the mobility on density to determine dominant scattering mechanisms, and wrote the manuscript. I performed magnetotransport measurements using a MATLAB based software package originally developed by A. McFadden and J. Shabani. The article is reproduced here with the permission of the American Institute of Physics: <http://scitation.aip.org/>.

A second article in preparation for submission will appear on the Arxiv in the article titled *On the limits to mobility in InAs quantum wells with nearly lattice matched barriers* by B. Shojaei, A.C.C. Drachmann, M. Pendharkar, D.J. Pennachio, M.P. Echlin, P.G. Callahan, S. Kraemer, T.M. Pollock, C.M. Marcus, and C.J. Palmstrøm. In this work I planned a majority of the study, fabricated all heterostructures by MBE, characterized the morphology and defect densities of the heterostructures by AFM, XRD and EPD measurements, fabricated gated Hall bar devices on samples A, B, C and E, performed the low temperature magnetotransport measurements on samples A, B, C and E, analyzed the experimental data by

- calculating the dependence of the mobility on density and gate voltage to determine dominant scattering mechanisms, and wrote the manuscript. A.C.C. Drachmann fabricated the gated Hall bar device on sample E, performed the low temperature magnetotransport measurements on sample E, and assisted with several AFM measurements. M. Pendharkar assisted with growth calibrations for several of the growths. D.J. Pennachio prepared the TEM specimen on sample D, and D.J. Pennachio and S. Kraemer assisted with STEM measurements. M.P. Echlin and P.G. Callahan assisted with ECCI measurements.
2. The content of Ch. 5 has previously appeared in the journal *Physical Review B* in the article titled *Demonstration of gate control of spin splitting in a high-mobility InAs/AlSb two-dimensional electron gas* by B. Shojaei, P.J.J. O'Malley, J. Shabani, P. Roushan, B.D. Schultz, R.M. Lutchyn, C. Nayak, J.M. Martinis, and C.J. Palmstrøm[20]. In this work I planned the study, carried out all experimental work, analyzed the data, and wrote the manuscript. The foundations for this work began in meetings, held under the guidance of Station Q, in which all co-authors were involved. The experimental progress at the time of these meetings had yielded studies of localization effects in 2DEGs with strong spin-orbit coupling. However, a portion of the framework for the experiments that led to reference [20] was developed in these meetings. The article is reproduced in Ch. 5 with the permission of the American Physical Society <https://www.aps.org/>.
 3. The content of Ch. 6 is an article in preparation for submission and will appear on the ArXiv in the article titled *Materials considerations for forming the topological insulator phase in InAs/GaSb bilayers* by B. Shojaei, A.P. McFadden, M. Pendharkar, J.S. Lee, M.E. Flatté, and C.J. Palmstrøm. In this work I planned the study, fabricated the heterostructure by MBE, fabricated the gated Hall bar

device, performed magnetotransport measurements in a helium-4 cryostat and an adiabatic demagnetization refrigerator, analyzed the data, interpreted the findings by considering disorder in the system, performed the calculations of the potential fluctuations from coulombic disorder, and wrote the manuscript. A.P. McFadden, M. Pendharkar, J.S. Lee and I took additional magnetotransport measurements in a dilution refrigerator and the National High Magnetic Field Laboratory. M.E. Flatté is performing calculations of the variation in the hybridization gap size over space due to interface roughness, and these calculations and the associated text in the manuscript are not included in this thesis.

4. In all other sections, assistance provided by colleagues not mentioned above are acknowledged in figure captions or in the acknowledgment section of the chapter that contained their contribution.

Chapter 2

Growth of AlSb, GaSb, InAs, and Their Heterostructures by Molecular Beam Epitaxy

2.1 A Historical Perspective

The growth of InAs and GaSb by molecular beam epitaxy was pursued early on in the development of MBE[21] and was in part motivated by the prediction of a broken gap band alignment between the two compound semiconductors[22, 23]. Soon after, the determination of the conduction band offset between InAs and AlSb[24] suggested quantum wells in an InAs channel could be formed with large confinement potential AlSb barriers. These properties continue to motivate current fundamental and device research utilizing these materials.

Many early advances in developing InAs/AlSb low-dimensional heterostructures were made by Professor Herbert Kroemer's group at UCSB. They include the development of buffers for growth on mismatched substrates[25, 26], the determination of the mecha-

nisms providing free carriers in un-intentionally doped wells[27], the development of Te-doped heterostructures[28] and other modulation doping techniques[29] for InAs/AlSb heterostructures, the influence of the shutter sequence during the growth of InAs/AlSb interfaces on the electron mobility in InAs quantum wells[29], and optimal well thicknesses for achieving the highest carrier mobility[30].

At around the same period of time, significant advances were made in understanding the subband structure of InAs/GaSb heterostructures. A hybridization gap was predicted (for superlattices[31] and coupled quantum wells[32, 33, 34]) and experimentally confirmed for InAs/GaSb coupled quantum wells[35].

The quantity of work on the 6.1 Å family of materials produced in the 1990s, particularly for applications in quantum transport and superconducting weak links, was not reproduced in the first decade of the new millenia. Recent focus on these materials has been for their application in high speed electronics[36, 37] and optoelectronic devices.

However, the prediction of a quantum spin Hall phase[18] in InAs/GaSb coupled quantum wells and the need for high spin-orbit coupled, low dimensional semiconductors for creating topologically protected qubits has renewed interest in studying these materials.

This thesis adds to the collection of work on heterostructures of InAs, GaSb and AlSb investigations of mobility limiting defects in the heterostructures, the control of spin orbit coupling in InAs/AlSb quantum wells, and the impact of defects on the formation of the topological phase and an insulating bulk in gate-tunable InAs/GaSb bilayers.

2.2 An Overview of the Structures Studied in this Thesis

The structures in the studies presented in chapters 4, 5 and 6 have many similarities. Growth on GaSb:Te (001) substrates is a common trait among those structures with exceptionally high carrier mobility in InAs channels. However, structures grown on GaAs (001) substrates were also studied. This section discusses the growth of these structures and some of their transport properties.

Schematics for three distinct methods of growing a channel material, InAs or InAs/GaSb, on GaAs (001) or GaSb:Te (001) substrates are shown in Fig. 2.1(a), 2.1(b), and 2.1(c). The AlSb/AlAs nucleation layer and antimonide based buffer depicted in Fig. 2.1(a) was based on the growths developed by Nguyen et al.[25] and Thomas et al.[26]. The GaSb interfacial misfit dislocation (IMF) array nucleation was based on the nucleation technique developed by Huang et al.[38]. Growth on GaSb:Te substrates, as depicted in Fig. 2.1(c), will be discussed later in this section.

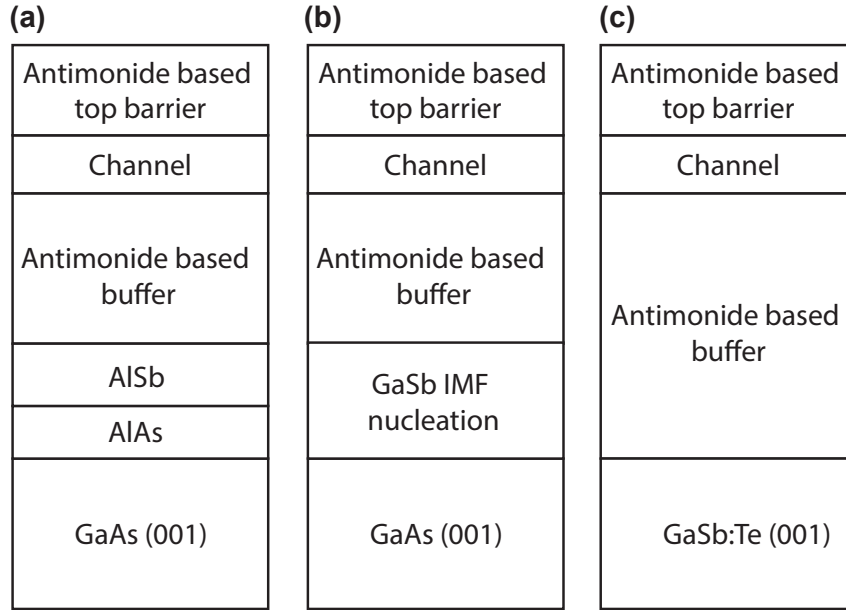


Figure 2.1: Schematics of the antimonide based heterostructures studied in this thesis. (a) A channel with antimonide barriers grown on a GaAs (001) substrate using an AlSb/AlAs nucleation layer. (b) A channel with antimonide barriers grown on a GaAs (001) substrate using GaSb/GaAs IMF nucleation layer. (c) A channel with antimonide barriers grown on a GaSb:Te (001) substrate.

The AlSb/AlAs nucleation technique and IMF nucleation technique were developed by other research groups as methods to reduce the extended defect density in antimonide epilayers grown on GaAs substrates. Early on in the development of AlSb/AlAs nucleation techniques by Thomas and coworkers[26], the dislocation density in the epilayers were estimated by the spiral mound density associated with the subsequent growth of a GaSb epilayer[39]. More recently, the dislocation densities were quantified by transmission electron microscopy[40]. In each case, the lowest achieved estimated dislocation density was on the order of 10^7 cm^{-2} .

These values are in agreement with the spiral mound density measured on films presented in this dissertation where the AlSb/AlAs nucleation technique was implemented with a subsequent 2-3 μm thick antimonide based buffer. A topographic map measured by atomic force microscopy (AFM) of a 1 μm GaSb buffer grown on a semi-insulating

GaAs (001) substrate using an AlSb/AlAs nucleation layer is shown in Fig. 2.2(a).

Qian et al.[41] studied the initial stages of molecular beam epitaxy of GaSb on GaAs(001) substrates and observed the formation of 90° misfit dislocations in growing GaSb islands at the GaSb/GaAs interface with Burgers vector $\mathbf{b} = \frac{a}{2}\langle 110 \rangle$. Also observed were 60° threading dislocations formed predominantly within growing islands, and not at island coalescence; there was no correlation between the threading dislocation density and the GaSb coverage in the initial stages of growth in Qian and coworker's study. The IMF nucleation developed by Huang and coworkers expanded on Qian et al.'s work and was claimed to suppress the extended defect densities propagating toward the surface of subsequent epilayers to $< 10^5 \text{ cm}^{-2}$ [42, 38] quantified by cross-sectional and plan view TEM.

Huang and coworker's procedure for the IMF nucleation technique forces the formation of an optimal IMF array when Sb is exposed to a (4x2) reconstructed Ga-rich GaAs surface. A correlation with a high density IMF array was reported with an observation of a (2x8) reconstruction after Sb was exposed to the Ga-rich GaAs surface[38].

The procedure outlined by Huang et al.[38] for the formation of an IMF array when nucleating GaSb on GaAs was implemented for InAs quantum well heterostructures and GaSb buffers grown on GaAs substrates presented in this dissertation. The surface reconstruction changes observed during the growth of the IMF nucleation layer for structures presented in this dissertation were consistent with those observed by Huang et al. [38]. However, the threading dislocation densities for quantum well structures and GaSb buffers estimated by the spiral mound density measured by AFM were much higher, typically of order 10^7 cm^{-2} , than the densities reported in the original works. It is noted that the surface topography of GaSb buffers grown using the IMF technique was not previously reported in the works of Huang and co-workers[42, 38]. A topographic map measured by AFM of a $1 \mu\text{m}$ GaSb buffer grown on a semi-insulating GaAs (001)

substrate using the GaSb/GaAs IMF nucleation technique is shown in Fig. 2.2(b).

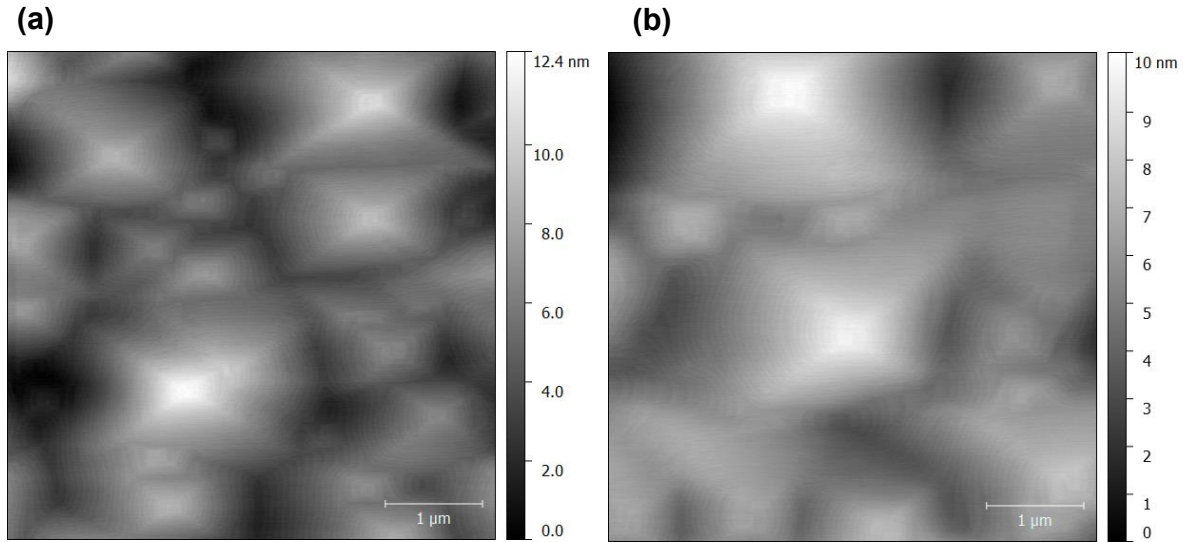


Figure 2.2: (a) Atomic force microscope topographic map of a 1 μm GaSb buffer grown on a semi-insulating GaAs (001) substrate using an AlSb/AlAs nucleation layer. (b) Atomic force microscope topographic map of a 1 μm GaSb buffer grown on a semi-insulating GaAs (001) substrate using a GaSb/GaAs interface misfit dislocation array nucleation layer. The [1-10] directions point approximately along the horizontal axis.

In parallel with efforts toward achieving low dislocation density epilayers on GaAs substrates, heterostructure growth on GaSb substrates was undertaken. Growth on GaSb substrates was historically avoided because semi-insulating GaSb did not (and still does not) exist. However, high aluminum content antimonides grown by MBE are insulating at low temperature, and the development of $\text{Al}_x\text{Ga}_{1-x}\text{As}_y\text{Sb}_{1-y}$ buffers grown on GaSb substrates became a critical factor in the growth of high mobility, dual-gated InAs heterostructures presented in this dissertation. Employing the substrate as an electrostatic gate required overcoming several technical challenges involving appropriate metal bonding techniques for MBE growth and micro-fabrication techniques that prevented the channel from inadvertently shorting to the substrate. These details are discussed in Appendix C. A schematic of a typical InAs quantum well heterostructure on a GaSb:Te

(001) substrate studied in this thesis is shown in Fig. 2.3. Two substrate growth temperature procedures are depicted. The constant substrate temperature procedure was most heavily used. The variable substrate temperature procedure will be discussed toward the end of this section.

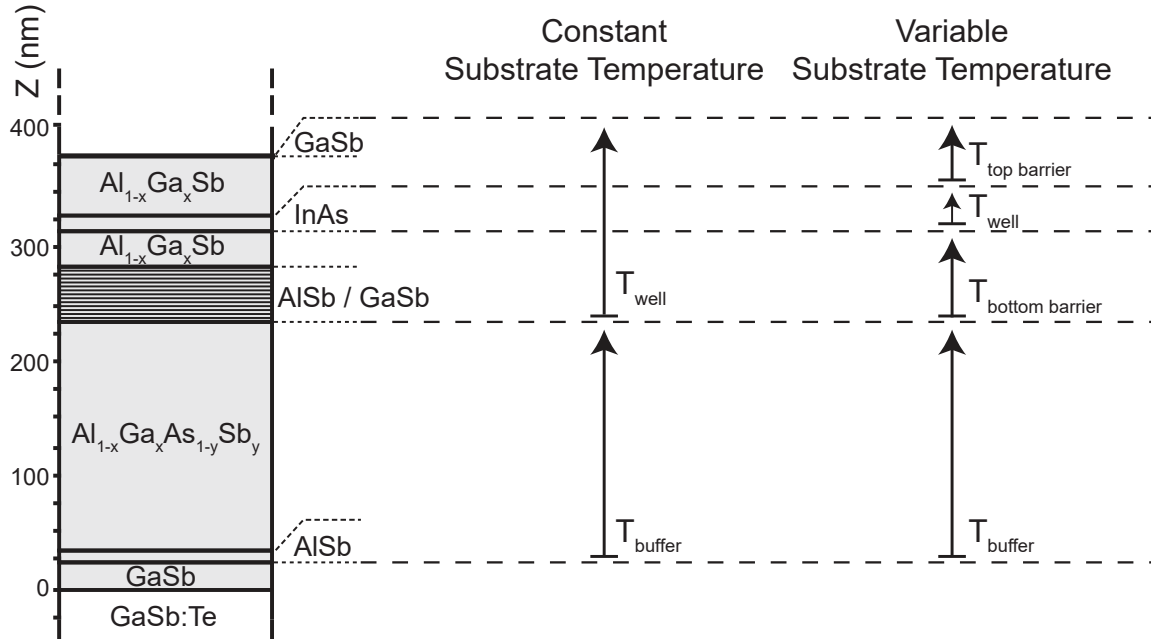


Figure 2.3: A schematic of a typical InAs quantum well heterostructure on a GaSb:Te (001) substrate studied in this thesis and two substrate growth temperature procedures.

By design, the $\text{Al}_x\text{Ga}_{1-x}\text{As}_y\text{Sb}_{1-y}$ buffers were intended to be lattice matched to the GaSb substrate. Ga was occasionally incorporated (i.e. $x < 1$) to enhance the stability of the buffer against oxidation if appropriate passivation techniques were not to be employed during device fabrication. The successful growth of $\text{Al}_x\text{Ga}_{1-x}\text{As}_y\text{Sb}_{1-y}$ buffers is made possible by the nonequilibrium thermodynamic and kinetic processes enabled by MBE, and phase separation can be avoided even inside the calculated miscibility gap[43].

Buffer growths were typically calibrated by adjusting relative beam fluxes during the growth of $\text{Al}_x\text{Ga}_{1-x}\text{As}_y\text{Sb}_{1-y}$, and thereafter, measuring composition by thin film x-ray diffraction. An example calibration curve for $\text{AlAs}_x\text{Sb}_{1-x}$ epilayers grown on GaSb:Te

(001) substrates at 510 °C is shown in Fig. 2.4. It is noted that As_4 beams are not entirely As_4 , and Sb_2 beams are not entirely Sb_2 . In each case, some fraction of the beam is composed of dimeric species and some fraction is tetrameric. The subscript denotes the majority species.

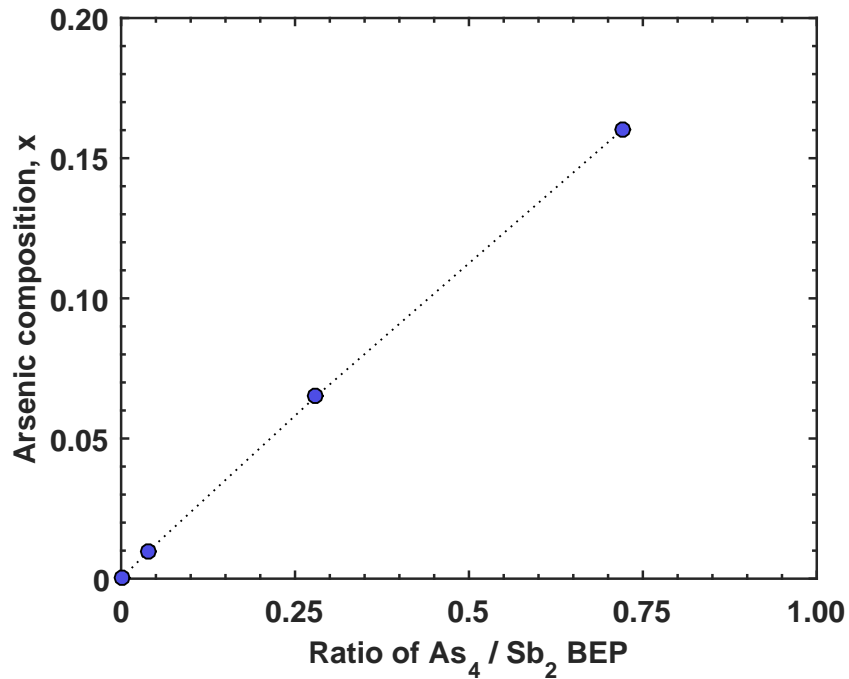


Figure 2.4: The composition x determined by thin film x-ray diffraction of a 500 nm thick $\text{AlAs}_x\text{Sb}_{1-x}$ epilayer, grown over a GaSb:Te (001) substrate at 510 °C, as a function of the As_4 to Sb_2 beam equivalent pressure (BEP) ratio.

A high angle annular dark field (HAADF) scanning transmission electron microscope (STEM) image of an InAs/AlSb/GaSb heterostructure similar to that depicted schematically in Fig. 2.3 along the [1-10] zone axis and in the vicinity of the InAs quantum well is shown in Fig. 2.5(a). This particular growth employed a shutter sequence at the barrier / quantum well interface in which group V and III shutters were simultaneously opened and closed. A higher magnification HAADF-STEM micrograph of the lower interface and upper interface between the barrier and quantum well is shown in Fig. 2.5(b) and

2.5(c), respectively. The 80 nm TEM specimen was prepared using a focused gallium ion beam. The thickness of the sample and the method of preparation make quantitative analysis of the interface between the quantum well and barriers difficult, but analysis of the images suggest the lower interface is smoother than the upper interface, and that each interface observes composition variations of one monolayer in the growth direction over lateral length scales of several nanometers.

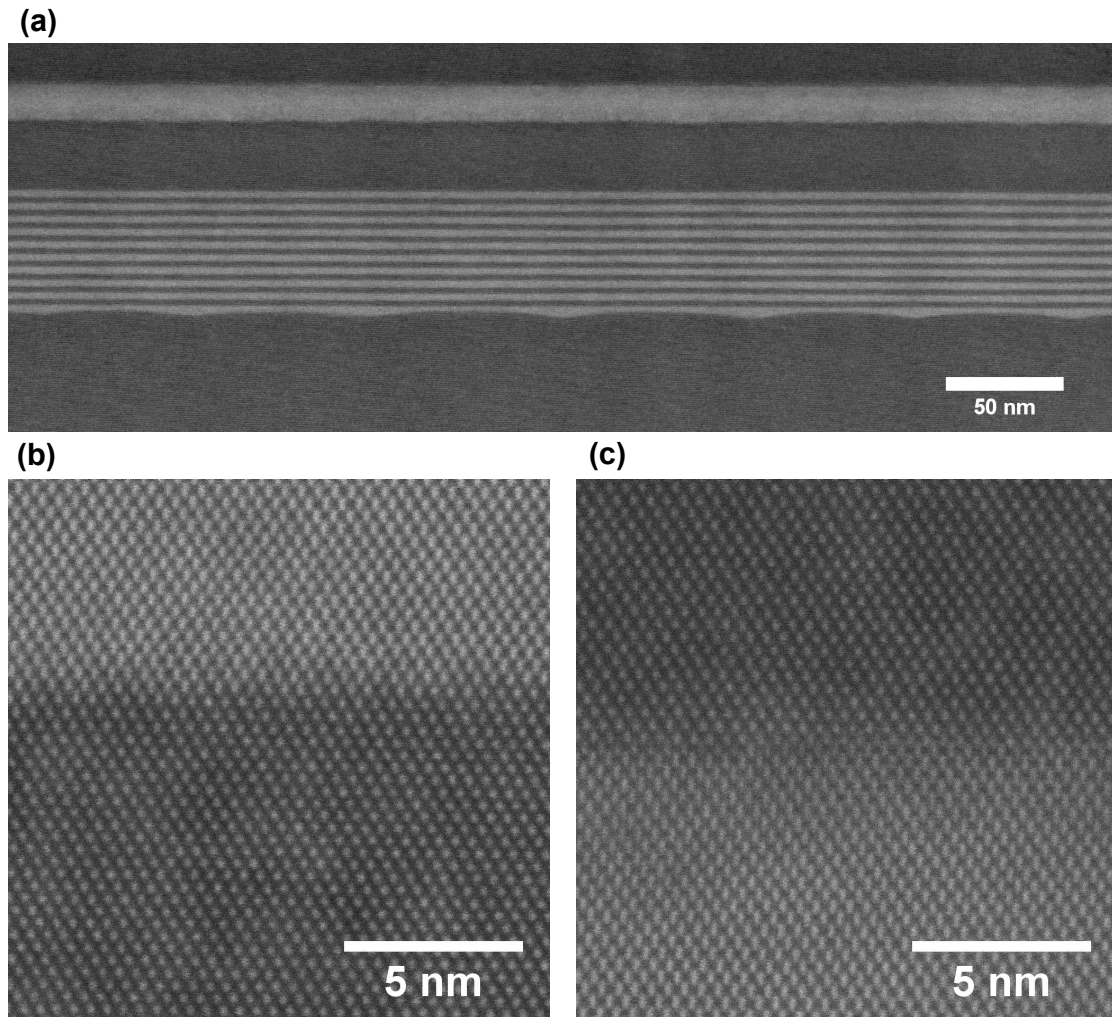


Figure 2.5: (a) High angle annular dark field (HAADF) scanning transmission electron microscope (STEM) image of an InAs/AlSb/GaSb heterostructure along the $[1-10]$ zone axis and in the vicinity of the InAs quantum well grown on a GaSb:Te (100) substrate. The 80 nm thick specimen was prepared by milling a section of wafer using a focused gallium ion beam. (b) HAADF-STEM image of the bottom InAs/AlSb interface. (c) HAADF-STEM image of the top InAs/AlSb interface. Sample preparation was performed by Dan Pennachio. TEM was performed with assistance from Stephan Kraemer and Dan Pennachio.

As noted earlier, of the two substrate temperature growth procedures depicted in Fig. 2.3, the constant temperature growth was most commonly used. The variable temperature growth procedure was motivated by some of the results presented in chapter

4 of this thesis and in some of the techniques used to grow high mobility GaAs/AlGaAs heterostructures discussed in an Appendix F. The constant temperature growth of the barriers and quantum well is a compromise between the optimal substrate temperature for each epilayer. A substrate temperature between 470 °C and 490 °C was found to be optimal for the MBE system used in the studies presented in this thesis as judged by mobility for a given set of beam flux conditions. However, over the course of these studies, improvements in vacuum quality, predominantly by the elimination of breaches in the vacuum system to atmosphere (for example at flange connections or ceramic to metal seals at electrical feedthroughs), colloquially referred to as leaks, and the implementation of appropriate shutter outgassing techniques led to the ability to sustain growth interrupts without impacting material quality. The duration of the interrupt could be adjusted to allow appropriate changes in substrate temperature between the barrier materials and the quantum well.

In Fig. 2.6(a) a topographic map of an InAs quantum well heterostructure grown on a GaSb:Te (001) substrate using the constant substrate temperature procedure is presented. This happens to be the same heterostructure on which HAADF-STEM was performed and presented in Fig. 2.5. In Fig. 2.6(b) a topographic map of an InAs quantum well heterostructure grown on a GaSb:Te (001) substrate using the variable substrate temperature procedure is presented. In this structure, the barriers were grown at a temperature of approximately 515 °C. The higher substrate temperature resulted in a step flow growth mode of the GaSb capping layer.

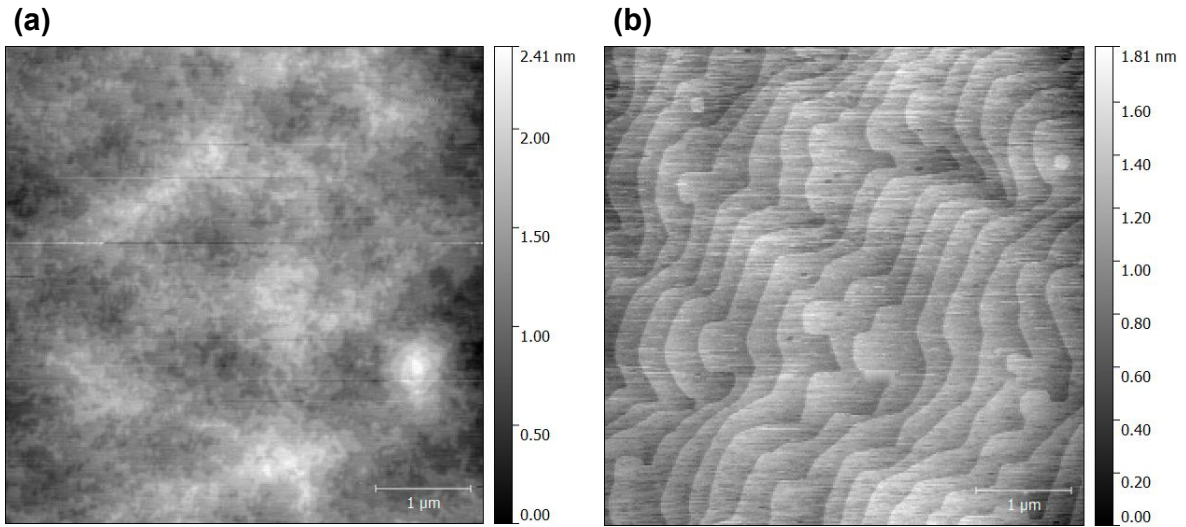


Figure 2.6: (a) Atomic force microscope topographic map of an InAs quantum well heterostructure grown on a GaSb:Te (001) substrate using the constant substrate temperature procedure presented in 2.3. (b) Atomic force microscope topographic map of an InAs quantum well heterostructure grown on a GaSb:Te (001) substrate using the variable substrate temperature procedure presented in 2.3

Transport in structures using the variable temperature growth procedure show promising results. In Fig. 2.7 the mobility as a function of carrier density at a sample temperature of 2 Kelvin for several InAs quantum well heterostructure grown on GaSb:Te (001) substrates using the variable substrate temperature and constant substrate temperature procedures. The data points are labeled by the $\text{Sb}_2\text{:III}$ BEP ratio used for the growth of the antimonide barriers. Several nanometers of the top barrier was grown over the surface of the quantum well layer prior to implementing the upper interface growth interrupt and substrate temperature change.

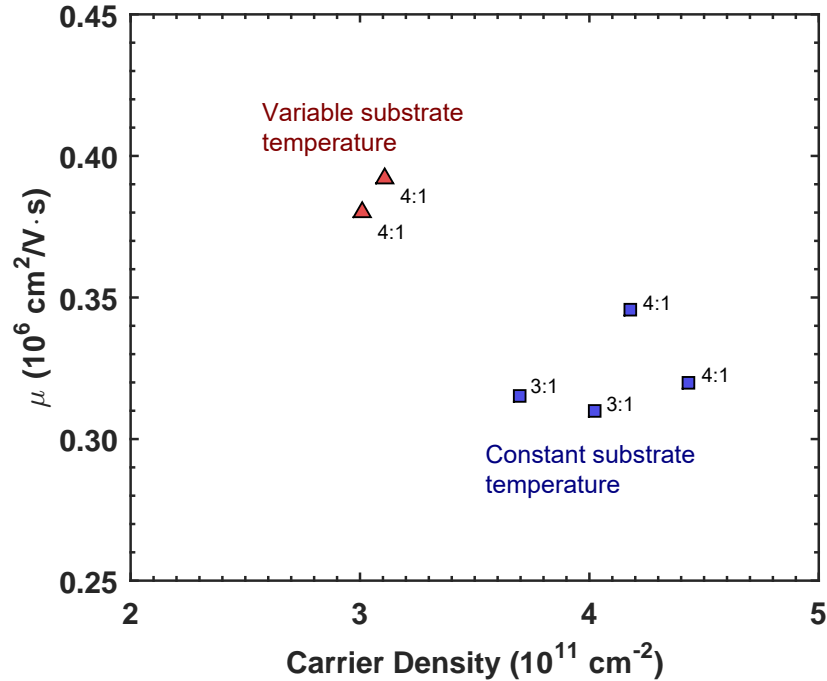


Figure 2.7: Mobility as a function of carrier density at a sample temperature of 2 Kelvin for several InAs quantum well heterostructure grown on GaSb:Te (001) substrates using the variable substrate temperature and constant substrate temperature procedures presented in 2.3. The data points are labeled by the Sb₂:III BEP ratio used for the growth of the antimonide barriers.

The reduction in carrier density and increase in mobility is believed to be statistically significant. The reason for the improved transport properties may be a reduction in intrinsic defect densities due to more optimal growth conditions, and/or a reduction in impurity incorporation due to higher substrate growth temperatures, and/or a smoothing of the quantum well/bottom interface because of the inherent annealing that takes place during the growth interrupt. These results are preliminary and more work is required to verify and understand them. To the author's knowledge, this is the first demonstration of a growth of InAs/AlSb/GaSb heterostructures wherein the barriers and quantum well were grown at different temperatures.

Before proceeding to the next section, the carrier density in the quantum well as a

function of top barrier thickness, Fig. 2.8, is presented. This is more or less a reproduction of the work of Nguyen et al.[27] concerning the Fermi level pinning at the GaSb capping layer. These results are applied to an argument made in chapter 6 concerning the conduction in InAs/GaSb coupled quantum wells.

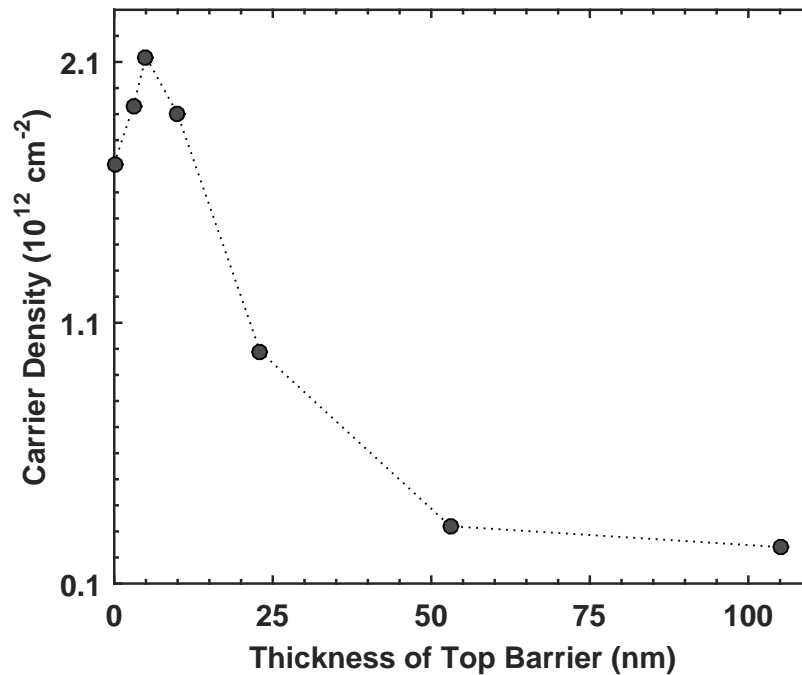


Figure 2.8: Carrier Density as a function of top barrier thickness at a sample temperature of 10 K or lower for several InAs quantum well heterostructures grown on a GaAs (001) substrates.

2.3 The Growth of an InAs/GaSb Interface Studied by Scanning Tunneling Microscopy

An influential experiment performed early on in the development of InAs quantum wells with antimonide barriers was the role the interface plays for the transport properties in the quantum well[29]. In this experiment two shutter sequences were implemented at

the growth of the barrier/quantum well interfaces. The first employed an Sb soak on the bottom barrier followed by a 1 monolayer deposition of indium before the progression of the growth of the InAs quantum well. The top barrier was grown in reverse order. The second terminated the bottom barrier with a 1 monolayer deposition of Al followed by an As soak before proceeding with the growth of the InAs quantum well. The top barrier was grown in reverse order. The conclusions were that the first technique forced the interfaces to be InSb-like and was deemed superior because higher carrier mobility was achieved compared to the second technique in which the interfaces were forced to be AlAs-like[29]. In this section, the interpretation of this result is placed on different grounds compared to what is commonly encountered in literature, for example see reference [44].

A possible explanation for the lower mobility observed in the AlAs-like interface well is that the arsenic soak resulted in significant arsenic over antimony exchange and led to the formation of high extended defect density AlAs nucleating on the AlSb bottom barrier. The original work cites the formation of As_{Al} antisite defects as the source of lower mobility[29]. Furthermore, it should be considered that the interface, even when formed attempting to force InSb-like bonding, may be governed by a universal behavior wherein the chemical profile observes a sigmoidal character[45]. In short, it may be that there is room to improve upon the level of control of growing the InAs/(Al,Ga)Sb interface by MBE, or perhaps the interface will do what it wants to do. A short scanning tunneling microscope (STM) experiment is presented which gives some context for a discussion.

Fig. 2.9(a) presents a topographic map measured by STM of a GaSb (001) surface terminated in a (1x3) surface reconstruction. This surface was returned to the MBE via interconnected UHV transfer chambers. On it, 0.5 monolayers of In was deposited at a substrate temperature of approximately 400 °C. The substrate was quenched immediately after the deposition. The topography was again measured in the STM and is shown in

Fig. 2.9(b). Some features of the step structure were observed to change. Notably, the step edges appeared more disordered. The surface reconstruction remained, but was also observed to be qualitatively more disordered. It appeared the In was incorporated at step edges; no island formation was observed.

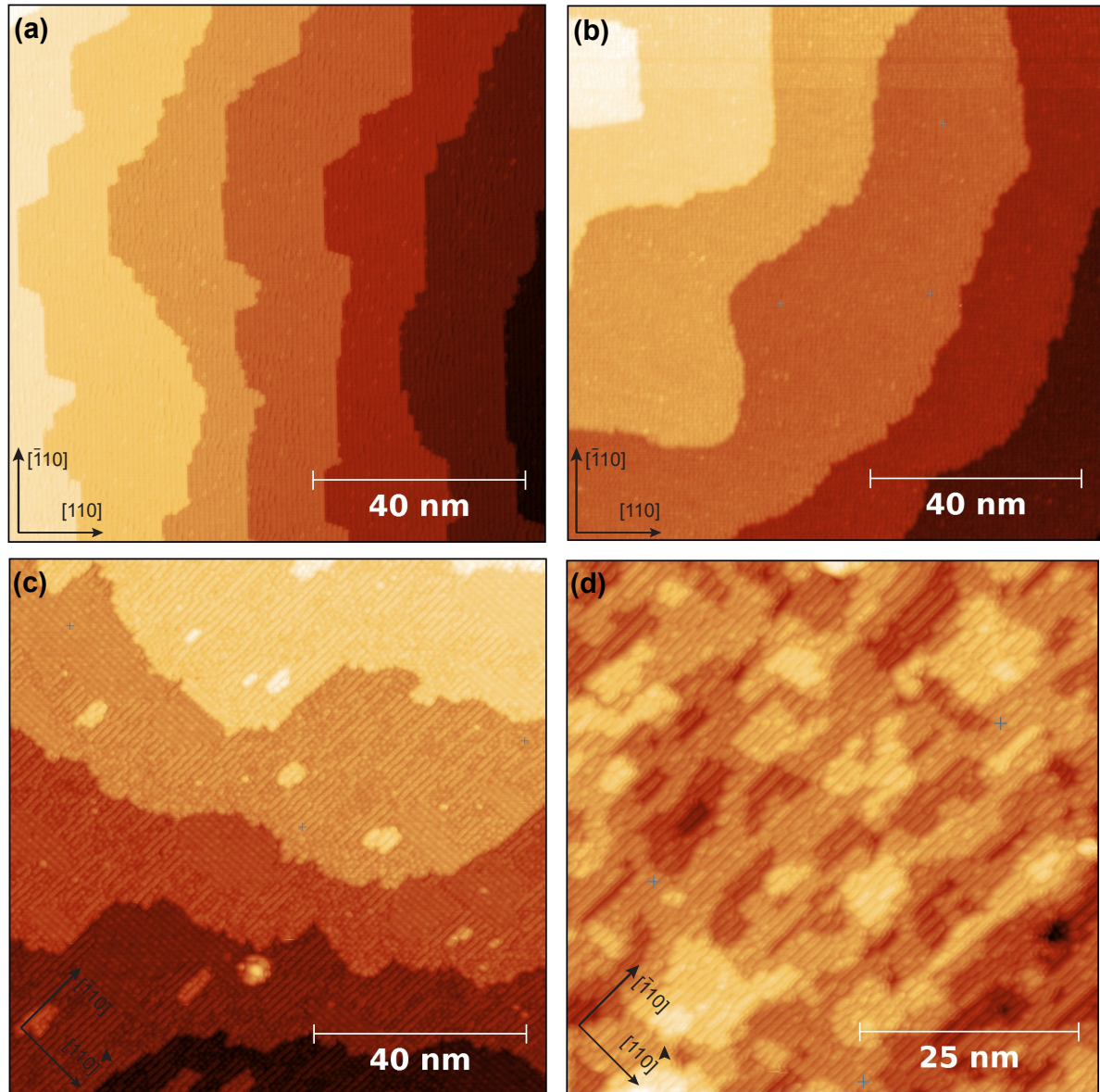


Figure 2.9: (a) Scanning tunneling electron microscope (STM) topographic map of a GaSb (001) surface terminated in a (1x3) surface reconstruction. (b) STM topographic map of 0.5 ML In/ GaSb surface (c) STM topographic map of 1 ML In/GaSb surface (d) STM topographic map of 1 ML InAs/1 ML In/GaSb surface. STM was performed with assistance from Nate Wilson.

The substrate was again returned to the MBE, heated to approximately 400 °C, and an additional 0.5 monolayers of In was deposited. The substrate was immediately quenched after the deposition. The topography measured on this surface, 1 ML In /

GaSb, is shown in Fig. 2.9(c). At this stage, multiple reconstructions and qualitatively more disordered step edges were observed. STM and RHEED indicated the (1x3) surface reconstruction was still dominant. Nucleation of 1 monolayer of InAs followed, and a topographic map of its surface is shown in Fig. 2.9(d). The morphology is indicative of layer by layer growth at a substrate temperature of 400 °C.

The stability of the InSb surface is questionable at what is considered optimal substrate temperatures for InAs quantum well growths. The electron counting model may also be violated in such a surface. The disordered reconstruction observed on the 1 ML In/GaSb surface also may have resulted from erring higher than the intended substrate temperature, possibly placing it above the congruent sublimation temperature of InSb. Further experiments of this sort will be useful in developing a greater understanding of the nature of the interface composition profile in this system and may lead to insights on creating higher quality interfaces. If repeated, it is suggested multiple samples be grown, with each terminated at the surface of interest as opposed to stepping through the interface on a single substrate using multiple depositions.

Chapter 3

The Electronic Properties of InAs, GaSb, and AlSb Heterostructures

In this chapter background is provided on the band alignments of the 6.1 Å family materials, the prediction of a topologically insulating phase in InAs/GaSb heterostructures, spin orbit coupling in two-dimensional systems, and two dimensional carriers in magnetic fields.

3.1 The Electronic Structure of InAs/GaSb/AlSb Heterostructures

The band structure of the 6.1 Å family of compounds make possible the creation of deep quantum wells in InAs channels with AlSb barriers and coupled electron-hole two-dimensional systems by utilizing the broken gap band alignment between InAs and GaSb. A ball and stick model of a AlSb/GaSb/InAs/AlSb heterostructure is shown in Fig. 3.1(a). The band structure along the growth axis for flat band conditions is depicted in Fig. 3.1(b). Quantization along the growth axis leads to the development of a subband

structure for electrons in the InAs channel and holes in the GaSb channel. The relative subband energy levels could be controlled by the degree of confinement (layer thicknesses) or by external electric fields. Another possible method would be to alloy the electron and hole layers. For example, instead of using GaSb for the hole layer, one may use $\text{In}_x\text{Ga}_{1-x}\text{Sb}$. The band would be altered by both a change in the confinement potential, but also by the introduction of strain in the structure by deviating from lattice matching. The subband states can quantum mechanically couple, leading to a hybridization gap when the bands are inverted.

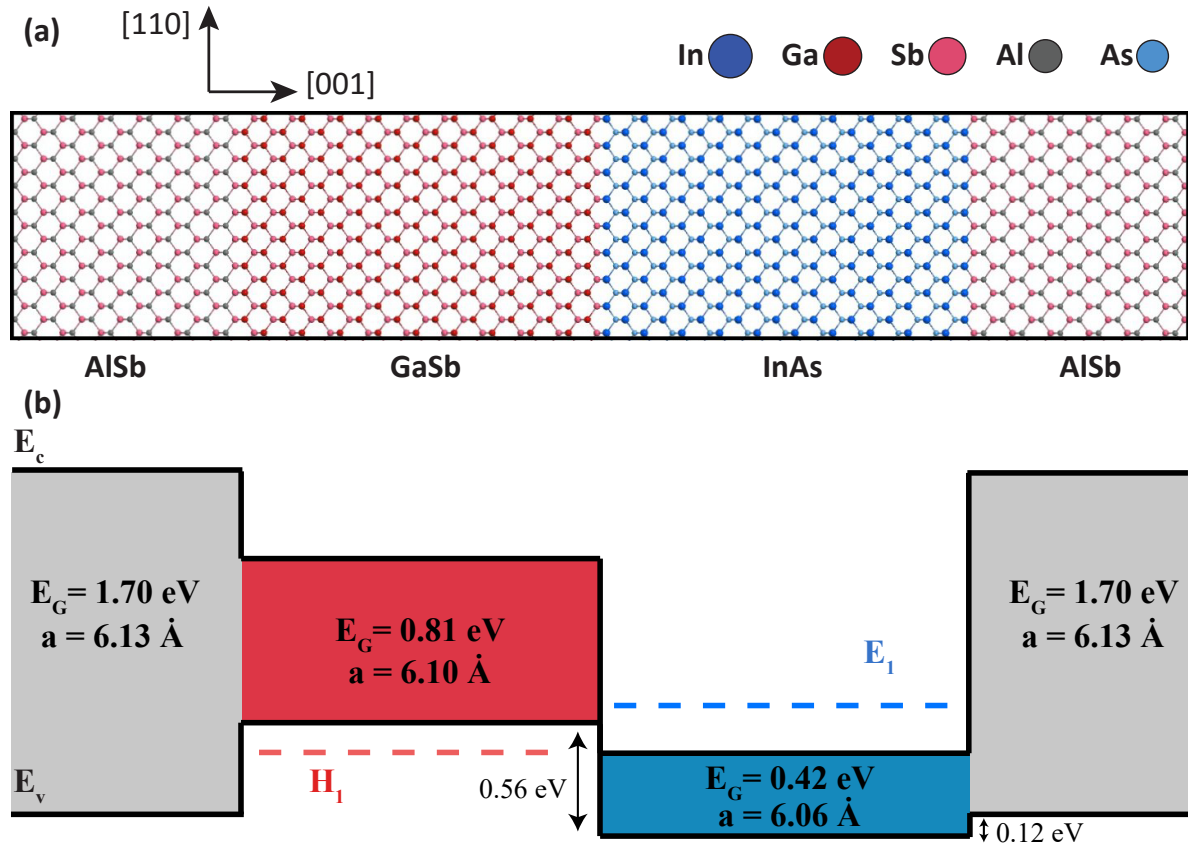


Figure 3.1: (a) Ball and stick model of an AlSb/InAs/GaSb/AlSb heterostructures (b) Band alignments, band gaps, and lattice parameters of the 6.1 Å family.

A hybridization gap was predicted (for superlattices[31] and coupled quantum wells[32,

33, 34]) and experimentally confirmed for InAs/GaSb coupled quantum wells[35]. More recently, a quantum spin Hall (2D TI) phase was predicted for InAs/GaSb heterostructures by Liu and co-workers[18]. This work was based on general symmetry considerations and a band perturbation theory for semiconductors accounting for spin orbit coupling. It was shown that the electronic states near the Γ point observe a quantum phase transition wherein the mass term changes sign and leads to two topologically distinct phases. The work is summarized in Fig. 3.2.

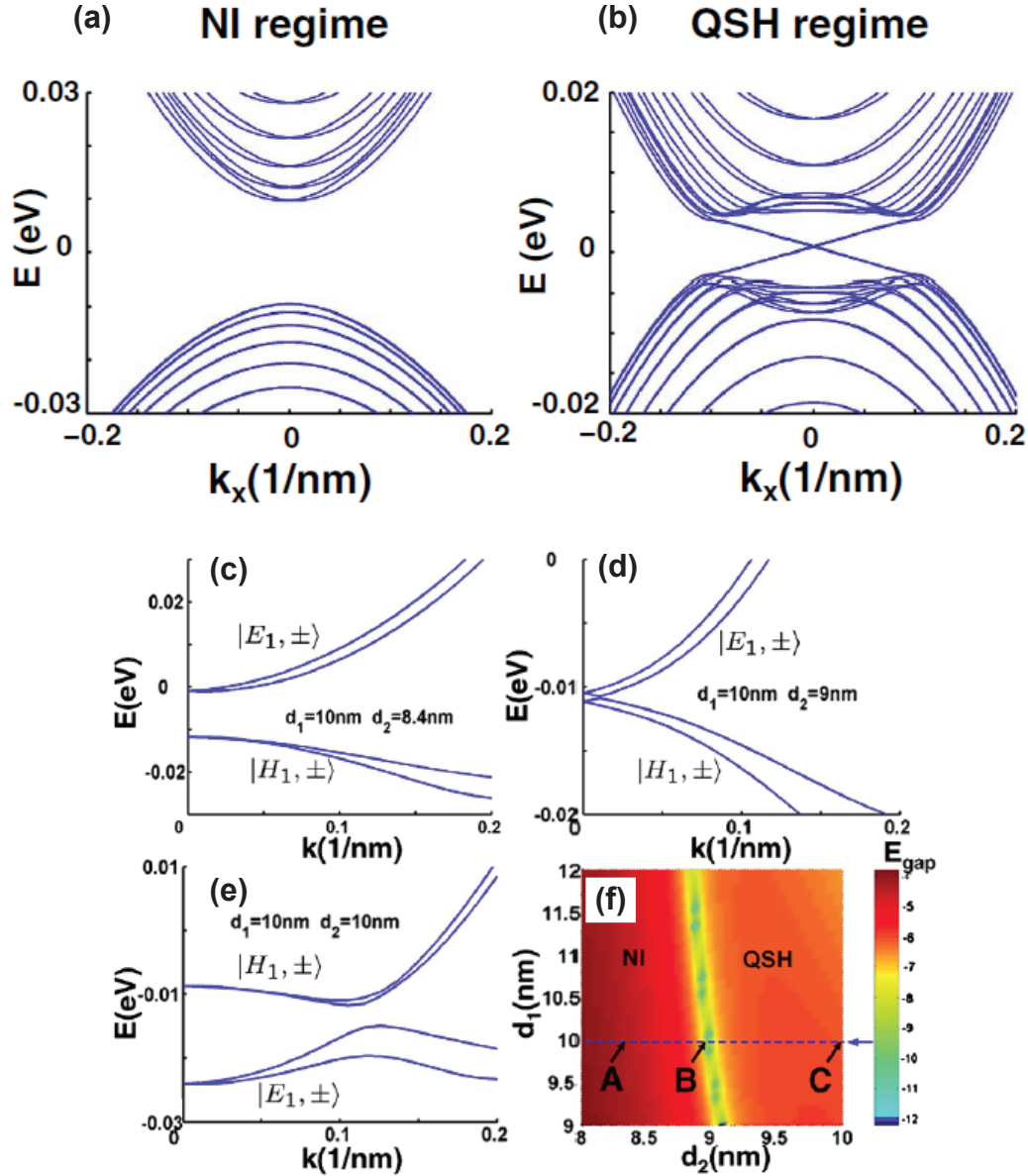


Figure 3.2: The quantum spin Hall (2D TI) phase in InAs/GaSb heterostructures. Adapted from [18] with permission from the American Physical Society <https://www.aps.org/>. (a) Dispersion of an InAs/GaSb coupled quantum well with GaSb layer thickness $d_1 = 10$ nm and InAs layer thickness $d_2 = 8.1$ nm. (b) Dispersion of an InAs/GaSb coupled quantum well with $d_1 = d_2 = 10$ nm. (c) - (e) The energy dispersions calculated from an 8-band Kane hamiltonian for three coupled quantum well configurations. (f) The energy gap variation in the (d_1, d_2) plane. Points A, B and C correspond to the calculations in (c), (d) and (e).

The formation of the quantum spin Hall phase may be understood using the following argument. In the inverted gap subband structure, the relativistic mass must be negative; the electron subband lies below the hole subband and the change in energy to move an electron from the hole subband to the electron subband is opposite that of a normal gap. At the boundary of a material with an inverted gap and a material with a normal gap the mass must change sign[46]. This forces a zero-mass constraint at the boundary. Note that vacuum also requires a positive mass from the energy required to produce electron positron pairs. The zero-mass constraint results in linearly dispersing edge states in the dispersion. Spin-polarization of these states is required by Kramer's theorem[47], where time-reversal invariance at high symmetry points requires a degeneracy at these points[46].

3.2 Spin-Orbit Coupling in Two Dimensional Electron Systems

In non-centrosymmetric zinc-blende semiconductors, such as InAs, the lack of an inversion center of symmetry results in a built-in electric field which from the reference frame of a mobile carrier appears as a magnetic field. The bulk inversion asymmetry produces a splitting in both conduction and valence band states mediated by spin-orbit interaction and is referred to as the Dresselhaus effect[48]. Heterostructures of such materials have additional symmetry breaking internal electric fields and can accommodate the application of an external electric field. The structure inversion asymmetry in heterostructures induces an additional energy splitting of spin-degenerate subbands and is referred to as the Rashba effect[49]. The spin-splitting energy due to the Rashba effect in narrow gap semiconductor heterostructures is comparable to or exceeds the spin-splitting

energy that results from the Dresselhaus effect[50]. The magnetic field generated by the Rashba effect is proportional to the expectation value of the electric field within the confinement potential, and the Dresselhaus field is inversely proportional to the thickness of the confined material[51]. The Rashba effect allows the use of an insulated electrostatic gate to modify the electric field over the heterostructure, and in turn, control the spin-splitting energy of the electronic energy bands.

3.3 Two-Dimensional Carriers in Magnetic Fields

Two-dimensional carriers in quantizing magnetic fields observe a quantization in their allowed energy states parameterized by a quantum number n , the so-called Landau-level. Quantum states with different k but the same n are degenerate. The energy of a given Landau-level increases linearly with the magnetic field. At a fixed electron density, the chemical potential of the electron gas oscillates with the number of occupied Landau-levels, termed the filling factors, which oscillate in a $1/B$ periodic manner. The corresponding oscillation in the density of states results in oscillations of measurements of the magnetoresistivity.

A calculation of the magnetoresistivity taking account Landau-level broadening, Zeeman splitting and spin orbit coupling in an InAs quantum well for three different values of the Rashba spin-orbit coupling constant is shown in Fig. 3.3.

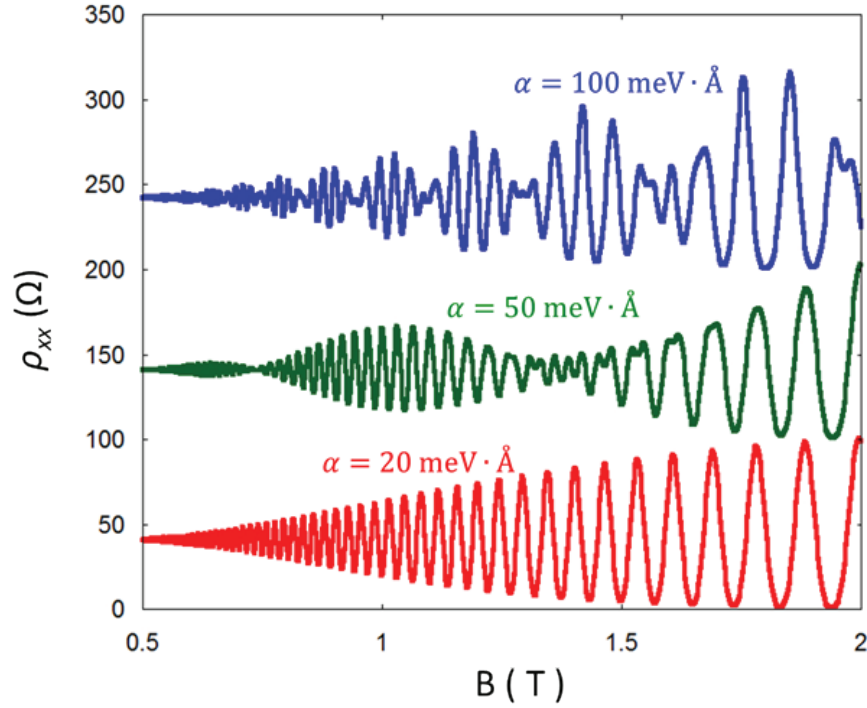


Figure 3.3: The calculated magnetoresistivity as a function of magnetic field for three values of the Rashba spin-orbit coupling constant.

Measurements of the magnetoresistivity allow quantification of the two-dimensional carrier density, the Landau-level broadening, the Zeeman splitting, the spin-orbit coupling and the carrier effective mass. Details are presented in an appendix.

Chapter 4

Scattering Mechanisms and the Limits to Mobility in InAs Quantum Wells with Nearly Lattice Matched Barriers

This chapter contains two parts, the first of which presents a study of scattering mechanisms in gate tunable two dimensional electron gases (2DEGs) confined to InAs/(Al,Ga)Sb heterostructures with varying interface roughness and dislocation density. By integrating an insulated gate structure the evolution of the low temperature electron mobility and single-particle lifetime was determined for a previously unexplored density regime, $10^{11} - 10^{12} \text{ cm}^{-2}$, in this system. Existing theoretical models were used to analyze the density dependence of the electron mobility and single particle lifetime in InAs quantum wells. Scattering was found to be dominated by charged dislocations and interface roughness. It was demonstrated that growth of InAs quantum wells on nearly lattice matched GaSb substrate results in fewer dislocations, lower interface roughness and im-

proved low temperature transport properties compared to growth on lattice mismatched GaAs substrates.

The investigation linking low mobility to high dislocation density was self-contained, but open questions remained regarding the mobility limiting scattering mechanisms in the highest mobility structures. They were addressed by a study of the growth and the density dependence of the low temperature mobility of a series of two-dimensional electron systems confined to un-intentionally doped, low extended defect density InAs quantum wells with $\text{Al}_x\text{Ga}_{1-x}\text{Sb}$ barriers. The electron density was varied using electrostatic gates, and in 15 nm wide InAs quantum wells a non-monotonic dependence of mobility on electron density was observed over the range $2 \times 10^{11} \text{ cm}^{-2}$ to $1.8 \times 10^{12} \text{ cm}^{-2}$. A gate-tuned electron mobility exceeding $750,000 \text{ cm}^2/\text{V}\cdot\text{s}$ was achieved at a sample temperature of 2 K. Analysis of the possible scattering mechanisms suggest at high carrier densities within the first occupied electronic sub-band, the mobility was limited primarily by rough interfaces for narrow quantum wells, and a combination of alloy disorder and interface roughness for 15 nm wide wells. At low carrier density, the functional dependence of the mobility on carrier density provided evidence of coulombic scattering from charged defects.

4.1 The effect of dislocations on the transport properties of InAs quantum wells

4.1.1 Introduction

Heterostructures combining InAs with AlSb, GaSb and their ternary alloys have been of great importance for both mesoscopic physics and optoelectronic device research[36]. The large conduction band offset between InAs and AlSb makes possible deep quantum

wells with high tunneling barriers suitable for devices demanding both high speed and low power consumption. Exchanging Ga for Al allows the band lineup to be tuned from a staggered to broken alignment giving flexibility in band engineering heterostructures for use in optoelectronic applications. The electronic properties motivating device research are also important for condensed matter physics experiments. Theoretical and experimental investigations suggest low dimensional heterostructures of InAs and the antimonides, such as hybrid InAs superconductor structures and InAs/GaSb electron-hole bilayers, host topologically protected states of matter[52, 8, 53, 54, 55, 56]. In these and similar experiments utilizing the formation of a topological phase is dependent on a large momentum relaxation time in the InAs channel[53]. Experimental advances rely on InAs heterostructures with low levels of disorder and high carrier mobility[53, 57]. Understanding the prominent sources of scattering in InAs heterostructures will elucidate ways for improving material quality.

Investigations of scattering mechanisms in InAs quantum wells have focused on heterostructures with electron concentrations of the order 10^{12} cm⁻² and grown on GaAs (100) substrates. Interface roughness scattering has been found to limit the mobility for narrow wells[30], and the dependence on well width has been explained by a model of interface roughness scattering first developed by Gold[58] and modified to account for the non-parabolic conduction band in InAs[30]. Numerical investigations[59, 60] have analyzed the temperature dependence of mobility in modulation doped InAs and InAsSb quantum wells and have determined scattering is dominated by both remote ionized impurities and interface roughness for modulation doped structures. Investigations have also reported on single particle level broadening. Two distinct relaxation times can be defined to characterize the scattering mechanism in a two dimensional system and are denoted by the transport, τ_{tr} , and single particle, τ_q , lifetimes. The former is related to the dc conductivity and is insensitive to small angle scattering, while the latter is re-

lated to the single particle self-energy and is affected by all scattering events with equal weight[61]. In InAs heterostructures with carrier densities near 10^{12} cm⁻² large ratios between transport and single particle lifetimes have been observed[62], and thus, rule out background impurities as a dominant scattering mechanism[63].

4.1.2 Executive Summary

This work reports on the scattering mechanisms in three heterostructures hosting a two dimensional electron gas (2DEG) confined to an unintentionally doped InAs quantum well with antimonide barriers. By adjusting parameters of the buffer layer growth and using both lattice mismatched and nearly lattice matched substrates samples with varying roughness and dislocation density were grown. Integration of an insulated gate structure enabled modulation of the 2DEGs density, and the dependence of electron mobility and single-particle lifetime on electron density at sample temperatures of 1.8 K were determined. Existing theoretical models were used to quantify contributions from individual scattering mechanisms to the total electron mobility. Scattering from charged dislocations and interface roughness were identified as the dominant scattering mechanisms in all heterostructures. Growth on a nearly lattice matched substrate resulted in improved electron mobility and single particle lifetime compared to heterostructures grown on lattice mismatched substrates.

4.1.3 Results and Discussion

The heterostructures were grown by molecular beam epitaxy (MBE) and are depicted as insets in Fig. 4.1(a). Two structures, denoted samples A and B were grown on semi-insulating GaAs (001) substrates. A third structure, denoted sample C, was grown on a Te-doped GaSb (001) substrate. The two structures grown on GaAs substrates initiated

the growth of the antimonides with AlSb on an AlAs nucleation layer and proceeded with a $1.8 \mu\text{m}$ $\text{Al}_{0.8}\text{Ga}_{0.2}\text{Sb}$ buffer and a 200 nm AlSb bottom barrier. In sample A the nucleation and buffer layers were grown at a substrate temperature of $570 \text{ }^\circ\text{C}$. In sample B, the substrate temperature was $530 \text{ }^\circ\text{C}$ for the growth of the nucleation and buffer layers. In sample C, the buffer and bottom barrier are grown at a substrate temperature of $530 \text{ }^\circ\text{C}$. The buffer is insulating at low temperatures and isolates the channel from the conductive substrate.

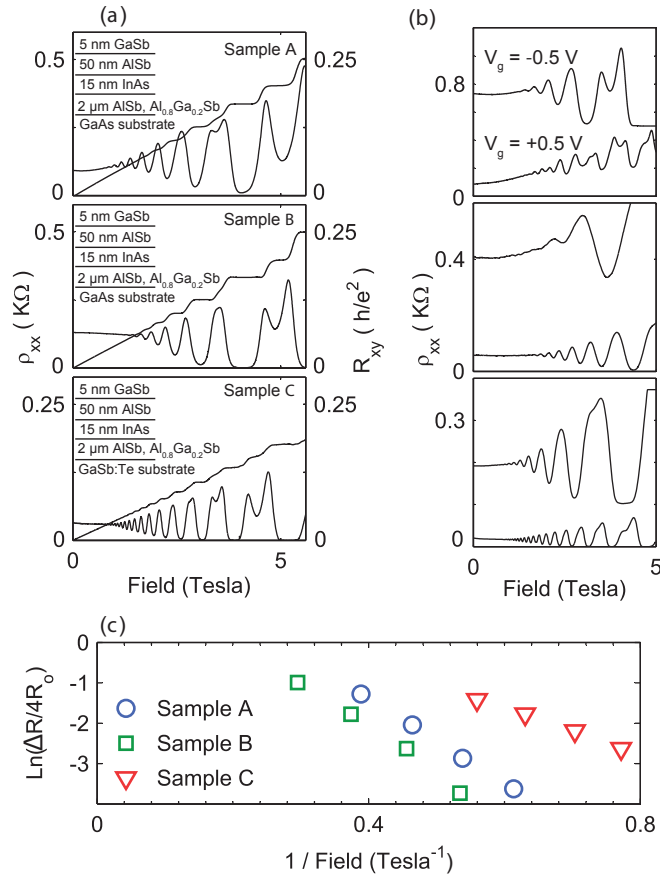


Figure 4.1: (a) Resistivity and Hall resistance as a function of magnetic field at zero gate voltage for samples A, B and C measured in a Hall bar geometry. The structure of each sample is shown as an inset. (b) Magnetoresistance at $V_g = -0.5 \text{ V}$, $+0.5 \text{ V}$ for samples A, B and C. The data is offset for clarity. (c) Dingle analysis of the magnetoresistivity in (a).

For all heterostructures the substrate temperature was reduced to $480 \text{ }^\circ\text{C}$ for the

growth of the InAs quantum well and barriers. Using a shutter sequence first proposed by Tuttle et al. interfaces between the InAs channel and barriers were forced InSb-like[29]. The separation between the InAs channel and the GaSb capping layer was made sufficiently large to reduce the contribution of carriers from the donor-like surface states on the GaSb capping layers[27, 64]. The staggered gap band alignment of InAs and AlSb creates a confinement potential for a single electron gas occupying the lowest energy subband over the gate bias range used in this study.

Gated hall bars were made using standard microfabrication techniques. Following mesa definition with wet chemical etching 40 nm of Al_2O_3 was deposited by atomic layer deposition to serve as the gate dielectric. To avoid parallel conduction through the substrate in the case of sample C openings for the ohmic contacts were formed by first etching vias through the dielectric, then the top antimonide barrier and stopping at the InAs channel. Ti/Au was deposited by electron beam evaporation for both ohmic contact and gate metallization.

Longitudinal resistance was measured in the [1-10] direction for all samples. Measurements were carried out in a He-4 cryostat using standard lock-in techniques. Resistivity and Hall resistance as a function of magnetic field at zero gate voltage are plotted in Fig. 4.1(a). Each sample shows well developed integer quantum Hall states ($\rho_{xx} = 0, R_{xy} = h/e^2\nu$).

The magnetoresistance at two gate voltages is depicted for each sample in Fig. 4.1(b). Under negative gate bias full quantization of the integer quantum Hall states were maintained in all samples. The 2DEG carrier density determined from the periodicity in the SdH oscillations at low magnetic field was in good agreement with the density determined from the slope of the Hall resistance at low magnetic field. The carrier density dependence on the gate voltage was linear for all gated hall bar devices. The single particle lifetime was determined from a Dingle analysis of the SdH oscillations[65]. The amplitude

of the oscillations, ΔR , is given by $\Delta R = 4R_o X(T) \exp(-\pi/\omega_c \tau_q)$, where R_o is the zero-field longitudinal magnetoresistance, and $X(T) = (2\pi^2 k_B T / \hbar \omega_c) / \sinh(2\pi^2 k_B T / \hbar \omega_c)$ is a function of temperature, T , and $\omega_c = eB/m^*$, where B is the magnetic field, e is the elementary charge, k_B is the Boltzmann constant, and T is the sample temperature. The zero-field effective mass, m^* , at zero gate bias was determined to be $(0.033 \pm 0.001)m_o$ from analysis of SdH oscillation amplitudes as a function of temperature. The measurement of the effective mass is in agreement with an estimate using $\mathbf{k} \cdot \mathbf{p}$ formalism accounting for band non-parabolicity[66]. Calculated values were used to account for the effective mass dependence on density. The logarithm $\ln(\Delta R/4R_o X(T))$ generated from the data in Fig. 4.1(a) is plotted against $1/B$ in Fig. 4.1(c). This analysis is repeated at different gate voltages to establish the density dependence of the quantum lifetime in each sample.

The morphology of the MBE grown films were measured by atomic force microscopy (AFM). AFM scans are shown in Fig. 4.2(a), 4.2(b) and 4.2(c) for samples A, B and C, respectively. A line profile for each sample is shown in Fig. 4.2(d) to aid in comparing the height variation across the samples. In all samples steps with heights corresponding to a bilayer variation (3 \AA) were observed.

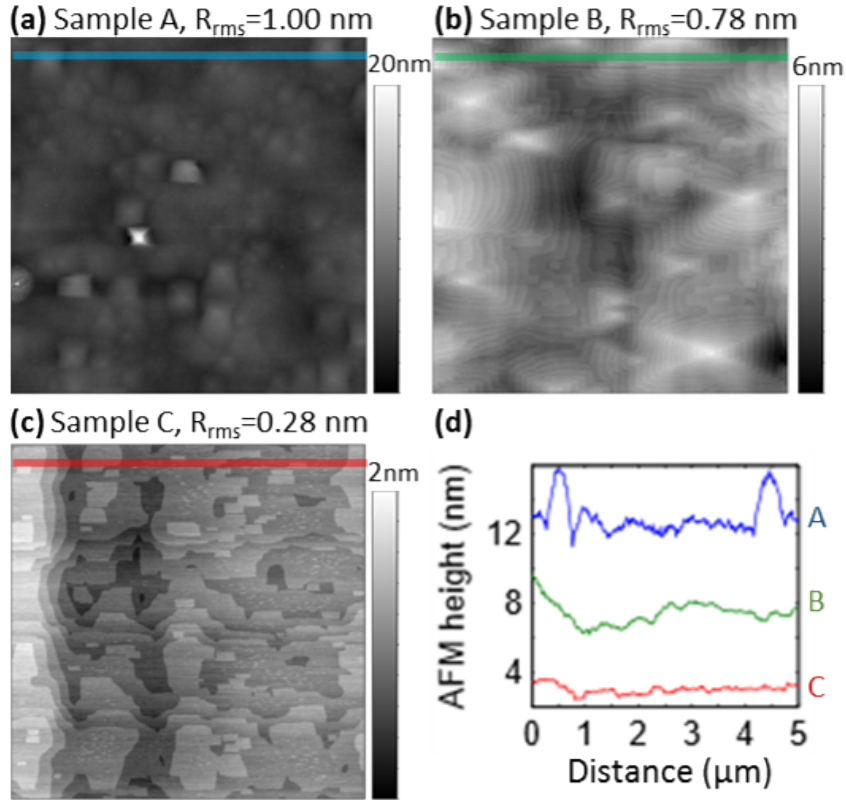


Figure 4.2: (a) $5 \times 5 \mu\text{m}^2$ AFM measurement of sample A (b) $5 \times 5 \mu\text{m}^2$ AFM measurement of sample B (c) $5 \times 5 \mu\text{m}^2$ AFM measurement of sample C (d) AFM line profiles from (a), (b) and (c) along the [1-10] crystallographic direction.

In samples A and B mounds due to spiral growth around threading dislocations with screw character were observed. The step density per mound and the average mound height is higher in sample A than in sample B, and the lateral mound dimensions in sample A are smaller than in sample B. The RMS roughness measured in samples A and B are 1.00 nm and 0.78 nm, respectively, and are substantially larger than the 0.28 nm RMS roughness measured on sample C. The density of mounds resulting from spiral growth was used as an estimation of the dislocation density[39] in samples A and B, and was determined to be approximately 10^8 cm^{-2} . From an etch pit density measurement on sample C the dislocation density was determined to be approximately 10^7 cm^{-2} .

Existing numerical models wherein the relaxation time approximation is applied to the

Boltzmann equation were used to examine contributions of individual elastic scattering mechanisms to the total electron mobility. An analysis outlined by Gold[58] was used to calculate scattering rates due to homogeneous background impurities at a concentration N_{BI} . The contribution from interface roughness scattering was incorporated by modeling the interface morphology as a Gaussian distribution with a mean step height, Δ , and a lateral correlation length, Λ , of the quantum well width fluctuations[30, 58]. Charged dislocations were modeled as line charges[67] with an areal density N_{disl} . The inverse mobility can be expressed by Mathiessens rule, $1/\mu_{total} = 1/\mu_{BI} + 1/\mu_{disl} + 1/\mu_{IR}$. The scattering mechanisms collectively determine the functional dependence of the mobility on the density.

Fig. 4.3(a) shows the mobility calculated from individual elastic scattering mechanisms for several N_{BI} , (Δ, Λ) , and N_{disl} . The experimentally measured values of the mobility and density in samples A, B and C overlay the calculations. In the MBE system used for this study N_{BI} is estimated to be of the order 10^{16} cm^{-3} for InAs and has a relatively small contribution to the overall scattering rate.

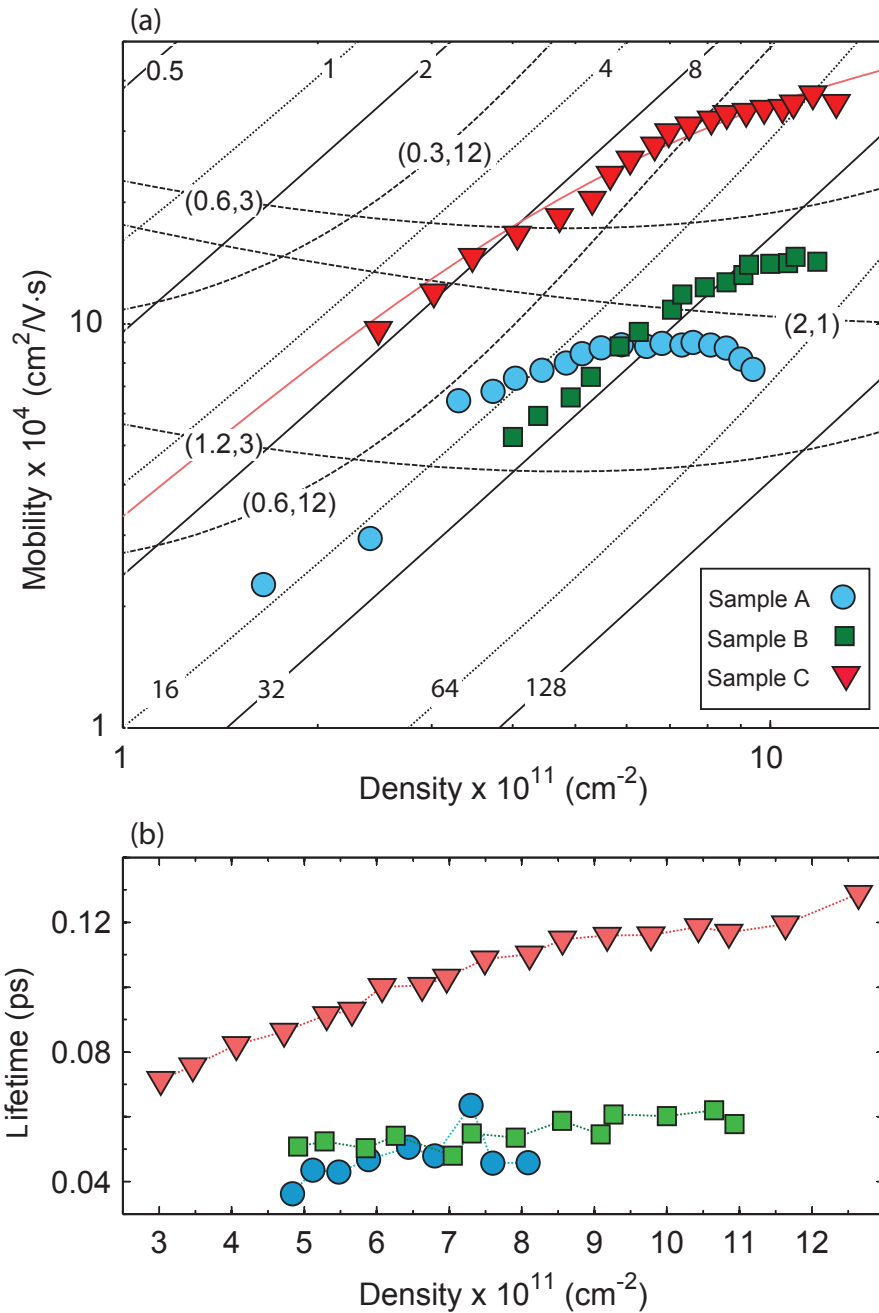


Figure 4.3: (a) Mobility as a function of density calculated for background impurity (dotted lines), dislocation (solid lines) and interface roughness scattering (dashed lines). Measurements of mobility as a function of density are shown as data points. Calculations are made for several $N_{BI} \times 10^{16} \text{ cm}^{-3}$, $N_{disl} \times 10^7 \text{ cm}^{-2}$ and $(\Delta \text{ nm}, \Lambda \text{ nm})$. The values of the parameters label the respective lines. The red solid line is the calculated total mobility for a $N_{BI} = 1 \times 10^{16} \text{ cm}^{-3}$, $N_{disl} = 4.3 \times 10^7 \text{ cm}^{-2}$, $\Delta = 0.46 \text{ nm}$, and $\Lambda = 1.8 \text{ nm}$. (b) Measured single particle lifetime as a function of density.

In all samples the evolution of mobility with density can be divided into two regimes in which the functional dependence of the mobility on the density are distinct. At low carrier density the mobility follows a power law dependence between 1 and 1.5, a trend consistent with scattering dominated by charged dislocations[67]. The dislocation densities determined from modeling the experimental data agrees with estimates of dislocation densities determined from AFM and etch pit density measurements. At higher carrier densities (above $4 \times 10^{11} \text{ cm}^{-2}$ for sample A and $6 \times 10^{11} \text{ cm}^{-2}$ for samples B and C) the dependence of the mobility on the density observes a transition to scattering dominated by interfacial roughness.

The transition from scattering dominated by dislocations to scattering dominated by interface roughness is most striking in sample A. The decrease in mobility at higher carrier density before the occupation of a second subband is consistent with scattering by rough interfaces. A similar decrease in mobility with increasing density has been reported in 2DEGs confined to high interface roughness GaN/AlGaIn heterostructures[68]. The relatively weaker dependence of mobility on scattering from interface roughness in samples B and C is attributed to larger lateral dimensions of bilayer steps as well as smaller and more uniform mound heights if one assumes the morphology measured on the surface of the film correlates with the morphology of the quantum well interfaces.

The dependence of mobility on density in sample C was found to be in close agreement with the calculated curve, shown as a red solid line in Fig. 4.3(a), using parameters $N_{BI} = 1 \times 10^{16} \text{ cm}^{-3}$, $N_{disl} = 4.3 \times 10^7 \text{ cm}^{-2}$, $\Delta = 0.46 \text{ nm}$, and $\Lambda = 1.8 \text{ nm}$. The parameters used to model the mobility from interface roughness scattering are different than those determined in previous studies[30]; however, in those findings, the measured mobility in wider quantum wells showed greater deviation from the model than narrower quantum wells. The current work includes contributions from multiple dominant scattering mechanisms making it more suitable for wider quantum wells and over a large density regime.

It is noted that a modification to the theory describing interface roughness scattering to account for the asymmetric distribution of the wave function at large gate voltages may result in small changes in parameters describing the interface roughness.

In Fig. 4.3(b) the evolution of τ_q as a function of density is shown. The weak dependence of τ_q on the carrier density in samples A and B are similar to those found in previous studies in quantum wells with higher densities and modulated by illumination or application of hydrostatic pressure[62]. The weak dependence of τ_q on density can result from the high dislocation density and the corresponding high small angle scattering rate[63, 61]. In contrast, in sample C where the dislocation density is lower τ_q shows a strong dependence on density and is larger in magnitude.

In sample C, the mobility and single particle lifetime, τ_q , are substantially greater than that measured in samples A and B over the studied density range. It is emphasized that the improved transport properties were due to a reduction in dislocation density and associated interfacial roughness from spiral growth around threading dislocations. Higher crystal quality was achieved by growth on a lattice matched substrate, but it is noted that similar quality may be reproduced for growth on lattice mismatched substrates if appropriate buffer structures and nucleation techniques[69] are implemented. The dislocations in sample C arise from the mismatch between the 2 μm $\text{Al}_{0.8}\text{Ga}_{0.2}\text{Sb}$ buffer layer and the GaSb substrate. A similar unintentionally doped InAs quantum well was grown using an $\text{AlAs}_{0.09}\text{Sb}_{0.91}$ buffer layer with a closer lattice match to the GaSb substrate. The structure was found to have fewer than 10^6 cm^{-2} dislocations, and the mobility measured over $700,000 \text{ cm}^2/\text{V}\cdot\text{s}$ at an electron density gated tuned to $1 \times 10^{12} \text{ cm}^{-2}$ and a sample temperature of 1.8 Kelvin.

The results of the numerical calculations have not included contributions from remote ionized impurity, inter-subband or alloy scattering. The structures were not modulation doped, and the power law dependence of mobility on density and the ratio of the transport

lifetime to the quantum lifetime are not consistent with remote ionized impurity scattering being the dominant scattering mechanism in the samples[70]. The SdH oscillations were periodic in inverse magnetic field with a single frequency at all gate voltages, and showed no evidence of intra-subband or inter-subband scattering[71]. The alloy scattering rate that may arise from unintentional alloying due to group V and group III intermixing during MBE growth is negligible compared to dislocation and interface roughness scattering rates over the studied carrier density range. Altogether, it was consistently observed that the 2DEG mobility in InAs/AlSb quantum wells was limited by scattering from charged dislocations and rough interfaces.

4.1.4 Conclusion

This work identifies extended defects and interface roughness as dominant scattering mechanisms in InAs/(Al,Ga)Sb heterostructures over the density regime $10^{11} - 10^{12}$ cm^{-2} . It was demonstrated that growth of InAs quantum wells on nearly lattice matched GaSb substrate results in fewer dislocations, lower interface roughness and improved low temperature transport properties compared to growth on lattice mismatched GaAs substrates. The evolution of the low temperature electron mobility was analyzed using existing theoretical models and scattering was found to be dominated by charged dislocations and interface roughness. A decrease in dislocation density and interface roughness was also correlated with an increase in magnitude and a stronger carrier density dependence of the single particle lifetime.

4.2 On the Limits to Mobility in InAs Quantum Wells with Nearly Lattice Matched Barriers

4.2.1 Introduction

A significant achievement of material science is the perpetual enhancement of low temperature two-dimensional (2D) electron and hole mobility in semiconductor heterostructures. Modulation doping, a technique that allows the spatial separation between dopants and carriers[72], and repeated advances in molecular beam epitaxy (MBE) have led to carrier mobility greater than 10^7 cm²/V·s and greater than 10^6 cm²/V·s in electron[73, 74] and hole[75] doped GaAs based 2D systems, respectively. These achievements are limited to GaAs based heterostructures; similar advances have yet to be made in other compound semiconductor heterostructures.

Of particular interest are heterostructures wherein carriers are confined to narrow gap semiconductors such as InAs and InSb. Strong spin-orbit coupling in narrow gap semiconductors and their heterostructures make them suitable for developing novel spin based electronics[76, 77, 78] and for realizing topological superconductivity in semiconductor-superconductor heterostructures[79, 80, 8, 52]. For their utilization in quantum information processing low-dimensional systems require sufficiently high carrier mobility[53]. In state-of-the-art GaAs based 2D electron systems, it is believed mobility is limited by homogeneous background impurities[70]. If similar scattering rates could be achieved in the narrow gap semiconductors, then a scaling by the effective mass would yield higher mobility than the best GaAs 2D electron systems, by a factor of approximately 3 for carriers confined to InAs and approximately 4 for carriers confined to InSb. Reported values of mobility[36, 81] are a factor of 100 lower than what may be theoretically possible for the narrow gap semiconductors. Advances require a greater understanding of the

scattering mechanisms in heterostructures of the narrow gap semiconductors.

4.2.2 Executive Summary

This work reports on scattering mechanisms and the limits to mobility in InAs quantum wells investigated by a comparative study of heterostructures with varying well thicknesses and interface growth procedures in which the density dependence of the low temperature mobility was determined by magnetotransport experiments using a dual gated Hall bar device geometry. In 15 nm wide InAs quantum wells a non-monotonic dependence of mobility on electron density was observed over the range $2 \times 10^{11} \text{ cm}^{-2}$ to $1.8 \times 10^{12} \text{ cm}^{-2}$. A gate-tuned electron mobility exceeding $750,000 \text{ cm}^2/\text{V}\cdot\text{s}$ was achieved at a sample temperature of 2 K. The possible scattering mechanisms leading to the observed density dependence of the mobility are discussed.

4.2.3 Results and Discussion

Heterostructures were grown by molecular beam epitaxy (MBE) on GaSb:Te (001) substrates. Growth rate and composition calibrations were performed prior to the growth of the heterostructures and verified by reflection high energy electron diffraction patterns and oscillations during the growth of the heterostructures. Fig. 4.4(a) depicts a schematic MBE grown structure with integrated gate dielectric and front gate metallization. The conduction band in the vicinity of a 15 nm wide InAs quantum well is depicted in Fig. 4.4(b) for the case of $\text{Al}_{0.8}\text{Ga}_{0.2}\text{Sb}$ barriers. The self-consistent calculation depicts a case wherein the Fermi energy lies between the first and second electronic sub-band of the two dimensional system. For the structures used in this study, the Fermi energy could be gate tuned using the dual gated Hall bar geometry shown in Fig. 4.4(c), where the tellurium doped GaSb substrate serves as one electrostatic gate and the Ti/Au metallization over

the Al_2O_3 dielectric serves as a second electrostatic gate.

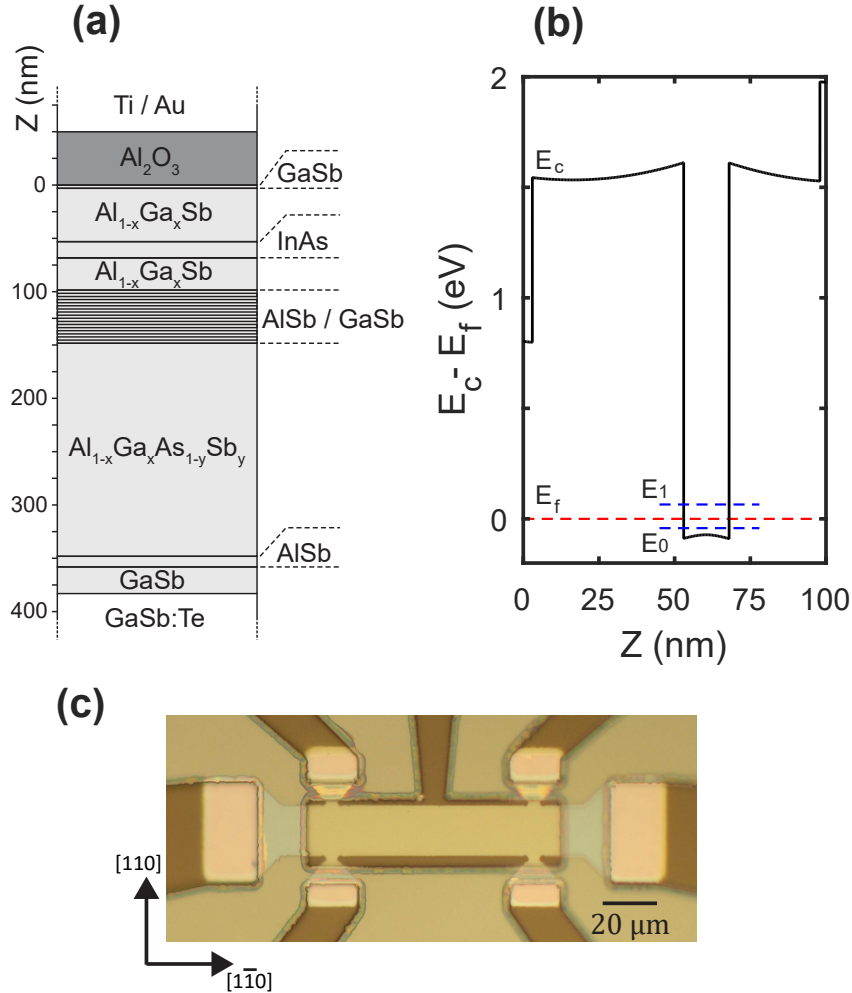


Figure 4.4: (a) A schematic of the InAs quantum well heterostructure with Al_2O_3 gate dielectric and Ti/Au front gate. (b) A self-consistent calculation of the conduction band profile and the first and second electronic subband levels relative to the Fermi level for an $\text{Al}_{0.8}\text{Ga}_{0.2}\text{Sb}/\text{InAs}/\text{Al}_{0.8}\text{Ga}_{0.2}\text{Sb}$ quantum well. (c) An optical micrograph of one of the Hall bar devices used in this study prior to gate and ohmic metallization.

Five structures, denoted samples A through E, were grown using similar electrically isolating $\text{Al}_{1-x}\text{Ga}_x\text{As}_{1-y}\text{Sb}_y/\text{AlSb}$ buffer layers through the AlSb/GaSb superlattice using a cumulative group V:III beam equivalent pressure (BEP) ratio of 4:1 and a substrate temperature of 510 $^\circ\text{C}$. The substrate temperature was reduced to 470 $^\circ\text{C}$ for the growth

of the superlattice and the remaining layers. The barriers and InAs layer were grown using a BEP ratio of 3:1 and 4:1, respectively. The set of structures comprised variations in the InAs layer thickness, the shutter sequence used to transition the growth between the barriers and quantum well, and the composition of the $\text{Al}_{1-x}\text{Ga}_x\text{Sb}$ barriers. Growth of samples A, B and C made use of a shutter sequence, denoted Procedure I, developed by Tuttle and co-workers[29]. Growth of samples D and E implemented a shutter sequence, denoted Procedure II, wherein group V and III shutters were closed and opened simultaneously when the growth transitioned between barriers and the InAs layer. Table 4.1 summarizes several critical characteristics of samples A through E. Additional details of the growth and device fabrication can be found in reference [20].

Sample	InAs thickness (nm)	Barrier composition	Interface formation	$\dagger N_{Hall}$ (10^{11} cm^{-2})	$\dagger N_{SdH}$ (10^{11} cm^{-2})	$\dagger \mu$ ($\text{cm}^2/\text{V}\cdot\text{s}$)
A	15	AlSb	Procedure I	3.81	3.82	258,000
B	10	AlSb	Procedure I	4.64	4.53	117,000
C	8	AlSb	Procedure I	3.59	3.44	20,000
D	15	AlSb	Procedure II	4.47	4.64	332,000
E	15	$\text{Al}_{0.8}\text{Ga}_{0.2}\text{Sb}$	Procedure II	4.43	4.69	355,000

\dagger Measured at a sample temperature of 2 Kelvin and $V_f = V_b = 0 \text{ V}$

Table 4.1: Characteristics of the InAs quantum wells discussed in the text.

The surfaces of the MBE-grown films appeared flat when examined under a Nomarski microscope at 100x magnification. Atomic force microscopy (AFM) of the surfaces revealed height variations corresponding to GaSb monolayer-height steps (0.3 nm) on all samples. Exemplar $20 \times 20 \mu\text{m}^2$ and $5 \times 5 \mu\text{m}^2$ AFM scans of sample E are shown in Fig. 4.5(a) and 4.5(b), respectively. Height variations along the [1-10] crystallographic direction starting at the triangular marker in Fig. 4.5(b) are depicted in Fig. 4.5(c).

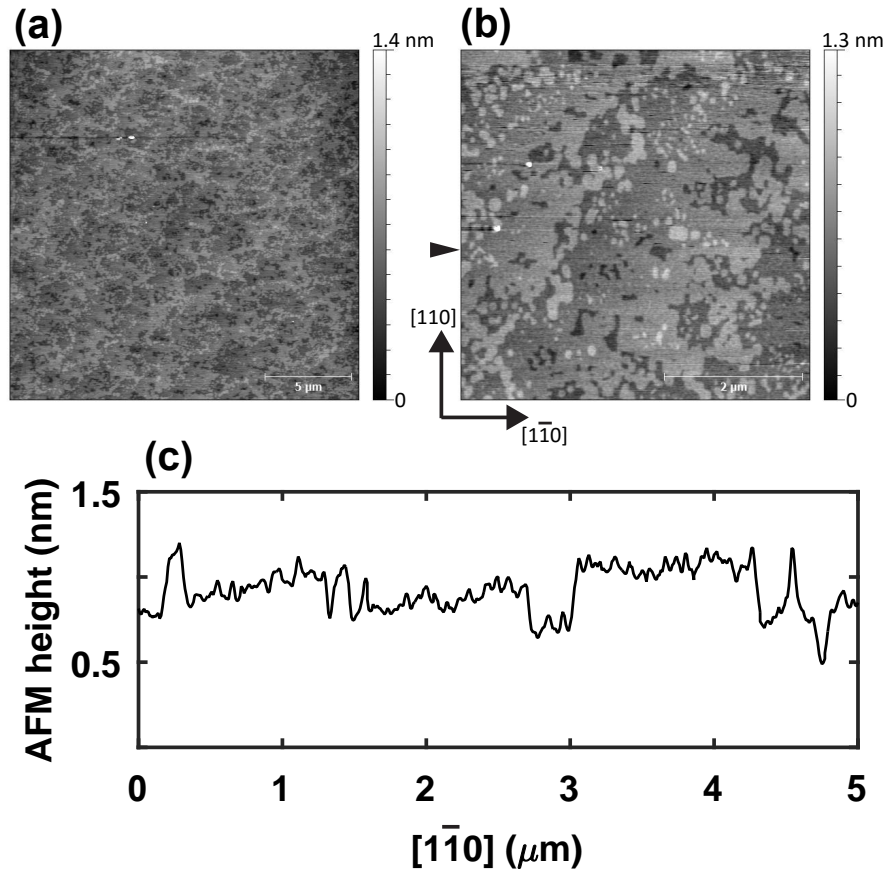


Figure 4.5: (a) A $20 \times 20 \mu\text{m}^2$ atomic force microscope image of sample E taken at the surface of the GaSb capping layer. (b) A $5 \times 5 \mu\text{m}^2$ subset of the image in (a). (c) A line scan along the $[1-10]$ crystallographic direction with origin at the arrow in (b)

In a previous work it was reported the carrier mobility and single-particle lifetime in InAs/(Al,Ga)Sb heterostructures are sensitive to the dislocation density in the epitaxial layers[19]. In this work the use of the nearly lattice matched substrate and buffer layers was intended to inhibit the formation of extended defects during MBE growth. Fig. 4.6(a) shows the thin film x-ray diffraction reciprocal space map in the vicinity of the 002 and asymmetric 115 Bragg reflections of the GaSb substrate of sample D. In the 115 reciprocal space map, the substrate peak and the peak from the $\text{AlAs}_{1-y}\text{Sb}_y$ buffer layer are well resolved and indicate the buffer was nearly lattice matched but slightly tensile strained

to the substrate ($y \approx 0.9$). The threading dislocation densities of the films were measured by both etch pits using a solution of HF:H₂O₂:H₂SO₄:H₂O similar to that reported by Aifer and Maximenko[82] and by electron channeling contrast imaging (ECCI) using a backscattering geometry in a field emission scanning electron microscope. ECCI analysis was performed using several diffraction vectors to mitigate unintentionally satisfying the invisibility criterion where the Burgers vector for a given dislocation is perpendicular to the diffraction vector.

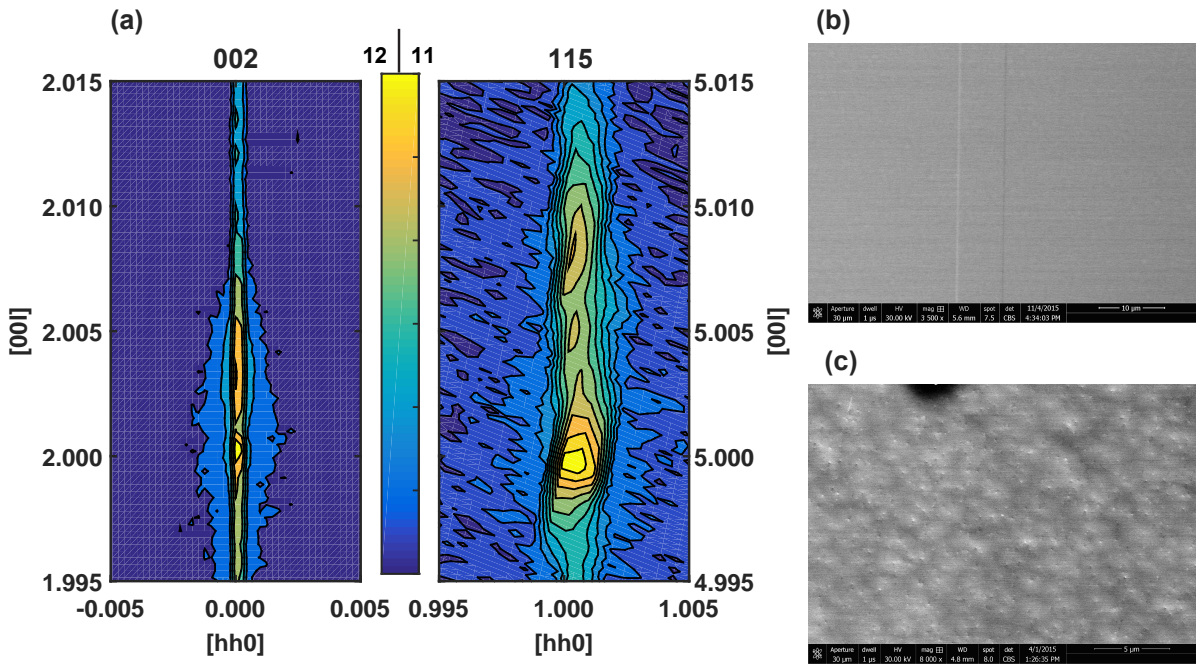


Figure 4.6: (a) X-ray diffraction reciprocal space maps of sample D measured close to the 002 and close to the asymmetric 115 Bragg reflections of the GaSb substrate. The color scale linearly spans the logarithm of the intensity. (b) Electron channeling contrast image (ECCI) of sample D. The scale bar at the lower right reads 10 μm . (c) Electron channeling contrast image of a reference GaSb buffer grown on a lattice mismatched GaAs (001) substrate. The scale bar at the lower right reads 5 μm . M.P. Echlin and P.G. Callahan assisted with ECCI measurements.

Fig. 4.6(b) shows an ECCI micrograph measured from the surface of the MBE grown film of sample D. Several lines of enhanced contrast are interpreted to be due to the presence of

misfit dislocations confined to heterointerfaces within the epitaxial layers. ECCI analysis was also performed on a 1 μm GaSb buffer structure grown on a GaAs (001) lattice mismatched substrate. An ECCI micrograph of the buffer grown on the mismatched substrate, shown in Fig. 4.6(c), indicates a high density of surface penetrating threading dislocations which manifest as bright spots. For the quantum well heterostructures grown using lattice matched buffers both the ECCI analysis and etch pit densities indicate low threading dislocation densities; a conservative estimate of 10^6 dislocations/ cm^2 is used as an upper limit for all samples.

A high angle annular dark field (HAADF) scanning transmission electron microscope (STEM) image of sample D along the [1-10] zone axis and in the vicinity of the InAs quantum well is shown in Fig. 4.7.

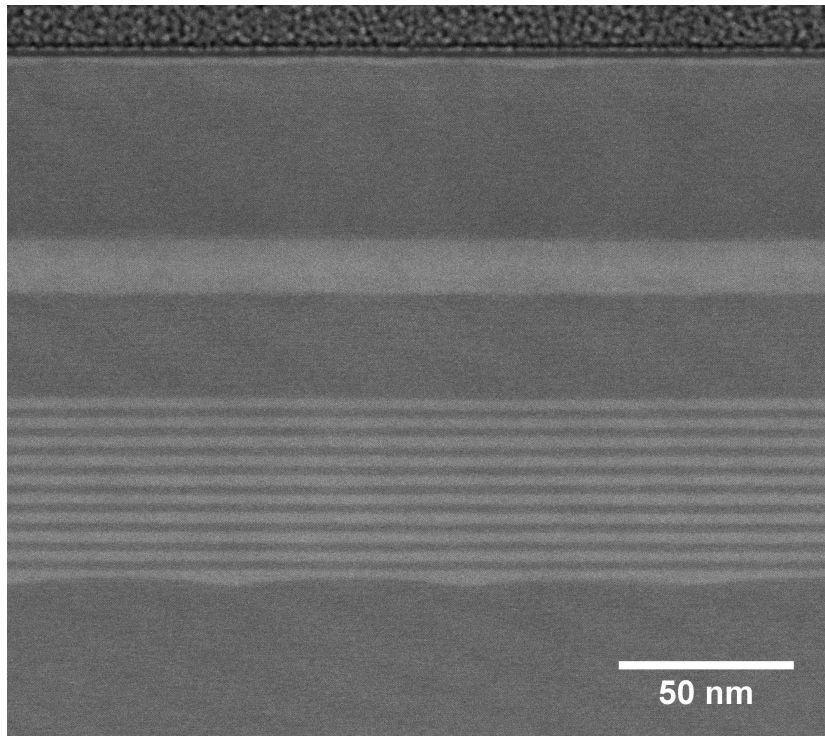


Figure 4.7: High angle annular dark field (HAADF) scanning transmission electron microscope (STEM) image of sample D along the [1-10] zone axis and in the vicinity of the InAs quantum well. The approximately 80 nm thick specimen was prepared by milling a section of wafer using a focused gallium ion beam. D.J. Pennachio prepared the TEM specimen on sample D, and D.J. Pennachio and S. Kraemer assisted with STEM measurements.

The 80 nm thick specimen was prepared by milling a section of wafer using a focused gallium ion beam. The undulations at the interface between the superlattice and the $\text{AlAs}_{1-y}\text{Sb}_y$ buffer are interpreted to be due to strain in the buffer and a resulting change in its surface morphology during growth. The tensile strain on the InAs channel is expected to result in a narrowing of the band gap and a shift in subband energy levels relative to the unstrained case. The well and barrier layer thicknesses measured by HAADF-STEM in sample D are in agreement with the values expected from MBE growth rate calibrations.

Magnetotransport experiments were carried out on dual gated Hall bars at a sample

temperature of 2 K in a He-4 cryostat and using an excitation current of $1 \mu\text{A}$. Measurements of the Hall and longitudinal magnetoresistance, as shown for sample D in Fig. 4.8 at a front and back gate voltage of 0 V, allowed the determination of carrier density and carrier mobility. In all devices, the carrier density varied linearly with applied gate voltages. A gating efficiency of the front gate, $\frac{dn_s}{dV_f} \approx 3.5 - 4.0 (10^{11} \text{ cm}^{-2} \cdot \text{V}^{-1})$ was typical. The determination of carrier density by the slope of the low-field Hall resistance and by the periodicity of Shubnikov de Haas (SdH) oscillations were in good agreement, and are summarized in Table 4.1 at zero gate bias.

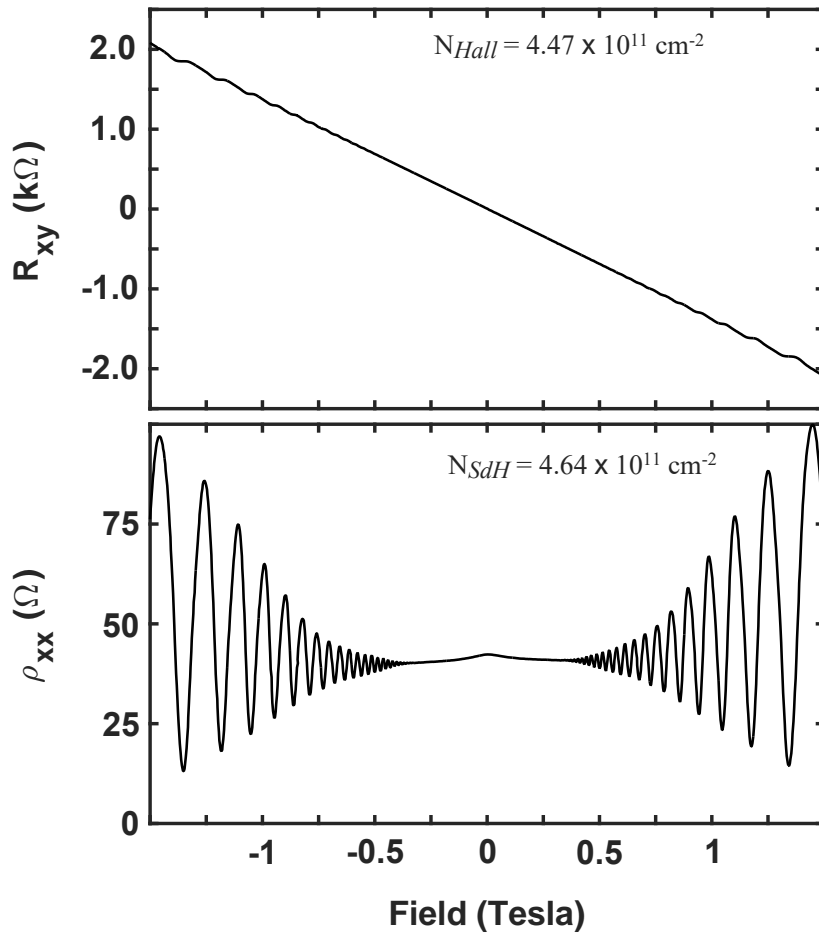


Figure 4.8: The Hall resistance (upper plot) and magnetoresistivity (lower plot) of sample D at $V_f = V_b = 0 \text{ V}$ and at a sample temperature of 2 K.

The carrier density dependence of the mobility was measured by gate-tuning the carrier density. To determine the scattering mechanisms that led to the functional dependence of the mobility on density a series of elastic scattering calculations were performed. These calculations included scattering due to background impurities, remote impurities, charged dislocations, interface roughness and alloy scattering[58, 67, 83, 84]. The calculations are outlined in Appendix A and follow the treatment of the transport relaxation time outlined by Stern and Howard[85] but modified to account for a square well confinement potential, and where zero temperature is assumed, and inter-subband scattering, multiple scattering events, and correlations between ionized impurities are neglected. The calculations were intended to determine the expected functional dependence of the mobility on carrier density and qualitatively determine which scattering mechanisms may be dominant in InAs quantum wells with nearly lattice matched barriers over a given carrier density range. Transport relaxation times were calculated individually and the total mobility was evaluated using Mathiessens rule.

The dependence of the mobility on density for samples A, B, and C is shown in Fig. 4.9(a). In all three cases, the density was tuned using the front gate. The back gate was fixed at 0 V and 0.8 V for sample A, and 0 V for samples B and C. For the 10 nm wide well, sample B, and the 8 nm wide well, sample C, the mobility increased monotonically with density. The dependence of mobility on density in the 15 nm wide well, sample A, and at 0 V bias on the back gate followed a power law dependence on the density, $\mu \propto n^\alpha$, with $\alpha \approx 1.4$, at low density and a saturation of the mobility at high density. The decrease in mobility at all densities for the thinner quantum wells relative to the thicker well was interpreted to be due to an increased dominance of interface roughness scattering, and provides evidence for interface roughness scattering being the dominant scattering mechanism in the thinner wells over the studied carrier density range.

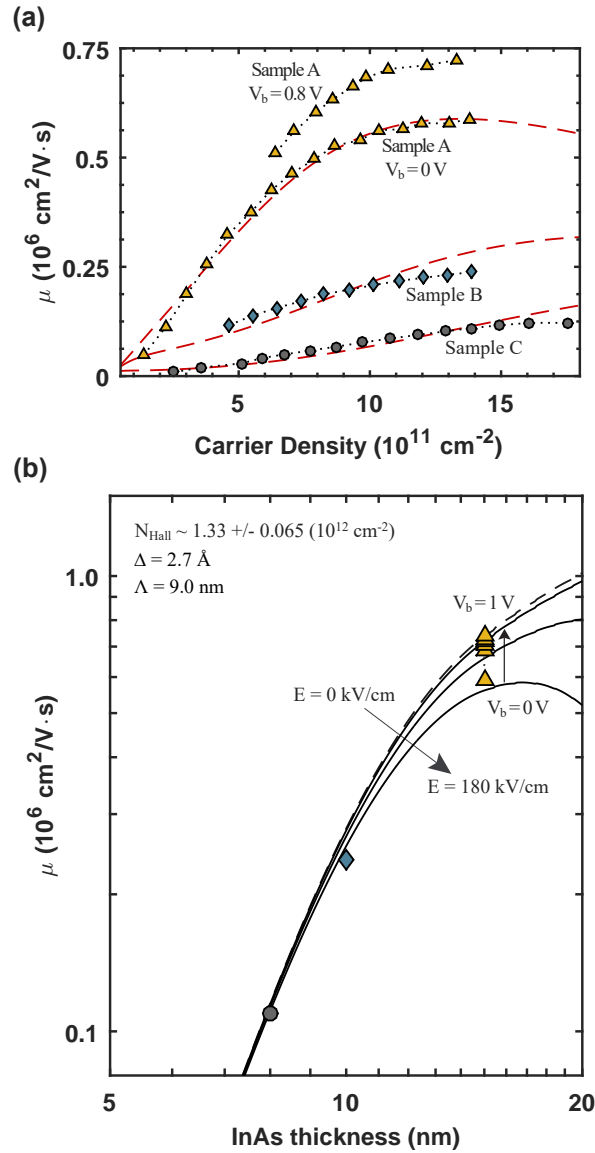


Figure 4.9: (a) The dependence of mobility on carrier density for sample A at constant back gate voltages $V_b = 0 \text{ V}$ and 0.8 V , and for sample B and C at constant back gate voltage $V_b = 0 \text{ V}$. The carrier density was changed by varying the front gate, V_f . The red dashed curves depict the calculated total mobility. (b) The dependence of mobility on the InAs thickness. The calculated mobility for zero average electric field over the quantum well is shown as the dashed line. The mobility for electric fields of 60, 120 and 180 kV/cm are shown as solid lines. The carrier density determined by Hall measurements and the interface roughness parameters used in the calculations are shown in the inset. The remaining parameters were an alloy composition of $\text{InAs}_{0.987}\text{Sb}_{0.013}$, a homogeneous background impurity concentration, $N_{BI} = 1 \times 10^{14} \text{ cm}^{-3}$, remote impurities, $N_{2D,R} = 5 \times 10^{12} \text{ cm}^{-2}$ located at the dielectric/III-V interface, remote impurities, $N_{3D,R} = 1 \times 10^{17} \text{ cm}^{-3}$ distributed through the top and bottom barriers, and a threading dislocation density, $N_{disl} 1 \times 10^6 \text{ cm}^{-2}$.

The value of the maximum mobility at high carrier density was a sensitive function of the back gate voltage, as depicted by the comparison of the density dependence of the mobility for sample A at a fixed back gate voltage of 0 V and 0.8 V. At high density, under accumulation by application of a positive front gate voltage, application of a positive back gate voltage corresponded to a decrease in the electric field and a decrease in the potential asymmetry over the quantum well. The corresponding increase in mobility suggests a dominant scattering mechanism that is a function of the magnitude of the electric field and the position of the electron wave function over the quantum well; therefore, both interface roughness scattering and alloy scattering are suspected of being dominant scattering mechanisms at high electron densities, the latter being due to a non-uniform alloy distribution resulting from asymmetric element intermixing during MBE growth. The mobility was less sensitive to the potential asymmetry over the quantum well at low density, suggesting the contribution to carrier scattering by interface roughness and alloy disorder was lower at low carrier density.

The calculated mobility in Fig. 4.9(a) included contributions to scattering from rough interfaces under a self-consistent electric field, alloy disorder in the quantum well, homogeneous background impurities, two-dimensional remote impurities located at the dielectric/III-V interface, three-dimensional remote impurities located in the barriers, and charged dislocations. The functional dependence of mobility on density for sample C was found to be singularly dependent on interface roughness scattering, with fluctuation height $\Delta = 2.7\text{\AA}$ and in-plane correlation length $\Lambda = 9\text{ nm}$, similar to previously reported values[86]. Having assumed the same interface roughness parameters apply to sample A and B, it was found that including alloy scattering with alloy composition $\text{InAs}_{0.987}\text{Sb}_{0.013}$ resulted in good agreement between the calculated and measured mobility for physically reasonable values of the electric field over the quantum wells.

Similar agreement between measurement and calculation could be achieved with ad-

justment to the interface roughness parameters by approximately $\pm 10\%$ of the aforementioned values while the alloy composition was adjusted by ± 0.003 . Neglecting either scattering mechanism did not yield agreement between calculations and measurements for all quantum well widths. The dependence of mobility at a carrier density of approximately $1.33 \times 10^{12} \text{ cm}^{-2}$ on quantum well width is shown in Fig. 4.9(b) for sample A at back gate voltages ranging from 0 V to 1.0 V in increments of 0.2 V, and for samples B and C and a back gate voltage of 0 V. Calculated values of mobility are depicted by the curves for several magnitudes of the average electric field over the quantum well with the dashed curve indicating the case of zero electric field.

The remaining parameters used for scattering calculations were a homogeneous background impurity concentration, $N_{BI} = 1 \times 10^{14} \text{ cm}^{-3}$, remote impurities, $N_{2D,R} = 5 \times 10^{12} \text{ cm}^{-2}$ located at the dielectric/III-V interface, remote impurities, $N_{3D,R} = 1 \times 10^{17} \text{ cm}^{-3}$ distributed through the top and bottom barriers, and a threading dislocation density, $N_{disl} 1 \times 10^6 \text{ cm}^{-2}$. The chosen values of N_{BI} , $N_{2D,R}$, and $N_{3D,R}$ were within the range of experimental estimates of these values. Estimates of background impurities in the channel and barrier materials were based on Hall measurements of bulk layers and secondary ion mass spectrometry of impurities in heterostructures. An estimate of the density of scattering centers at the dielectric/III-V interface was determined by the gating efficiency and is in agreement with reported values for devices using a similar gate metallization technique[87]. The calculated functional dependence of the scattering rate on density by remote impurities, versus distributed remote impurities versus background impurities were similar, and therefore, the level of deviation between calculated and measured mobility similar to that generated for sample A could be obtained by simultaneously varying N_{BI} , $N_{2D,R}$, and $N_{3D,R}$. The agreement between calculated and measured mobility was generally better at low density for lower N_{BI} and higher $N_{2D,R}$ and $N_{3D,R}$.

The density dependence of the mobility in samples D and E was qualitatively similar

to that observed in sample A; however, the magnitude of the mobility at higher carrier density was slightly higher in samples D and E compared to sample A. The carrier density in sample D was increased through occupation of the second sub-band, and a corresponding drop in mobility was observed at carrier densities great than approximately $1.7 \times 10^{12} \text{ cm}^{-2}$. Fig. 4.10 depicts the density dependence of the mobility for samples D and E, the calculated mobility due to individual scattering mechanisms (solid lines), and the total calculated mobility (dashed line).

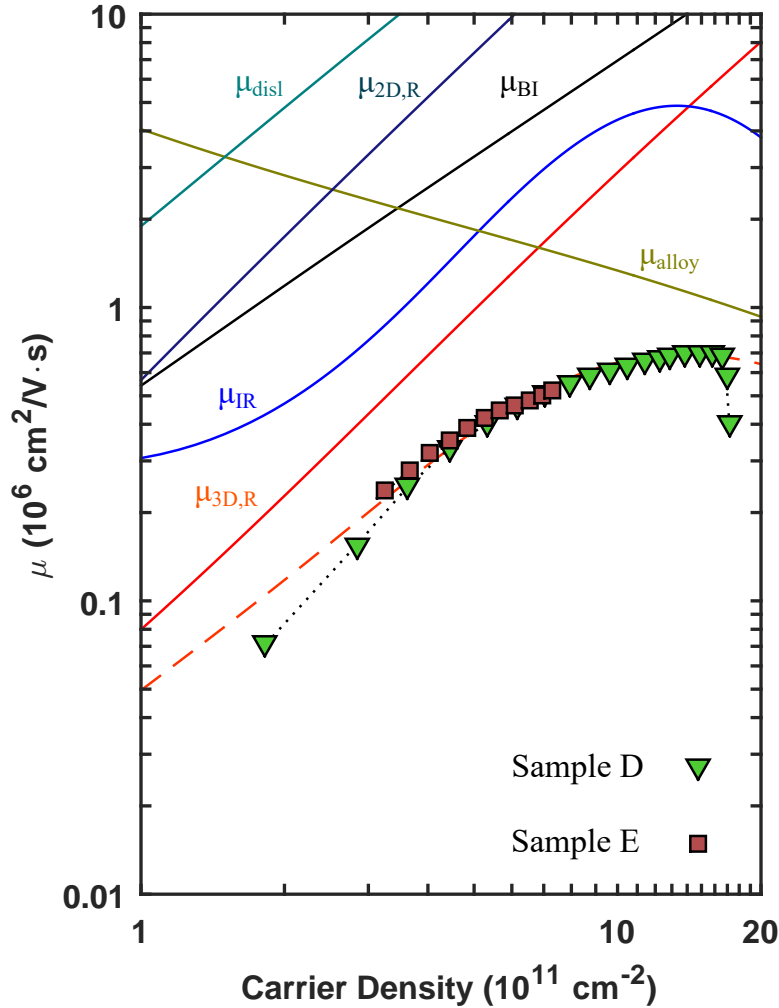


Figure 4.10: The dependence of mobility on carrier density for sample D and E at constant back gate voltage $V_b = 0$ V. The carrier density was changed by varying the front gate, V_f . Mobility limited by individual scattering mechanisms are depicted by solid lines with parameters for interface roughness $\Delta = 2.7 \text{ \AA}$ and $\Lambda = 13.0$ nm, a self-consistent electric field, an alloy composition of $\text{InAs}_{0.988}\text{Sb}_{0.012}$, a homogeneous background impurity concentration, $N_{BI} = 1 \times 10^{14} \text{ cm}^{-3}$, remote impurities, $N_{2D,R} = 5 \times 10^{12} \text{ cm}^{-2}$ located at the dielectric/III-V interface, remote impurities, $N_{3D,R} = 8 \times 10^{16} \text{ cm}^{-3}$, distributed through the top and bottom barriers, and a threading dislocation density, $N_{disl} = 1 \times 10^6 \text{ cm}^{-2}$. The dashed red line indicates the calculated total mobility. A.C.C. Drachmann fabricated the gated Hall bar device and performed the low temperature magnetotransport measurements on sample E.

The calculated mobility overlaying the data for samples D and E assumes a remote

impurity concentration in the barriers, $N_{3D,R} = 8 \times 10^{16} \text{ cm}^{-3}$, an alloy composition of $\text{InAs}_{0.988}\text{Sb}_{0.012}$, and interface roughness parameters, $\Delta = 2.7 \text{ \AA}$ and $\Lambda = 13.0 \text{ nm}$. The remaining parameters were identical to that used for sample A. The similarity in the mobility between sample A and samples D and E suggest shutter sequence I and shutter sequence II yield interfaces of similar quality, and the highly implemented and studied shutter sequence I may not be optimal. Further exploration of growth conditions for the heterointerfaces is merited and will likely be the source of higher mobility at higher carrier density in InAs quantum wells with lattice matched barriers.

At lower carrier density, samples A, D and E observe similar power law dependencies of the mobility on density, $\mu \propto n^\alpha$, with $\alpha \approx 1.3 - 1.6$. Such a power law dependence over the studied range of carrier density is consistent with mobility limited by coulomb scattering from impurities remote to the well[70]. As observed in sample A, in samples D and E increasing the coulomb scattering rate from impurities local to the well by significantly increasing the homogeneous background impurity concentration relative to the value used for the calculations, $N_{BI} = 1 \times 10^{14} \text{ cm}^{-3}$, led to greater discrepancy between calculated mobility and measured values at low carrier density. However, the expected dependence of mobility on density is sensitive to screening of the scattering potential by the 2DEG[70], which itself is sensitive to the relative concentrations and locations of impurities.

Scattering from charged dislocations contributed little to the overall scattering rate. Accounting for scattering by remote impurities located in the barriers, $N_{3D,R}$, at concentrations of order 10^{17} cm^{-3} led to reasonable agreement between calculated mobility and measured mobility at low carrier densities. A concentration of remote impurities in the barriers of the order 10^{17} cm^{-3} is not unrealistic if both donor states and acceptor states are both present and in a ratio that would bring the total donor contribution to the quantum well in agreement with the measured sheet carrier densities. Donor levels

may arise from As_{Al} anti-site defects formed by un-intentional As incorporation in the barriers during MBE growth[29, 88], and numerous intrinsic and extrinsic defects may form in the barriers. Electrically active intrinsic defects with the lowest reported formation energies[89] include interstitial aluminum, $\text{Al}_{i,\text{Al}+1}$, antimony anti-sites, $\text{Sb}_{\text{Al}+1}$, and aluminum vacancies $\text{V}_{\text{Al}-3}$. Extrinsic defects from the common impurities carbon and oxygen are predicted[90] to form primarily acceptor levels from the substitutional defect C_{Sb} and the interstitial defect $\text{O}_{i,\text{tet},\text{Al}}$. Extrinsic and intrinsic defects of both donor and acceptor character are predicted to form over a wide range of chemical potential at temperatures close to the MBE growth temperature.

A final coulombic scattering mechanism is considered: that arising from a two-dimensional layer of charged defects contained at the interface between the barriers and quantum well. Such a model is physically meaningful if the As_{Al} anti-site defects are formed predominantly near the interfaces. Not considering scattering from other mechanisms, a charge density of 10^{11} cm^{-2} shared between the top and bottom interfaces would result in a calculated mobility in agreement with measured values at low carrier density.

The complexity of the system makes it difficult to pinpoint the origin(s) of coulombic scattering dominant at low density. However, the noted sources of charged defects suggest improvements to the quality of the AlSb barriers by optimizing growth conditions and developing techniques to suppress unintentional group V intermixing and alloying may yield higher mobility at lower carrier densities. This work is forthcoming.

4.2.4 Conclusions

The growth and the density dependence of the low temperature mobility of a series of two-dimensional electron systems confined to un-intentionally doped, low extended defect density InAs quantum wells with $\text{Al}_{1-x}\text{Ga}_x\text{Sb}$ barriers has been reported. A gate-tuned

electron mobility exceeding $750,000 \text{ cm}^2/\text{V}\cdot\text{s}$ was achieved at a sample temperature of 2 K. Analysis of the possible scattering mechanisms suggest that at high carrier density within the first occupied electronic sub-band, the mobility was limited by interface roughness and alloy scattering. At low carrier density, the functional dependence of the mobility on carrier density and gate voltage provided evidence of coulomb scattering from charged defects.

4.3 Acknowledgements

This work was supported by Microsoft Research Station Q. This work made use of the central facilities of the UCSB MRL, which is supported by the MRSEC program of the National Science Foundation under Award No. DMR-1121053. This work also made use of the UCSB Nanofabrication Facility, a part of the NSF funded NNIN network, and of the California NanoSystems Institute.

Chapter 5

Gate Control of Spin Orbit Coupling in a High Mobility InAs Quantum Well

Control of zero field spin-splitting is realized in a dual-gated high quality InAs-AlSb two-dimensional electron gas. Magnetotransport experiments showed clean Shubnikov-de Haas oscillations down to low magnetic fields, and the gate-tuned electron transport mobility exceeded $700,000 \text{ cm}^2/\text{V}\cdot\text{s}$. A clear beating effect was observed in magnetoresistance oscillations at large potential asymmetry between gates. Beat patterns due to zero field spin-splitting and other classes of transverse magnetoresistance oscillations were distinguished by temperature dependent magnetoresistance measurements. Analysis of the magnetoresistance oscillations indicated the zero field spin-splitting could be tuned via the Rashba effect while keeping the two-dimensional electron gas charge density constant.

5.1 Introduction

Bychkov and Rashba's description of the lifting of spin degeneracy by spin-orbit interaction in two-dimensional semiconductors[49] has inspired numerous predictions and discoveries regarding the nature of carrier spin in semiconductor heterostructures. Control over spin-orbit interaction in semiconductors is necessary for developing novel spin-based electronics[76, 77, 78] and studying phenomena mediated by spin-orbit coupling[91], which include spin filtering techniques[92, 93], spin-orbit qubits[94, 95], all-semiconductor spin-FETs[96, 97], and topological superconductivity in semiconductor-superconductor heterostructures[79, 80, 8, 52]. In addition to strong spin-orbit coupling, low-dimensional systems require sufficiently high carrier mobility to enable their utilization for quantum information processing[53]. Experimental and technological advances require semiconductor materials that are low in disorder and provide a large degree of control over the spin-splitting energy.

A powerful mechanism that evokes spin-splitting of electronic energy bands uses a combination of inversion asymmetry and spin-orbit interaction. In non-centrosymmetric zinc-blende semiconductors, such as InAs, the lack of an inversion center of symmetry results in a built-in electric field which from the reference frame of a mobile carrier appears as a magnetic field. The bulk inversion asymmetry produces a splitting in both conduction and valence band states mediated by spin-orbit interaction and is referred to as the Dresselhaus effect[48]. Heterostructures of such materials have additional symmetry breaking internal electric fields and can accommodate the application of an external electric field. The structure inversion asymmetry in heterostructures induces an additional energy splitting of spin-degenerate subbands and is referred to as the Rashba effect[49]. The spin-splitting energy due to the Rashba effect in narrow gap semiconductor heterostructures is comparable to or exceeds the spin-splitting energy that results from the

Dresselhaus effect[50]. The magnetic field generated by the Rashba effect is proportional to the expectation value of the electric field within the confinement potential, and the Dresselhaus field is inversely proportional to the thickness of the confined material[51]. The Rashba effect allows the use of an insulated electrostatic gate to modify the electric field over the heterostructure, and in turn, control the spin-splitting energy of the electronic energy bands.

Control over the spin-orbit coupling has been demonstrated in several heterostructures of zinc-blende semiconductors. The Rashba effect was used to control the spin-orbit coupling in an InAs/InAlAs heterostructure using an external gate voltage[98]. The contribution to the spin-splitting energy from asymmetric wave function penetration into barriers was experimentally observed in an asymmetric InAs/InGaAs quantum well[99]. In these experiments, the spin splitting energy was quantified by analyzing the beat patterns in Shubnikov-de Haas (SdH) oscillations. Weak antilocalization analysis of low field magnetoresistance was used to determine the spin splitting energy in asymmetrically doped InAs/InAlAs heterostructures[100]. A gate controlled transition from weak antilocalization to localization allowed the distinction between Rashba, as well as linear and cubic Dresselhaus contributions to the total spin-orbit field in a GaAs heterostructure[101]. In these systems, experimental findings have corroborated theoretical predictions. In contrast, in heterostructures where InAs was confined by AlSb barriers conflicting results have been reported on the ability to control the spin-orbit coupling via modifications to heterostructure asymmetry. Notably, modification of the spin splitting energy was solely attributed to a change in the Fermi wave vector in an insulated gate structure[102]. In addition magnetotransport measurements showed a lack of a beat pattern in Shubnikov-de Haas oscillations in 2DEGs wherein the carrier density and with it the self-consistent electric field were varied by the persistent photoconductivity effect[103]. The nature of spin-splitting in InAs/AlSb heterostructures has remained ambiguous.

5.2 Executive summary

In this work the gate control of spin-orbit coupling is demonstrated in a 2DEG confined to an unintentionally doped InAs/AlSb heterostructure. The high quality of the 2DEG and the integration of both a front and back gate resulted in a gate-tuned electron mobility exceeding $700,000 \text{ cm}^2/\text{V}\cdot\text{s}$. A low magnetic field onset of magnetoresistance oscillations enabled a Fourier analysis of SdH oscillations with high frequency resolution. Beat patterns in the SdH oscillations formed at large potential asymmetry between front and back gates. Beat patterns due to zero-field spin-splitting and magneto-inter-subband scattering were distinguished by temperature dependent magnetoresistance measurements. Analysis of the magnetoresistance oscillations indicated the spin-splitting energy in the first subband depended strongly on the asymmetry induced by the two gates. The analysis was implemented over a wide carrier density regime in this system and determined the spin-splitting energy could be controlled by the Rashba effect while keeping the 2DEG charge density constant.

5.3 Results and discussion

The heterostructure was grown by molecular beam epitaxy (MBE) on a GaSb:Te (001) substrate mounted to a molybdenum substrate holder using gallium. Prior to the growth of the heterostructure the oxide was thermally desorbed under atomic hydrogen in a custom ultra-high-vacuum preparation chamber with a base pressure of 2×10^{-10} mbar. During the 30 minute desorption procedure, the chamber pressure was maintained at 3×10^{-6} mbar by adjusting the hydrogen flow rate through an atomic hydrogen source operating at $1900 \text{ }^\circ\text{C}$. The substrate thermocouple was maintained at $500 \text{ }^\circ\text{C}$. The configuration of the substrate, substrate heater and thermocouple was such that the true

substrate temperature was likely lower than the temperature measured by the thermocouple. Following oxide desorption, the substrate was transferred in-situ to a modified VG V80H for the growth of the heterostructure.

In a previous work it was reported that carrier mobility and single particle lifetime in InAs/(Al,Ga)Sb heterostructures are sensitive to the dislocation density in the epitaxial layers[19]. Therefore, the growth proceeded with a 20 nm GaSb buffer and a 200 nm AlAs_{0.09}Sb_{0.91} epitaxial film to act as an electrically isolating, lattice matched buffer between the conductive GaSb:Te substrate and the InAs channel. The growth followed the AlAs_{0.09}Sb_{0.91} buffer with a ten period 2.5 nm AlSb \times 2.5 nm GaSb superlattice, over the course of which reflection high energy electron diffraction oscillations were monitored to verify calibrated growth rates and a layer by layer growth mode for both AlSb and GaSb. Following the superlattice the growth proceeded with a 30 nm AlSb bottom barrier, a 15 nm InAs channel, and a 50 nm AlSb top barrier. The interfaces between the InAs channel and the barriers were formed using a shutter sequence developed by Tuttle and co-workers[29]. The structure was terminated with a 3 nm GaSb capping layer to prevent the oxidation of the Al-containing layers. A schematic of the heterostructure is shown in Fig. 5.1(a).

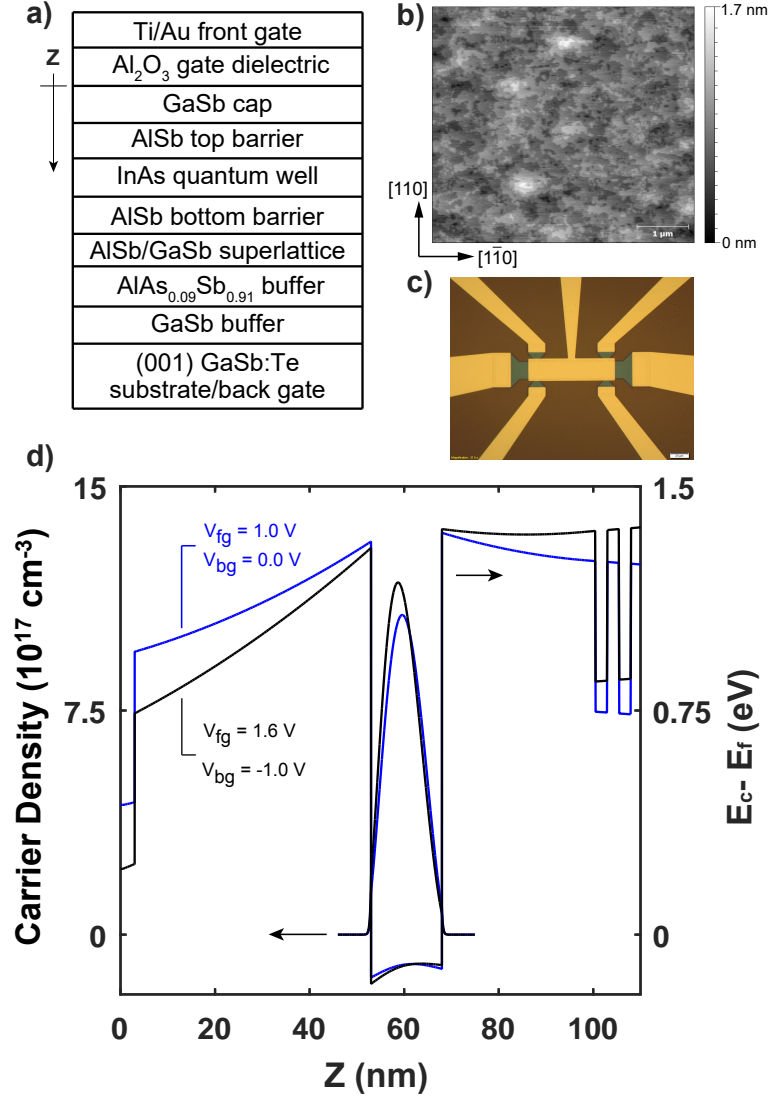


Figure 5.1: (a) A schematic of the InAs quantum well heterostructure with Al₂O₃ gate dielectric and Ti/Au front gate. (b) A $5 \times 5 \mu\text{m}^2$ atomic force microscope image of the heterostructure taken at the surface of the GaSb capping layer. (c) An optical micrograph of the Hall bar used in this study. The scale bar at the lower right represents $20 \mu\text{m}$. (d) A self-consistent calculation of the conduction band profile and carrier density distribution in the vicinity of the InAs quantum well when $V_{fg} = 1 \text{ V}$ and $V_{bg} = 0 \text{ V}$ (blue lines), and when $V_{fg} = 1.6 \text{ V}$ and $V_{bg} = -1 \text{ V}$ (black lines). See text for details of the calculation.

The surface of the MBE grown film appeared flat when examined under a Nomarski microscope at $100\times$ magnification. Atomic force microscopy (AFM) of the surface re-

vealed height variations corresponding to GaSb monolayer-height steps (0.3 nm). The root-mean-square roughness[104] of the $5 \mu\text{m} \times 5 \mu\text{m}$ AFM image shown in Fig. 5.1(b) is 0.18 nm.

A gated Hall bar device with dimensions $80 \mu\text{m} \times 20 \mu\text{m}$ was fabricated using standard microfabrication techniques. Following mesa definition by wet chemical etching, 50 nm of Al_2O_3 was grown by atomic layer deposition to serve as the top gate dielectric. To avoid an electrical short to the substrate, openings for the ohmic contacts were formed by first etching vias through the gate dielectric, then through the top antimonide barrier and stopping on the InAs channel. Ti/Au was deposited by electron beam evaporation to serve as both ohmic and gate metallization. An optical micrograph of the device is shown in Fig. 5.1(c).

Longitudinal resistance was measured in the [1-10] crystallographic direction. Measurements were performed at cryogenic temperatures in a He-4 cryostat using standard lock-in techniques under an excitation current of $1 \mu\text{A}$. The 2DEG carrier density varied linearly under both back and front gate operation.

The integration of a front and back gate allowed independent control of the electric field over the quantum well and the 2DEG carrier density. A self-consistent calculation of the Schrodinger and Poisson equations[17] allowed the study of the conduction and valence band profiles, carrier density distributions, and the expectation value of the electric field over the quantum well in the gated hall bar device under gate operation. Band parameters reported by Vurgaftman et al.[15] were used for the III-V heterostructure, and parameters reported by Huang et al.[69] were used for the ALD grown Al_2O_3 gate dielectric. These parameters are summarized in Appendix H. The conduction band profile and carrier density distribution in the vicinity of the InAs channel for two combinations of front and back gate voltages are depicted in Fig. 5.1(d). The origin of the growth axis was chosen to be the interface of the GaSb capping layer and the Al_2O_3 gate dielectric.

The electron density is maintained near $\approx 1 \times 10^{12} \text{ cm}^{-2}$ at two different back and front gate voltage combinations.

The magnetoresistivity, shown in Fig. 5.2(a), was calculated from the measurement of the magnetoresistance at multiple front gate voltages, V_{fg} , while the back gate voltage was fixed at $V_{bg} = 0 \text{ V}$ and at multiple back gate voltages while the front gate voltage was fixed at $V_{fg} = 1 \text{ V}$.

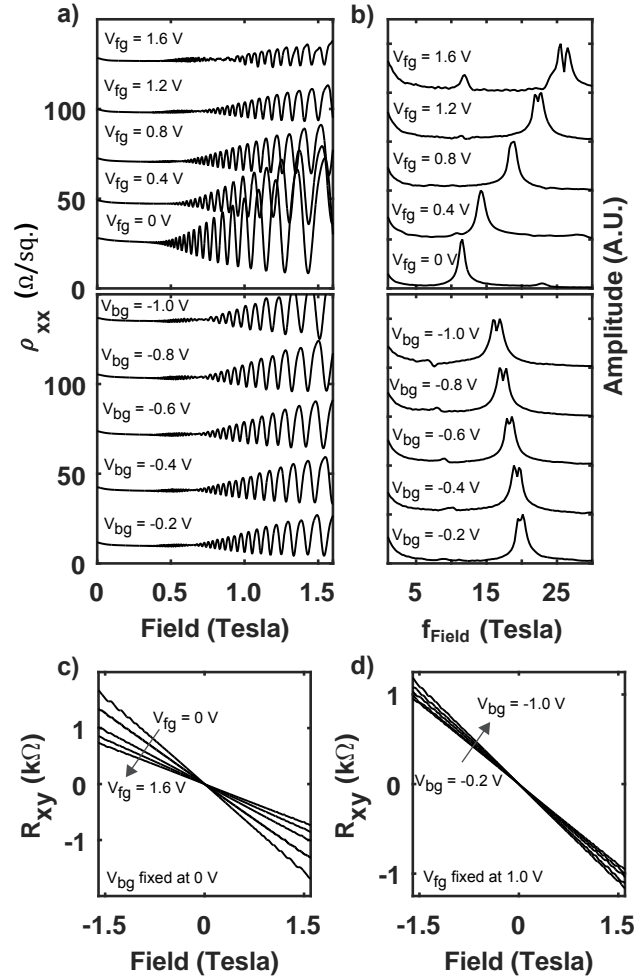


Figure 5.2: (a) Magnetoresistivity at $V_{fg} = 0, 0.4, 0.8, 1.2,$ and 1.6 V while $V_{bg} = 0$ V (upper plot), and at $V_{bg} = 0.2, 0.4, 0.6, 0.8$ and 1 V while $V_{fg} = 1$ V (lower plot). (b) Fourier amplitude versus magnetoresistance oscillation frequency determined from a Fourier analysis of the corresponding magnetoresistance in (a) as a function of inverse magnetic field. The data in (a) and (b) are offset for clarity. (c) Hall resistance at $V_{fg} = 0, 0.4, 0.8, 1.2,$ and 1.6 V while $V_{bg} = 0$ V. (d) Hall resistance at $V_{bg} = 0.2, 0.4, 0.6, 0.8,$ and 1 V while $V_{fg} = 1$ V. Measurements were performed at a sample temperature of 2 K.

A clear beat pattern was observed in the SdH oscillations upon application of gate voltages to the front or back gate, and the beating effect became more pronounced as the potential asymmetry between front and back gates was increased. The beating was determined to be due to two narrowly separated oscillation frequencies by a Fourier

analysis (FA) of the SdH oscillations. The FA is depicted in Fig. 5.2(b) for each of the measurements in Fig. 5.2(a). The Hall resistances corresponding to the measurements in Fig. 5.2(a) are plotted in Fig. 5.2(c) and 5.2(d).

The electron mobility, μ , exceeded 700,000 cm²/V·s when the carrier density, N_s , was gated-tuned to $\approx 1.2 \times 10^{12}$ cm⁻², determined from $\mu = 1/\rho_o N_s e$, where ρ_o is the zero magnetic field resistivity and e is the elementary charge. The dependence of mobility on density at several fixed back gate voltages is shown in Fig. 5.3(a).

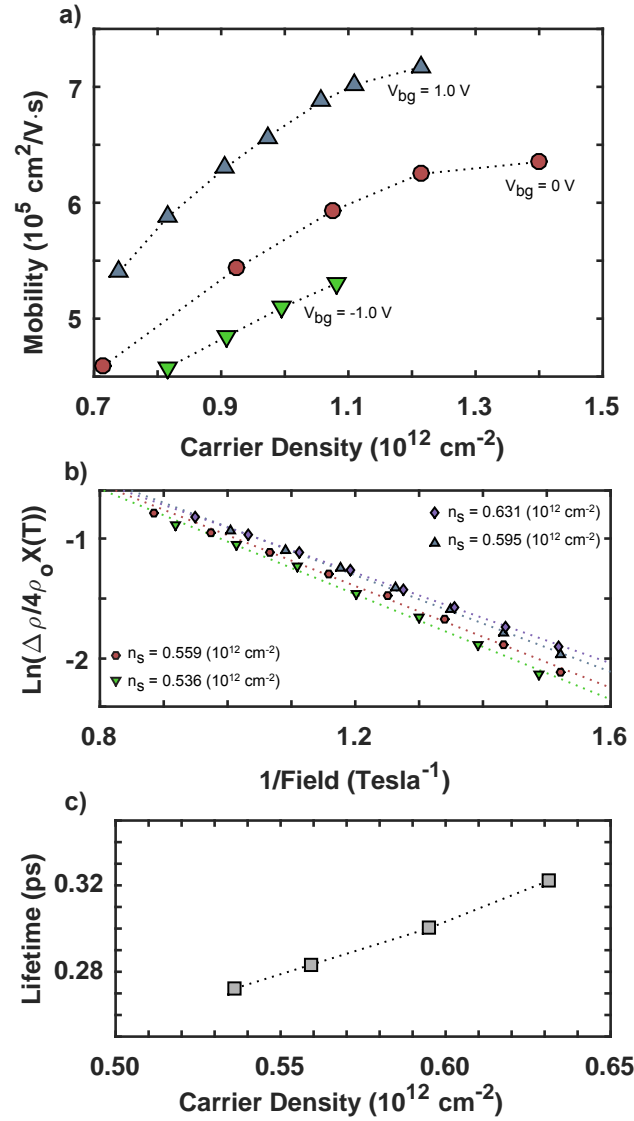


Figure 5.3: (a) The dependence of mobility on carrier density at a sample temperature of 2 K and at constant back gate voltages $V_{bg} = 1, 0,$ and $+1 \text{ V}$. The carrier density was varied using the front gate, where in each case an increase in the front gate voltage corresponds to an increase in carrier density. (b) Dingle analysis of the SdH oscillations at a sample temperature of 2 K and at four carrier densities near zero gate bias. The carrier density was modulated using the back gate. Linear fits are shown as dotted lines. (c) The dependence of quantum lifetime on carrier density determined from the data in (b).

The density was varied by the front gate voltage. For a given carrier density the mobility could be increased by applying a positive bias to both the front and back gate

in comparison to applying a positive bias to only the front gate. This observation can be explained by the creation of a more symmetric quantum well potential for the latter case and a corresponding centered wave function with a reduced scattering rate from rough interfaces. The change in mobility as a function of carrier density has a weaker dependence on back gate voltage at lower carrier density ($< 0.6 \times 10^{12} \text{ cm}^{-2}$). The mobility may be limited by scattering mechanisms less sensitive to wave function position in this carrier density regime.

When the 2DEG carrier density was gate tuned to $\approx 8 \times 10^{11} \text{ cm}^{-2}$, the onset of SdH oscillations occurred slightly below 0.27 Tesla. This onset corresponds to a Dingle mobility, D , of $37,000 \text{ cm}^2/\text{V}\cdot\text{s}$ and a Dingle temperature, $T_D = e\hbar/(2\pi k_B m^* \mu_D)$, of 1.7 K. Here, k_B is the Boltzmann constant, and m^* the zero-field effective mass. The quantum lifetime of the 2DEG at carrier densities near zero gate voltage was determined using a Dingle analysis of the SdH oscillations [105] over the magnetic field range 0.6 T to 1 T. The amplitude of the oscillations, $\Delta\rho$, is given by $\Delta\rho = 4\rho_o X(T) \exp(-\pi/\omega_c \tau_q)$, where ρ_o is the zero-field longitudinal magnetoresistance, and $X(T) = (2\pi^2 k_B T / \hbar \omega_c) / \sinh(2\pi^2 k_B T / \hbar \omega_c)$ is a function of temperature, T , and $\omega_c = eB/m^*$, where B is the magnetic field. At zero gate bias m^* was determined to be $0.032m_e$ from analysis of SdH oscillation amplitudes as a function of temperature. The measurement of the effective mass was in agreement with an estimate using $\mathbf{k}\cdot\mathbf{p}$ formalism accounting for band non-parabolicity [66]. Calculated values were used to account for the effective mass dependence on density. The Dingle analysis at several carrier densities gate-tuned using the back gate is shown in Fig. 5.3(b) along with linear fits to the data. The slight curvature in the Dingle plots with respect to the linear fits may be due to non-parabolicity and competing spin-orbit-coupling and Zeeman effects on the Landau level spectrum. The curvature and the fits $1/\text{Field} = 0$ intercepts being greater than 0 may also be due to the presence of a spread in carrier density [65] and field-dependent

dephasing. The Dingle analysis does not show evidence of second subband occupation or sample inhomogeneity[65]. The slope of the linear fit provides an estimate of the quantum lifetime at the given carrier density. The quantum lifetime is plotted versus carrier density in Fig. 5.3(c). The dependence of quantum lifetime on carrier density may be due to a suppression of small-angle-scattering from remote ionized donors upon increasing carrier density[65].

The low magnetic field magnetoresistance oscillations allowed analysis of beat patterns with high frequency resolution. In addition to spin-split subbands, several other mechanisms result in magnetoresistance oscillations with characteristic frequencies; they include magnetophonon resonances (MPR)[106, 107, 108] and magneto-intersubband scattering (MIS)[109, 71, 110]. Magnetoresistance oscillations characteristic of MPR and MIS were observed when the 2DEG carrier density was gate-tuned above $1.1 \times 10^{12} \text{ cm}^{-2}$ in addition to oscillations due to spin-split subbands.

Beat patterns due to spin-split subbands, MPR and MIS were distinguished by measurements of the temperature dependence of the magnetoresistance oscillations and by magnetotransport measurements. MPR and MIS scattering persists in the presence of significant thermal excitation whereas SdH amplitudes decrease rapidly with increasing temperature. The longitudinal magnetoresistance measured at two front gate voltages and at several temperatures for each gate voltage are shown in Fig. 5.4(a). The FA of the respective magnetoresistance oscillations are shown in Fig. 5.4(b).

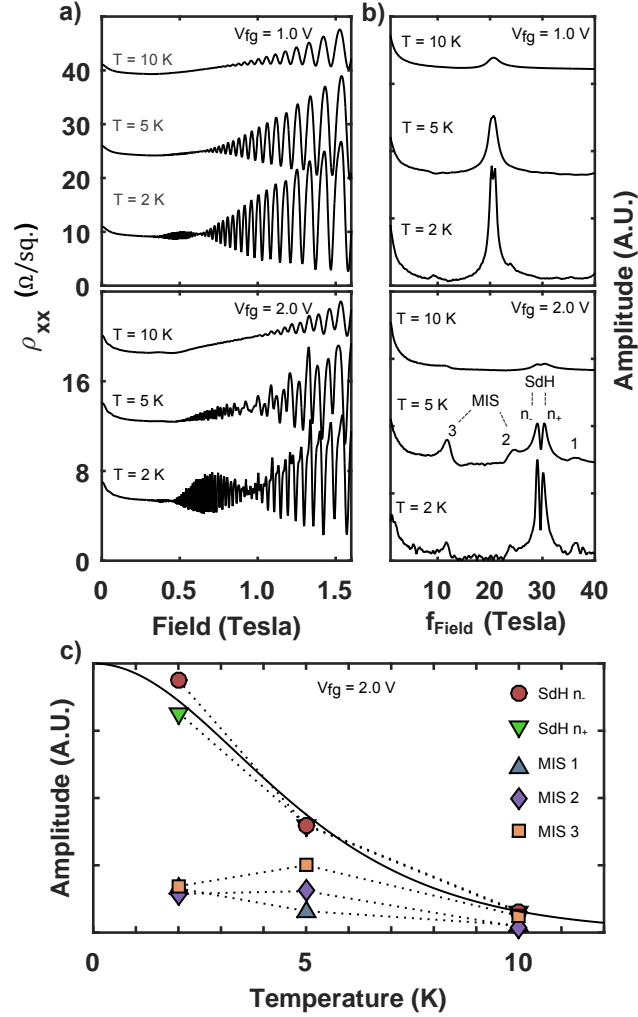


Figure 5.4: (a) Magnetoresistivity at sample temperatures 2, 5, and 10 K for $V_{fg} = 1.0$ V (upper plot) and 2.0 V (lower plot). (b) Fourier amplitude versus magnetoresistance oscillation frequency determined from a Fourier analysis of the corresponding magnetoresistance in (a) as a function of inverse magnetic field. The data in (a) and (b) are offset for clarity. (c) The temperature dependence of the Fourier amplitudes denoted by SdH n_+ , SdH n_- , MIS 1, 2, and 3 in the Fourier analysis shown in (b) for the front gate voltage $V_{fg} = 2.0$ V. The solid line depicts the theoretical temperature dependence of SdH Fourier amplitudes, $\approx (2\pi^2 k_B T / \hbar \omega_c) / \sinh(2\pi^2 k_B T / \hbar \omega_c)$.

At $V_{fg} = 1.0$ V and $T = 2$ K two narrowly separated oscillation frequencies are observed at $f_{\text{Field}} \approx 20$ T. The temperature dependence of the amplitudes of the peaks near 20 T were consistent with the temperature dependence predicted for SdH oscillations. Three additional oscillation frequencies at approximately 12 T, 24 T, and 36 T were also

observed. The amplitudes of the Fourier peaks located at 12, 24, 36 T slightly decreased or increased as a function of temperature when the front gate was tuned to $V_{fg} = 2.0$ V; furthermore, the frequencies of the peaks at 12 and 24 T, which could be resolved at the lower applied gate voltages, were weakly dependent on the gate voltage, suggesting the corresponding oscillations were not due to the SdH effect. The temperature dependence of the Fourier peaks labeled SdH n_+ , SdH n_- , 1, 2 and 3 are compared in Fig. 5.4(c). The amplitudes of SdH n_+ and SdH n_- have a functional dependence on temperature that matches the prediction for SdH oscillations depicted by the solid black line. Fourier peaks 1, 2 and 3 have a weak temperature dependence. Furthermore, when the density was gate-tuned such that the SdH peaks surpassed peak 1 at 36 Tesla, the mobility decreased by approximately $200,000 \text{ cm}^2/\text{V}\cdot\text{s}$ per increase in density by 10^{11} cm^{-2} , suggesting the field at peak 1 corresponds to the MIS fundamental field[110], $f_{Field,MIS1} = E_{12}m^*/e\hbar$, where $E_{12} = E_2 - E_1$ is the subband spacing. The subband spacing determined from the MIS fundamental field is 107 meV. A calculated value for E_{12} is 127 meV. Peaks 2 and 3 are attributed to MPRs.

The narrowly separated SdH oscillation frequencies are interpreted to be due to spin-split subbands. The oscillation frequency of each peak in the FA amplitude provides the population of each spin split subband n_+ and n_- by $n_{\pm} = (ef_{Field})/h$. The total carrier density determined by the low field Hall resistance is in good agreement with the density determined by the FA frequencies of the spin-split subbands. Restricting the experiment and analysis to the first occupied subband the Rashba spin orbit coupling parameter is determined by[111]

$$\alpha = \frac{(n_+ - n_-)\hbar^2}{m^*} \sqrt{\frac{\pi}{2N_s - 2(n_+ - n_-)}}. \quad (5.1)$$

The experimentally determined Rashba spin orbit coupling parameter, α , versus carrier density measured at a multiple back gate and front gate voltage combinations is shown

in Fig. 5.5.

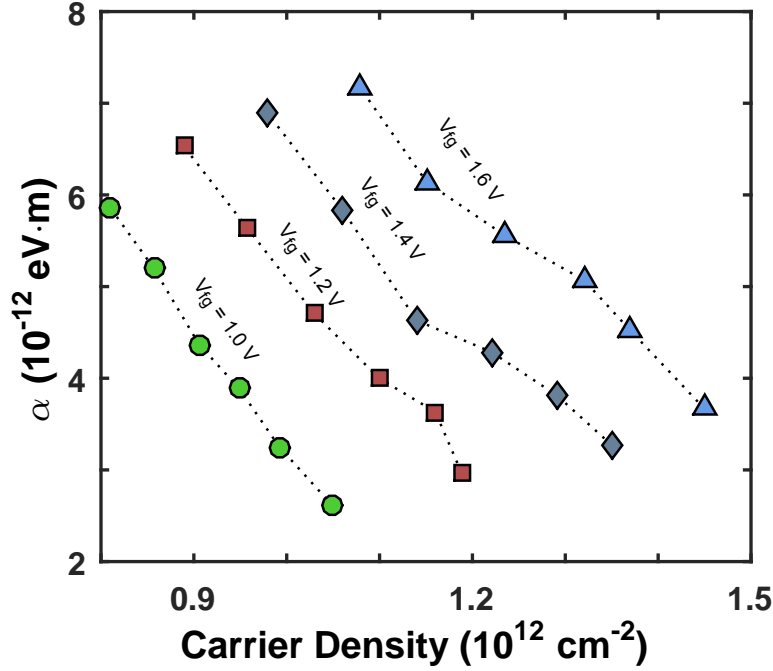


Figure 5.5: Experimentally determined Rashba spin-orbit coupling parameter versus carrier density. The data are grouped by common fixed front gate voltage. For a given front gate voltage the back gate voltage was varied from 0 to 1.0 V in 0.2 V increments.

The data is grouped by a common fixed front gate voltage. For a given front gate voltage the density was changed by varying the back gate voltage from 0 V to -1.0 V in 0.2 V increments. An increase in the difference between the back and front gate voltages generated an increase in α , and α could be increased at constant carrier density by appropriate set points of the back and front gate voltages.

The expectation value of the electric field, $\langle E \rangle$, over the quantum well varied between 20 kV/cm and 50 kV/cm for gate voltage combinations having the lowest and highest potential asymmetry, respectively. A scaling factor, b , that parameterizes the spin-orbit interaction parameter, $\alpha = b\langle E \rangle$, at constant carrier density was approximately 170 $e\text{\AA}^2$ electric quadrupole moments. This value is notably larger than the electric field

contribution of the spin-splitting parameter resulting from the quantum well alone[112], which is calculated to be $120 e\text{\AA}^2$ for the InAs/AlSb quantum well under investigation, and suggests interface contributions to the zero-field spin-splitting energy were significant.

The strong dependence of α on the gate-controlled potential asymmetry suggests the structure inversion asymmetry contribution to the total spin orbit interaction was controlled by the Rashba mechanism. This finding is in contrast with previous results[102, 103]; however, by using 2DEGs with exceptionally high mobility and implementing electric field control by integrating both a back and front gate this work was able to resolve finer changes in the spin splitting energy and probe a previously unexplored range of potential asymmetry and carrier density in this system. In addition to offering technological advances for studies in Spintronics and related fields, the back and front gated high mobility 2DEG confined to the InAs/AlSb heterostructure enables the investigation of a system wherein phenomena inherent to high carrier mobility two-dimensional semiconductors and to narrow band gap semiconductors with tunable spin-orbit coupling coexist.

5.4 Conclusion

This work has demonstrated the gate control of zero field spin-splitting in a high quality back and front gated InAs-AlSb heterostructure. Magnetotransport experiments on a high mobility 2DEG confined to the InAs channel showed clean Shubnikov de Haas oscillations down to low magnetic fields. Analysis of the magnetoresistance oscillations indicated the spin-splitting energy in the first subband was controlled by front and back gates via the Rashba effect. The spin-splitting energy could be modified while keeping the 2DEG charge density constant.

5.5 Acknowledgements

This work was supported by Microsoft Research Station Q. This work made use of the central facilities of the UCSB MRL, which is supported by the MRSEC program of the National Science Foundation under Award No. DMR-1121053. This work also made use of the UCSB Nanofabrication Facility, a part of the NSF funded NNIN network, and of the California NanoSystems Institute. Experiments performed under proposal P02254 at the National High Magnetic Field Laboratory, which is supported by NSF Cooperative Agreement No. DMR-1157490, the State of Florida, and the U.S. DOE, contributed to this work.

Chapter 6

Materials Considerations for Forming the Topological Insulator Phase in InAs/GaSb Heterostructures

The temperature and magnetic field dependence of the resistance of a dual-gated InAs/GaSb heterostructure gate-tuned through the inverted to normal gap regimes is reported. The resistance maxima monotonically decreased with increasing temperature over the entire phase diagram. A large positive magnetoresistance was observed when the structure was gate-tuned to the inverted regime. Conduction in the inverted (predicted topological) regime was qualitatively similar to behavior in a disordered two-dimensional system. The impact of disorder on the formation of topologically protected edge states and an insulating bulk were considered. Potential fluctuations in the electronic band structure for realistic levels of disorder were calculated using a gated heterostructure model. Potential fluctuations were estimated to be sufficiently strong such that conduction in the

predicted topological insulator (TI) regime was likely dominated by a symplectic metal phase rather than a TI phase. The implications are that future efforts must address disorder in this system and focus must be placed on the reduction of defects and disorder in these heterostructures if a TI regime is to be achieved.

6.1 Introduction

The prediction of the existence of a topologically non-trivial, or quantum spin Hall (QSH) insulator, phase in InAs/GaSb heterostructures[18], introduced in Ch. 3.1, has significant implications for fault-tolerant quantum information processing[9]. The prospect of implementing quantum computing architectures on technologically mature III-V requires topologically protected helical edge channels and an insulating bulk in InAs/GaSb heterostructures.

Evidence supporting the existence of helical edge states has been found in observations of conductance quantized near predicted values for single mode conduction and measured in both local and non-local configurations[113, 56, 114, 115]. In some of these experiments silicon or beryllium doping was required to suppress bulk conductivity[114, 115]. These experiments confirm conduction close to quantized values over micron-sized device geometries but do not incontrovertibly confirm helicity. Furthermore, they report suppressed bulk conduction, but do not confirm if the bilayer structure was tuned to the inverted gap regime. Additional evidence supporting the existence of helical edge states is lacking. In particular, reports on the temperature dependence of the conductivity when the Fermi level was interpreted to be in the hybridization gap showed it to be stagnant with changes in temperature[56, 114, 115] or to increase with increasing temperature[116], and are in disagreement with theoretical expectations for conduction through helical edge states[117].

6.2 Executive Summary

This chapter reports on the temperature dependence of the resistance of a dual-gated 11 nm InAs / 8 nm GaSb heterostructure gate-tuned through the inverted to normal gap regimes. The inverted and normal regimes were identified by measurements of the evolution of resistance as a function of the two gates and under in-plane and out-of-plane magnetic fields. The resistance maxima monotonically decreased with increasing temperature over the entire phase diagram. A large positive magnetoresistance was observed when the structure was gate-tuned to the inverted regime. Conduction in the inverted (predicted TI) regime was qualitatively similar to behavior in a disordered two-dimensional system. The impact of disorder on the formation of topologically protected edge states and an insulating bulk were considered. Potential fluctuations in the electronic band structure for realistic levels of disorder were calculated using a gated heterostructure model. Potential fluctuations were estimated to be sufficiently strong such that conduction in the predicted TI regime was likely dominated by a symplectic metal phase rather than a TI phase.

6.3 Results and Discussion

The 11 nm InAs / 8 nm GaSb bilayer heterostructure was grown by molecular beam epitaxy on a GaSb:Te (001) substrate. A schematic of the heterostructure, with integrated 50 nm Al_2O_3 gate dielectric and Ti/Au gate metallization is shown in Fig. 6.1(a). The bilayer heterostructure is surrounded by a 50 nm AlSb top barrier and a 30 nm AlSb bottom barrier, a 10 period 2.5 nm AlSb / 2.5 nm GaSb superlattice and a 100 nm $\text{AlAs}_{0.1}\text{Sb}_{0.9}$ electrically insulating buffer. This dual-gated device structure was shown in Ch. 5 and reference [20] to linearly vary the electron density in single InAs quantum

wells with both the Ti/Au front gate, V_f , and the GaSb:Te back gate, V_b over a wide gate voltage range. A calculated in-plane dispersion of a coupled electron-hole quantum well representing the heterostructure under study is shown in Fig. 6.1(b).

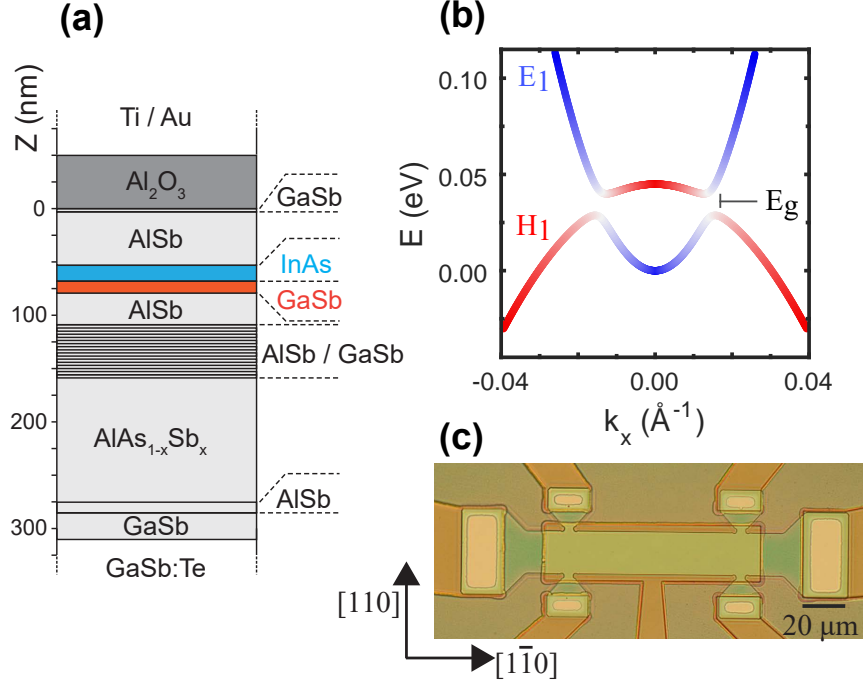


Figure 6.1: (a) A schematic of the 11 nm InAs / 8 nm GaSb bilayer heterostructure with Al₂O₃ gate dielectric and Ti/Au front gate. (b) The calculated in-plane dispersion including the hybridization effect for the InAs/GaSb bilayer in the inverted regime. Here, the H₁ subband is assumed to be 50 meV above the lowest electron subband, E₁. (c) An optical micrograph of the 80×20 μm² Hall bar device used in this study prior to gate and ohmic metallization. The long axis of the hall bar is oriented along the [1-10] crystallographic direction.

Here, the hybridization effect was included, resulting in the formation of a hybridization gap of size E_g , and the structure was modeled to be in the inverted regime wherein the H₁ subband was set 50 meV above the lowest electron subband, E₁ at zone center. A dual gated Hall bar device fabricated over the heterostructure is shown in Fig. 6.1(c). The dual gated device allows for control of the subband levels, enabling the electronic structure to be tuned from a normal gap dispersion where the minimum of E₁ is higher

in energy than the maximum of H_1 to an inverted gap dispersion where the minimum of E_1 is lower in energy than the maximum of H_1 , while independently controlling the Fermi level[32, 118].

Measurements were performed using standard lock-in techniques under an excitation current of 1 nA and 10 nA and at cryogenic temperatures in an adiabatic demagnetization refrigerator with a base temperature of 50 mK, a He-4 cryostat with a base temperature of 1.8 K, and a dilution refrigerator equipped with a sample tilter with a base temperature of 20 mK. In all systems, the device was cooled under zero gate bias.

The dependence of the longitudinal resistance on the front and back gate voltages at a sample temperature of 165 mK is shown in Fig. 6.2(a).

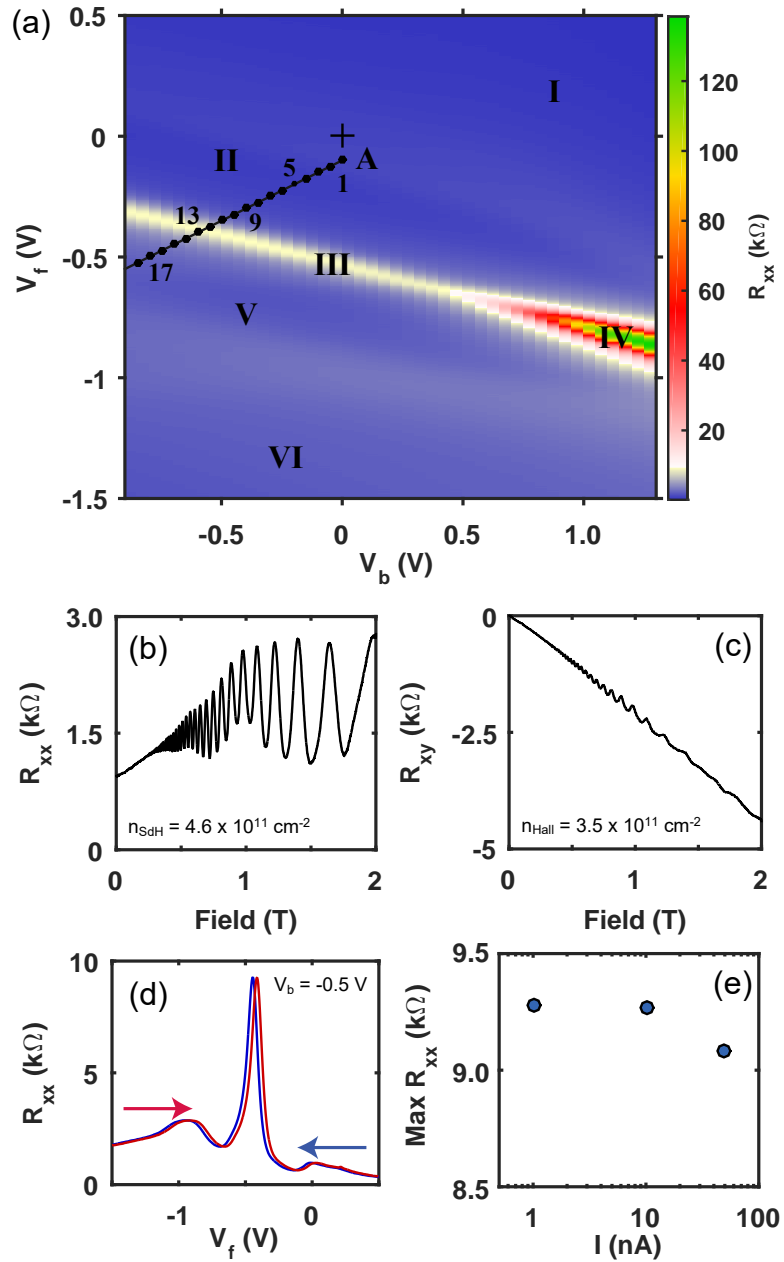


Figure 6.2: (a) The dependence of longitudinal resistance on front and back gate voltages at a sample temperature of 165 mK. Line A, spanning regions II and V, follows an estimate of constant electric field over the InAs/GaSb heterostructure across the inverted gap. (b) Magnetoresistance measured at zero gate bias. (c) Hall magnetoresistance measured at zero gate bias. (d) Longitudinal resistance as a function for front gate at a fixed back gate of -0.5 V for decreasing and increasing front gate voltage sweeps. (e) The maximum value of the longitudinal resistance as a function of excitation current measured as the front gate is modulated as in (d) at a fixed back gate -0.5 V.

The resistance map is divided into several regions surrounding and including a line of maximum resistance which itself observes a minimum value of approximately $7 \text{ k}\Omega$ at $V_b \approx 0.35 \text{ V}$, $V_f \approx -0.55 \text{ V}$. The (+) near the center of the map indicates the origin in gate space. Longitudinal and Hall magnetoresistance measurements, as shown for zero gate bias in Fig. 6.2(b) and Fig. 6.2(c), were used to determine the evolution of carrier density as a function of V_f and V_b . The channel resistance was measured by modulating the front gate at fixed back gate. The hysteresis in modulating the front gate is shown in Fig. 6.2(d). The current dependence of the channel resistance maximum over a front gate sweep at a fixed back gate of -0.5 V is shown in Fig. 6.2(e).

Longitudinal and Hall magnetoresistance measurements identified transport in region I in Fig. 6.2(a) as being electron dominated with electron mobility exceeding $200,000 \text{ cm}^2/\text{V}\cdot\text{s}$. Region II showed mixed conduction with majority n-type carriers. Conduction in region V was of mixed type but through majority p-type carriers. Conduction in region VI was dominated by holes with mobility exceeding $20,000 \text{ cm}^2/\text{V}\cdot\text{s}$. Magnetoresistance was measured at twenty-one points along line A, which approximately followed a line of constant electric field. A subset of the magnetoresistance measurements along line A in Fig. 6.2(a) are shown in Fig. 6.3(a) and 6.3(b), and the longitudinal resistance, extracted carrier density and carrier type are shown in Fig. 6.3(c).

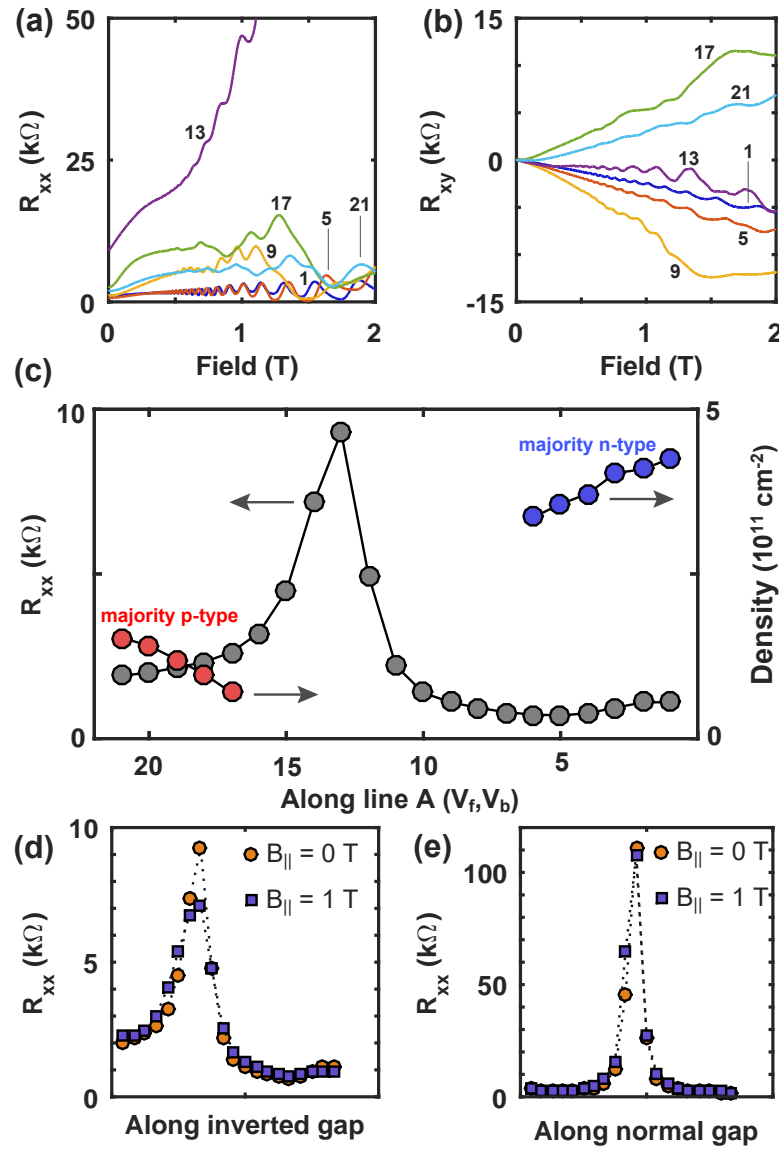


Figure 6.3: (a) The longitudinal magnetoresistance measured along several points along line A. (b) The Hall magnetoresistance measured along several points along line A in Fig. 6.2(a). (c) Longitudinal resistance and carrier density measured along line A. (d) Longitudinal resistance along line A at 0 T and 1 T in-plane magnetic fields. (e) Longitudinal resistance along a line approximately parallel to line A over the normal gap regime (region IV) and at 0 T and 1 T in-plane magnetic fields.

Measurements were performed under in-plane magnetic field perpendicular to the current path of the Hall bar at a sample temperature of 165 mK. The dependence of the resistance along line A at 0 T and 1 T in-plane magnetic field is shown in Fig.

6.3(d). The resistance was found to decrease as a function of magnetic field along line A, and identifies region III as having an inverted subband structure[35, 119]. The same measurement was performed across region IV with gate voltage modulated using a similar slope as that of line A, and is shown in Fig. 6.3(e). The relative change in the resistance as a function of in-plane magnetic field was significantly less over region IV and suggests the presence of a normal gap subband structure over region IV. The Hall voltage as a function of in-plane magnetic field was used to determine a misalignment of the in-plane magnetic field of approximately 2 degrees. Similar in-plane magnetic field measurements were performed in a dilution refrigerator at a sample temperature of 20 mK to verify the subband structure. A sample tilter enabled near perfect in-plane field alignment. In this configuration the resistance maximum in region III as a function of in-plane magnetic field was measured in 0.25 T increments from 0 T to 4 T and was found to monotonically decrease. The resistance maximum measured in region IV slightly increased over the same magnetic field range. The resistance minimum along the line of maximum resistance at $V_b \approx 0.35$ V, $V_f \approx -0.55$ V was interpreted to be due to a gap closing in the subband structure.

The progression of the subband structure under gate operation is summarized in Fig. 6.4. The calculated in-plane dispersion including the hybridization effect for the InAs/GaSb bilayer in the inverted regime is shown in Fig. 6.4(a). The dispersion and three distinct Fermi level positions, lines 1, 2 and 3 approximate the evolution of the system traveling from regions II to III to V in Fig. 6.2(a). The calculated in-plane dispersion InAs/GaSb bilayer in the normal regime is shown in Fig. 6.4(b). The dispersion and three distinct Fermi level positions, lines 1, 2 and 3 approximate the evolution of the system traveling from regions I to IV to VI in Fig. 6.2(a).

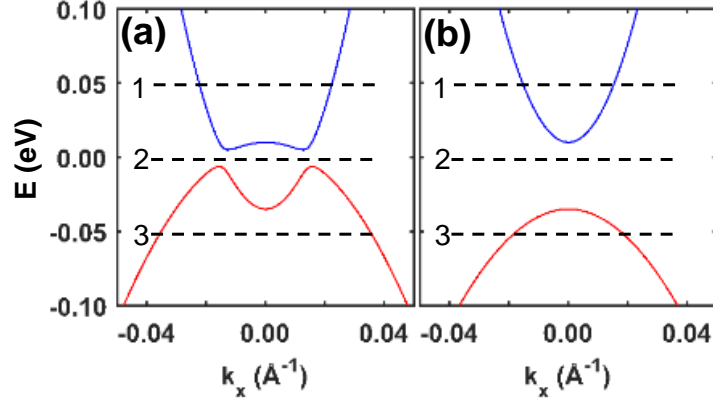


Figure 6.4: (a) The calculated in-plane dispersion including the hybridization effect for the InAs/GaSb bilayer in the inverted regime. The dispersion and three distinct Fermi level positions, lines 1, 2 and 3 approximate the evolution of the system traveling from regions II to III to V in Fig. 6.2(a). (b) The calculated in-plane dispersion InAs/GaSb bilayer in the normal regime. The dispersion and three distinct Fermi level positions, lines 1, 2 and 3 approximate the evolution of the system traveling from regions I to IV to VI in Fig. 6.2(a).

An approximation of the size of the hybridization gap was obtained by the ratio of the change in density across the gap over the density of states, and a range of $E_g = (\pi\hbar^2\Delta n)/m^* = 2.7 \text{ meV} - 8.5 \text{ meV}$ was determined, where Δn was estimated to be $5 \times 10^{10} \text{ cm}^{-2}$ to $1.6 \times 10^{11} \text{ cm}^{-2}$ by extrapolating the carrier density and the associated error in its measurement far from the gap to points 11 and 14 along line A and straddling the gap. An effective mass is estimated as $m^* = 0.035m_e$ from the temperature dependence of Shubnikov de Haas oscillations measured in the electron dominated regime up to a sample temperature of 20 K.

The resistance maxima in the space of gate voltages yielding a hybridized band structure and with the Fermi level tuned to the hybridized gap are of the order 8 k Ω . This value is far below the expected value of several multiples of h/e^2 for conduction in long helical edges in which the phase coherence length is assumed to be smaller than the physical edge length of 80 μm . The temperature dependence of the resistance maxima of

the longitudinal resistance measured by modulation of V_f at several fixed V_b is shown in Fig. 6.5(a). For $V_b = -0.7$ V and $V_b = 0.2$ V, the dispersion is hybridized. For V_b equal to and greater than 0.4 V, the conduction is measured through a normal gap. Fig. 6.5(b) shows the temperature dependence at several additional back gate voltages extending further into the normal gap.

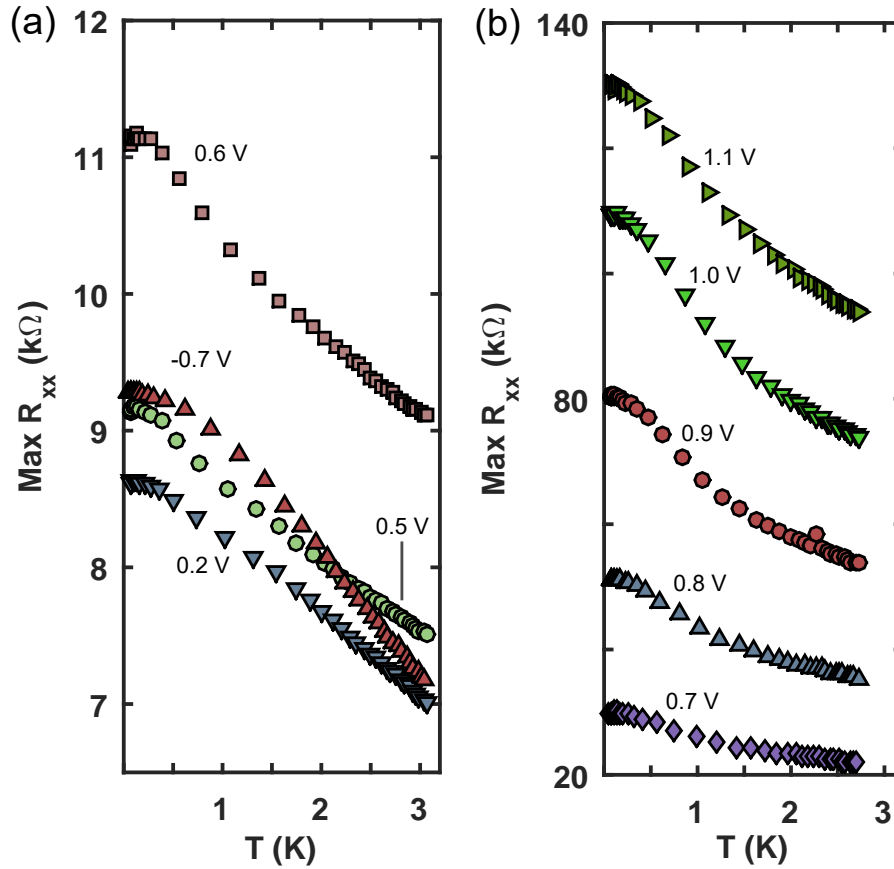


Figure 6.5: (a) Temperature dependence of the resistance maximum of the longitudinal resistance over front gate modulation at several fixed back gate voltages. (b) Temperature dependence of the resistance maximum of the longitudinal resistance over front gate modulation at several additional fixed back gate voltages.

The dependence of resistance on temperature for conduction measured in the hybridization gap observes a saturating character at low temperature. This behavior and the large positive magnetoresistance for conduction through the hybridization gap is in qual-

itative agreement with conduction in a disordered two-fluid (electron-hole) system[120]. The temperature dependence is not in agreement with the predictions that consider helical edge channels coupled to charge puddles modeled as quantum dots[117], where at temperatures lower than the average level spacing in charge puddles the rate of backscattering is expected to increase with increasing temperature. The temperature dependence of the resistance for conduction measured in the normal gap observes an activated behavior but also appears to saturate at low temperatures. The saturation in the normal gap regime may be due to anomalous edge channels[121], which may be due to residual conduction from charge accumulation at etched surfaces.

The origin of electron and hole charge fluctuations in an InAs/GaSb heterostructure may result from charged defects inducing potential fluctuations of sufficient strength that force the conduction band below and the valence band above the Fermi level randomly over space. A simple model was used to estimate the strength of the potential fluctuations in the heterostructure. In this model, depicted in the inset of Fig. 6.6, a layer of randomly distributed donor impurities are placed at the III-V/gate dielectric interface for the heterostructure, where l_g is the distance between the gate and bilayer, and l_d is the distance between the donor layer and the bilayer. For a donor layer of sheet charge density n_d , Tripathi and Kennett developed an analytical solution for the resulting potential fluctuations given the above model and accounting for screening by carriers in the two-dimensional system[122]:

$$e\sqrt{\langle\delta\phi^2\rangle} = \frac{\sqrt{n_d}e^2}{4\sqrt{\pi\epsilon}} \ln \left(1 + \left(\frac{R_c}{l_d} \right)^2 \right)^{1/2}, \quad (6.1)$$

where $R_c = \frac{\sqrt{n_d}}{\sqrt{\pi n_e}}$. The carrier density in the heterostructure was $\approx 4 \times 10^{11} \text{ cm}^{-2}$ at zero gate bias; therefore, n_d can be assumed at least this large, and studies of the well carrier density as a function of the top barrier thickness¹⁷ [27] and the gating efficiency¹⁸ [87]

suggest it is in the range of $10^{12} - 10^{13} \text{ cm}^{-2}$.

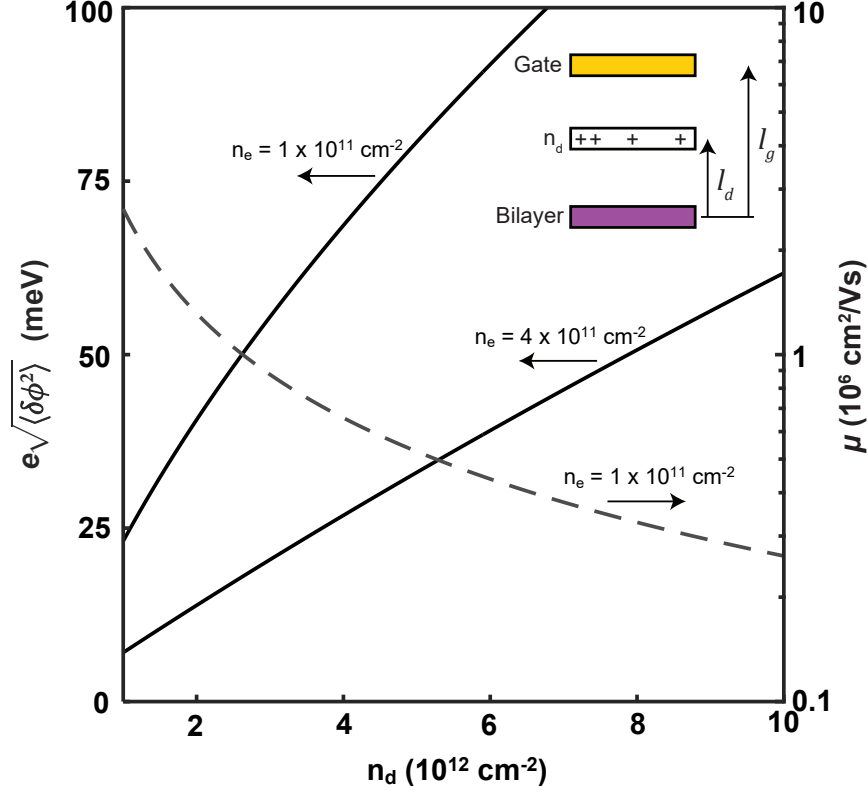


Figure 6.6: The calculated mean potential fluctuation for bilayer densities, $n_e = 1 \times 10^{11} \text{ cm}^{-2}$ and $n_e = 4 \times 10^{11} \text{ cm}^{-2}$, and the calculated mobility (dashed curve) for a bilayer density, $n_e = 1 \times 10^{11} \text{ cm}^{-2}$, as a function of a two-dimensional ionized donor layer for the gated heterostructure model shown in the inset.

The mean potential fluctuation as a function of n_d for two different carrier densities, n_e , calculated using Eq. 6.1 is depicted in Fig. 6.6. The dielectric constant, ϵ , was assumed to be $10\epsilon_0$. The mobility of electrons confined to InAs for the same model calculated following the treatment of Stern and Howard[85], as outlined in Appendix A, assuming a square well wavefunction[58] and a two-dimensional carrier density $n_e = 1 \times 10^{11} \text{ cm}^{-2}$ is also depicted in Fig. 6.6. The calculated mean potential fluctuation is substantially larger than the size of the hybridization gap measured in the heterostructure over the range of n_d . Furthermore, an estimate of the mobility for the above model would

be of the order 10^6 cm²/V·s. The measured mobility suggests the estimated potential fluctuations are a conservative estimate, and that other factors such as charge impurities in closer proximity to the bilayer and short range disorder such as interface roughness and alloy disorder should be considered. An estimate of the average spacing between charge fluctuations of approximately 200 nm was determined by the transition from negative longitudinal magnetoresistance to positive longitudinal magnetoresistance in region III.

In the InAs quantum wells presented in Ch. 4, the mobility in the 15 nm wide wells is believed to be limited by coulombic scattering mechanisms at densities in the range of the cross over density of the bilayer structure. The Landau level broadening can be estimated from measurements of the quantum lifetime. The lifetime at higher density, at approximately 8×10^{11} cm⁻² and under symmetric gating conditions have yielded lifetimes as high as 0.6 ps and correspond to a Landau level broadening of 1.1 meV. However, at a density in the range of the cross over density, at approximately 2×10^{11} cm⁻², and under symmetric gating conditions, yielded lifetimes lower than 0.1 ps, suggesting the broadening was greater than 6.5 meV. Thus, the level broadening in symmetrically biased InAs quantum wells grown under similar conditions and with the same barrier configuration as the InAs/GaSb bilayer corroborates the calculation indicating the scale of potential fluctuations are equal to or greater than the size of the hybridization gap.

The implication of this work is that even in a structure with state-of-the-art mobility the level of disorder is sufficiently high to suppress the topological phase[123] and lead to conduction through the bulk. Improvements in material quality are one path toward reducing potential fluctuations due to disorder. It is noted that in InAs quantum wells negative persistent photoconductivity and an associated enhancement in the quantum lifetime under illumination was observed by Lo and coworkers[124] and may be a technique to reduce charge disorder in InAs/GaSb heterostructures.

6.4 Conclusion

This work reported on the temperature and magnetic field dependence of the resistance of a dual-gated 11 nm InAs / 8 nm GaSb heterostructure gate-tuned through the inverted to normal gap regimes. The resistance maxima monotonically decreased with increasing temperature over the entire phase diagram. A large positive magnetoresistance was observed when the structure was gate-tuned to the inverted regime. Conduction in the predicted TI regime was qualitatively similar to behavior in a disordered two-dimensional system. Potential fluctuations were estimated to be sufficiently strong such that conduction in the predicted TI regime was likely dominated by a symplectic metal phase rather than a TI phase. The implications are that future efforts must address disorder in this system and focus must be placed on the reduction of defects and disorder in these heterostructures if a TI regime is to be achieved.

6.5 Acknowledgements

This work was supported by Microsoft Research Station Q. Chetan Nayak, Roman Lutchyn, Leonid Glazman, and Michael Freedman are thanked for valuable discussions. This work made use of the central facilities of the UCSB MRL, which is supported by the MRSEC program of the National Science Foundation under Award No. DMR-1121053. This work also made use of the UCSB Nanofabrication Facility, a part of the NSF funded NNIN network, and of the California NanoSystems Institute.

Chapter 7

Concluding Remarks and Outlook

7.1 A Summary of This Work

A comparative study of InAs/AlSb heterostructures wherein structure parameters were systematically varied led to a greater understanding of the limits to mobility in InAs quantum wells. Magnetotransport measurements using a dual-gated device geometry and a comparison of experiment to models of carrier mobility as a function of carrier density were used to identify dominant scattering mechanisms in these heterostructures. A novel variable substrate temperature growth procedure was developed and led to higher mobility at low carrier density in InAs quantum wells.

The development of dual-gated devices and high quality InAs channels with AlSb barriers led to a demonstration of the gate control of spin-orbit coupling in a high mobility InAs/AlSb quantum well in which the gate-tuned electron mobility exceeded $700,000 \text{ cm}^2/\text{V}\cdot\text{s}$. Analysis of low temperature magnetoresistance oscillations indicated the zero field spin-splitting could be tuned via the Rashba effect while keeping the two-dimensional electron gas charge density constant.

Findings from the work on InAs quantum wells were applied to investigations on

InAs/GaSb bilayers, a system predicted to be a two-dimensional topological insulator (TI). The temperature and magnetic field dependence of the resistance in dual-gated InAs/GaSb heterostructures gate-tuned to the predicted TI regime were found consistent with conduction through a disordered two-fluid system. The impact of disorder on the formation of topologically protected edge states and an insulating bulk was considered. Potential fluctuations in the band structure for realistic levels of disorder in state-of-the-art heterostructures were calculated using a gated heterostructure model. Potential fluctuations were estimated to be sufficiently large such that conduction in the predicted TI regime was likely dominated by tunneling between localized electron and hole charge fluctuations, corresponding to a symplectic metallic phase rather than a topological insulator. The implications are that future efforts must address defects and disorder in this system if the TI regime is to be achieved.

7.2 Future Work

The theoretical requirement on the mobility for forming topologically protected states of matter in 1-D InAs/superconductor heterostructures is satisfied by the highest quality materials presented in this thesis. Further improvements to mobility should still be pursued. The variable temperature substrate growth procedure presented in Ch. 2 requires additional investigation. Optimal V:III flux ratios and temperatures for barriers and the quantum well should be sought, and the concept of a variable temperature growth procedure can be extended to finding an optimal temperature for nucleating well/barrier interfaces and adjusting the substrate temperature to an optimal value for bulk growth after the seed layers are grown at interfaces.

Effort should be placed on improving source material quality, in particular the purity of antimony, which had higher specified impurity levels than aluminum, gallium, indium

and arsenic. In-house zone refining should be considered. Source material outgassing in dedicated outgassing chambers should also be considered; source material outgassing has recently been shown to yield significant improvements in the mobility of electrons confined to GaAs/AlGaAs heterostructures[125].

Enhancing mobility is a critical part of a conclusive observation of the predicted TI phase in InAs/GaSb heterostructures. Additional avenues to reduce potential fluctuations in the bilayer exist. For example, reducing the gate dielectric thickness will increase screening of charge at the III-V/dielectric interface by the gate metal. Furthermore, if the average separation of charge fluctuations could be increased to micron length scales, observation of the TI phase may be possible in mesoscopic devices. An additional motivation for enhancing mobility in heterostructures of InAs and AlSb is the yet-to-be-observed fractional quantum Hall effect in this material system, a hallmark of high material quality.

The InAs/GaSb bilayer structure offers a unique method for studying the heterointerface between the two materials. The dual-gated transport measurements can be used to measure the coupling strength of the two-dimensional states in the InAs and GaSb layers through the size of the hybridization gap, a parameter sensitive to the composition and the presence of defects at the heterointerface. The coupling strength can be compared for different interface growth procedures. This work would have implications for InAs/GaSb superlattices used for optoelectronic device applications.

Another possible method for controlling the subband structure of InAs/GaSb bilayers would be to alloy the electron and hole layers. For example, instead of using GaSb for the hole layer, one may use $\text{In}_x\text{Ga}_{1-x}\text{Sb}$. The band would be altered by both a change in the confinement potential, but also by the introduction of strain in the structure by deviating from lattice matching. A benefit of this path toward forming coupled two-dimensional electron-hole systems is that band alignments can be tuned in a way where

electron-hole subband inversion can take place for thinner epilayers, and therefore, the quantum mechanical coupling between subbands in the electron and hole layers can be increased; the coupling strength is inversely proportional to the physical separation of the electron and hole wavefunctions.

A final experimental approach to study defects in heterostructures of InAs, GaSb and AlSb is proposed: investigate the resistance fluctuations in mesoscopic devices fabricated on the heterostructures to determine capture and emission kinetics of defects and determine the effects of these defects on the low-frequency ($1/f$) noise in these devices. In mesoscopic devices (this proposal suggests the use of small area field effect device geometries) the alternate capture and emission of carriers at individual defects produce discrete switching events in the device resistance, resulting in the so called random telegraph signal (RTS) in current-voltage measurements over time. The experimental and theoretical framework for studying defects by studying noise in small area devices fabricated on Si/SiO₂ heterostructures[126, 127] can be used as a guide for studying defects by the same techniques in heterostructures of InAs, GaSb and AlSb. This investigation would yield important results concerning the utilization of the 6.1 Å family of materials in mesoscopic devices for quantum computation and identify fundamental characteristics of the defects in their heterostructures.

Appendix A

Calculating Mobility in InAs Quantum Wells

A.1 Section Title

The system considered was a two-dimensional electron gas confined to an InAs quantum well with $\text{Al}_x\text{Ga}_{1-x}\text{Sb}$ barriers. The electrons are mobile in the xy plane and are confined in the z-direction. The envelope wave function $\phi(z)$, over the InAs layer of thickness L was approximated by

$$\phi(z) = \left(\frac{2}{L}\right)^{1/2} \sin\left(\frac{\pi z}{L}\right), 0 \leq z \leq L \quad (\text{A.1})$$

and zero for all other z . The subband structure was neglected; only the lowest occupied subband was treated. The electron mobility $\mu = e\tau/m^*$, where e is the elementary charge, is a function of the momentum relaxation time, and the electron effective mass, m^* . An estimate of the effective mass accounting for band non-parabolicity[66] was used in the proceeding calculations.

Under the Born approximation the general form of the momentum relaxation time is given by[85]

$$\frac{1}{\tau_i} = \frac{1}{2\pi\epsilon_f} \int_0^{2k_f} dq \frac{q^2}{\sqrt{4k_f^2 - q^2}} \frac{\langle |U_i(q)|^2 \rangle}{\epsilon_q^2}, \quad (\text{A.2})$$

where the integration is over the wave number, q , and the subscript i labels the scattering mechanism under consideration. Within the random-phase approximation the dielectric matrix, ϵ_q , is given by

$$\epsilon_q = 1 + V(q)[1 - G(q)]X^0(q), \quad (\text{A.3})$$

where $G(q)$ is the Hubbard form of the local-field correction and $X^0(q)$ is the polarizability of the 2DEG. The electron-electron interaction $V(q)$ is characterized by a form factor and Coulomb potential due to the finite confinement and is expressed as

$$V(q) = \frac{q_s}{q} F_c(q), \quad (\text{A.4})$$

where $q_s = \frac{2\pi e^2}{\epsilon_L}$ is the screening parameter with dielectric constant, ϵ_L , and $F_c(q)$ is given by

$$F_c(q) = \int_{-\infty}^{+\infty} dz |\phi(z)|^2 \int_{-\infty}^{+\infty} dz' |\phi(z')|^2 \exp(-q|z - z'|). \quad (\text{A.5})$$

$\langle |U_i(q)|^2 \rangle$ is the averaged random potential corresponding to specific forms of defects leading to elastic scattering.

Rough quantum well interfaces in the presence of an electric field results in an averaged random potential, $\langle |U_{IR}(q)|^2 \rangle$, of the form[83]

$$\langle |U_{IR}(q)|^2 \rangle = \pi F^2 \Delta^2 \Lambda^2 \exp(-(q\Lambda)^2/4). \quad (\text{A.6})$$

Here, F is a function that includes terms for the variation in the quantum well width and a shift in the ground state energy in the presence of an electric field, E , from a perturbative treatment:

$$F = - \left(\frac{\hbar^2 \pi^2}{m^* L^3} + 96 \left(\frac{2}{3\pi} \right)^6 \frac{e^2 m^* L^3 E^2}{\hbar^2} \right). \quad (\text{A.7})$$

The quantum well width fluctuation due to interface roughness is parameterized by the height Δ and the in-plane correlation length Λ .

Un-intentional group-V (group-III) intermixing between the well and barriers during MBE growth can lead to the formation of $\text{InAs}_x\text{Sb}_{1-x}$ ($\text{In}_x\text{Al}_{1-x}\text{As}$) within the quantum well. The case of alloy scattering within the quantum well due to group-V intermixing was considered. Perfectly random alloy disorder results in a short range fluctuating potential, and the averaged random potential, $\langle |U_{\text{alloy}}(q)|^2 \rangle$, is expressed as[84]

$$\langle |U_{\text{alloy}}(q)|^2 \rangle = x(1-x)\delta V^2 \Omega \int dz \phi(z)^4. \quad (\text{A.8})$$

Here, δV is the spatial average of the fluctuating alloy potential, and $\Omega = \frac{\sqrt{3}\pi}{16} a^3$ is the volume of scattering potential in an alloy with lattice parameter, a . The spatial average of the fluctuating alloy potential, $\delta V = 0.8$ eV, was determined for the specific alloy composition from the heteropolar energy associated with the dielectric method of calculating the band structure[128].

Remote ionized impurities confined to a two-dimensional plane lead to a random potential, $\langle |U_{R,2D}(q)|^2 \rangle$, of the form[58]

$$\langle |U_{R,2D}(q)|^2 \rangle = \left(\frac{2\pi e^2}{\epsilon_L} \frac{1}{q} \right)^2 n_i(z) F(q, z_i)^2, \quad (\text{A.9})$$

where $n_i(z)$ is the impurity concentration. The form factor $F(q, z_i)$ accounts for the

finite width of the quantum well with the distance z_i between the impurity layer and the quantum well and is given by

$$F(q, z_i) = \int_{-\infty}^{+\infty} dz |\phi(z)|^2 \exp(-q|z - z_i|). \quad (\text{A.10})$$

The form of the average random potential, $\langle |U_{R,2D}(q)|^2 \rangle$, was extended for calculating the momentum relaxation time due to remote ionized impurities distributed in three dimensions by integration.

Homogeneous background impurities lead to a random potential[58]

$$\langle |U_B(q)|^2 \rangle = \left(\frac{2\pi e^2}{\epsilon_L} \frac{1}{q} \right)^2 N_B F_B(q), \quad (\text{A.11})$$

where N_B is the concentration of the three dimensional background ionized impurities in the InAs quantum well with the form factor

$$F_B(q) = \frac{1}{L} \int_{-\infty}^{+\infty} dz_i F(q, z_i)^2. \quad (\text{A.12})$$

The random potential, $\langle |U_{disl}(q)|^2 \rangle$, due to charged dislocations treated as a line charge[67] with charge density ρ_L along the dislocation line and areal density N_{disl} is given by

$$\langle |U_{disl}(q)|^2 \rangle = N_{disl} \left(\frac{e \rho_L}{\epsilon_L q} \right)^2 F_d(q), \quad (\text{A.13})$$

where the form factor is given by

$$F_d(q) = \int_{-\infty}^{+\infty} dz_i F(q, z_i)^2. \quad (\text{A.14})$$

The total momentum relaxation time was determined from the individual relaxation

times associated with each scattering mechanism by application of Mathiessens rule,

$$\frac{1}{\tau} = \frac{1}{\tau_{IR}} + \frac{1}{\tau_{alloy}} + \frac{1}{\tau_{R,2D}} + \frac{1}{\tau_{R,3D}} + \frac{1}{\tau_B} + \frac{1}{\tau_{disl}}. \quad (\text{A.15})$$

Appendix B

MBE Apparatus and Several In-situ Techniques

An overview of the MBE apparatus and several in-situ techniques is presented.

B.1 Overview of the III-V VG V80H

The III-V materials presented in this thesis were fabricated in a custom modified VG V80H MBE, and is shown in Fig. B.1. The MBE underwent 19 system openings which the author contributed too and, starting in his second year, led. Over the years a number of important modifications were made. The reader may find details of system openings in the VG V80H laboratory notebooks.

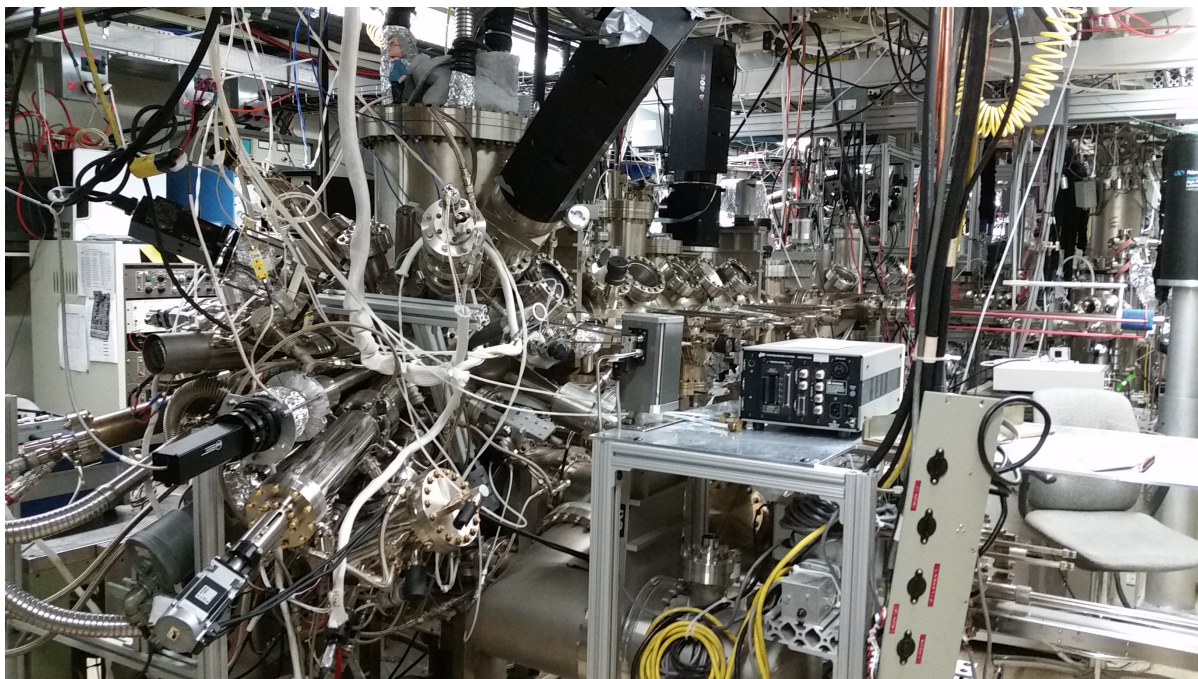


Figure B.1: A photograph of the III-V VGV80H MBE (center-left) circa May 2016.

The system, as of the summer of 2016, housed arsenic and antimony valved-cracker sources, aluminum, indium, gallium, silicon, beryllium, erbium, iron, gadolinium, and gallium telluride. An electron-gun source contained niobium, titanium, vanadium and NiTi. Pumping was provided by two cryopumps and two ion pumps. The VG V80H is a part of a large interconnected MBE and UHV characterization system discussed in a later section.

B.2 Installation of a 2” substrate manipulator

An important modification to the VG V80H MBE was the installation of a custom UHV Design substrate manipulator capable of handling 2” diameter wafers. The original substrate manipulator was limited to wafers of approximately $12 \times 17 \text{ mm}^2$ in size. A rear/side view of the substrate manipulator near the continuous azimuthal rotation

(CAR) is shown in Fig. B.2.



Figure B.2: Rear/Side view of the substrate manipulator near the continuous azimuthal rotation mechanism.

After the first several months of operation of the manipulator the wires, housed in ceramic beads on the rear side of the CAR, and providing a current path to the substrate heater, were disconnected from their barrel connectors. It was discovered that the original wires were silver plated copper. These wires, of course, reacted with arsenic in the MBE to form a brittle compound that fell apart at connections during operation. After this discovery, all silver coated copper wires with risk of exposure to arsenic were replaced with tantalum wires. The tantalum wires have yet to result in an open connection. They were an excellent improvement over the original design.

B.3 Finding small leaks

A critical step in realizing high mobility InAs quantum wells was, to the best of the author's ability, the elimination of leaks between UHV and atmosphere. The ability to find small leaks, where helium leak testing could be sensitive to a partial pressure of helium of 1×10^{-13} mbar, was enabled by an important repair of the MBE's residual

gas analyzer's (RGA) continuous dynode electron multiplier (CDEM). The RGA was originally installed on the growth chamber with a direct line of sight to the arsenic background pressure within the cryoshield. In this configuration, it was believed that metal coatings on the CDEM reacted with arsenic over time, rendering it inoperable. The CDEM was replaced and the RGA was moved to the preparation chamber. After the system opening in which this repair was performed, twelve previously undetected, small UHV leaks were discovered and repaired. The RGA with a properly working CDEM became an invaluable asset in discovering newly formed leaks or identifying contaminated substrates or sample blocks prior to loading into the growth chamber. A schematic of the RGA detector assembly and a new and damaged CDEM is shown in Fig. B.3.

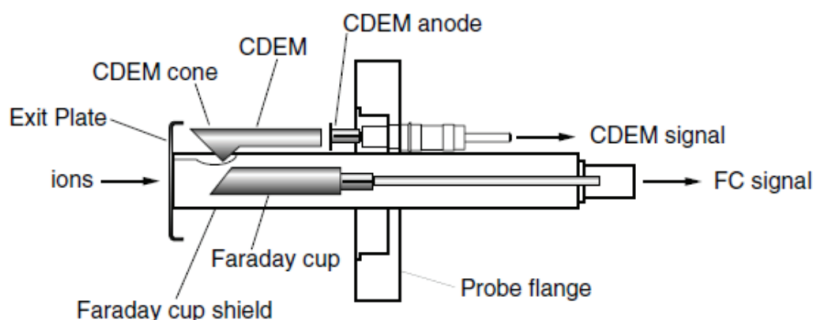


Figure B.3: Schematic of the Stanford Research Systems Model RGA200 residual gas analyzer's detector assembly (upper) and photograph (lower) of new (left) and damaged (right) continuous dynode electron multiplier.

B.4 Installation of the valved-cracker source for antimony

A Veeco 200V-Sb-L valved-cracker cell for antimony was installed in 2013. The cell yielded improved flux control, a lower cracker operating temperature, a larger capacity for source material, and greater reliability of operation over the original SVTA cell. Photographs of critical components of the cell during the initial assembly are shown in Fig. B.4.

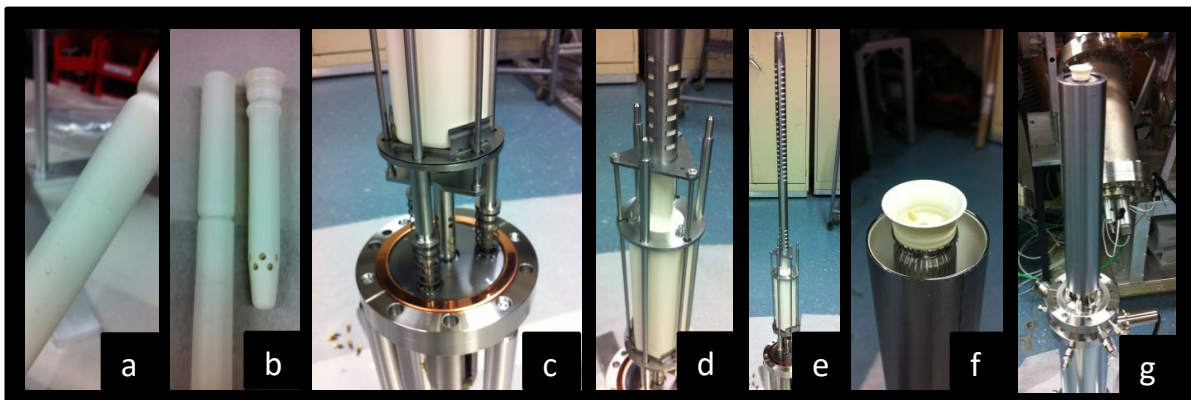


Figure B.4: Veeco 200V-Sb-L valved-cracker cell for antimony. (a) Conductance of pyrolytic boron nitride crucible. (b) End of conductance and needle valve. (c) Valve drive flange. (d) Trombone assembly. (e) Assembly prior to inserting into bulk and cracking zones. (f) Needle installed in trombone assembly. (g) Full assembly prior to outgassing.

The cell is, overall, of excellent design. One fault is pointed out. A tantalum tube used for heat shielding at the base of the cracking zone assembly and on the side of the cracker (see Fig. B.4(g)) was weakly spot welded to a tantalum frame. The shield can easily be perturbed from its position. A permanent solution for this issue was not developed because of limited access for making modifications without disassembling the cracking zone. Care should be taken while reloading source material, and the heat shielding tube should be checked each time the cell is reinstalled in the MBE.

B.5 A note on outgassing cells

It was found that cells using graphite crucibles, such as those provided by E-Science, benefit from outgassing at temperatures beyond the manufacturer's recommended outgassing temperatures. The procedure developed for high temperature outgassing is to operate the cell at the filament current limits for 8 hours. This outgassing step follows an initial slow and low temperature outgassing procedure to avoid high background partial pressures of atmospheric and water. Typical maximum outgassing temperatures will exceed 1600 °C on both base and tip thermocouples for dual-filament cells.

B.6 Integrated MBE and characterization facility

The VG V80H is a part of a large interconnected MBE and UHV characterization system shown in Fig. B.5. The instruments used to perform the work presented in this thesis include an atomic hydrogen source, an x-ray photoelectron spectrometer, and a low temperature STM.

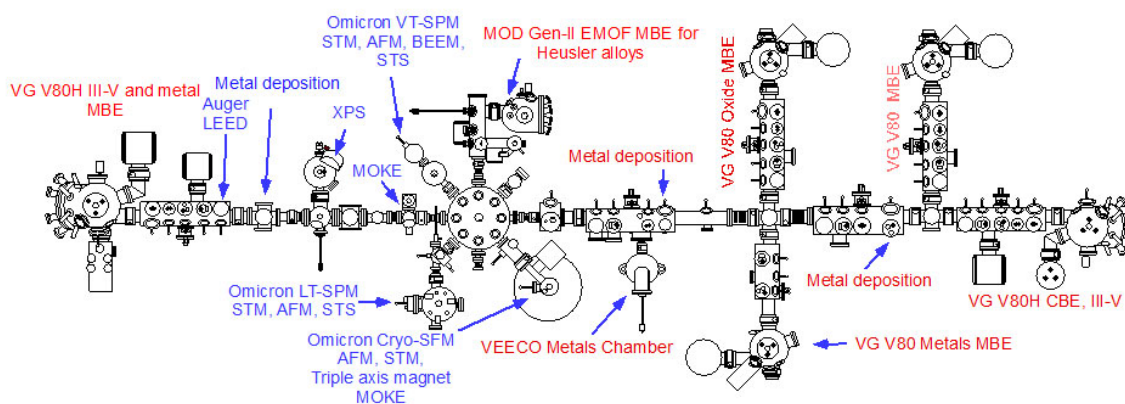


Figure B.5: A schematic of Chris's MBE and in-situ characterization facility circa 2016. Courtesy of Chris Palmstrøm.

Appendix C

Device Fabrication on InAs/AlSb/GaSb Heterostructures

Several of the microfabrication techniques used for fabricating the devices studied in this thesis are presented in this appendix.

C.1 Fabrication of dual-gated devices by optical lithography

An important technical accomplishment of this dissertation was the fabrication of dual-gated devices, wherein the conductive (001) GaSb:Te substrate could serve as one electrostatic gate while Ti/Au patterned with a lift-off mask could serve as a second electrostatic gate.

Fabrication begins with mesa definition. A key feature of the device geometry is its small size. It was found that larger devices had less reliable and lower yield operable back gates. Their primary short coming was high leakage currents at low back gate bias voltages. It was presumed that the larger area devices had a higher probability

of unintentionally shorting the back gate to the channel material through randomly distributed leakage paths, for example metallic oval defects. Therefore, devices were made small, with Hall bars having typical dimensions of $80 \times 20 \mu\text{m}^2$. The mesas for the devices presented in this thesis were defined by wet chemical etching with a solution of $\text{H}_3\text{PO}_4:\text{H}_2\text{O}_2:\text{C}_6\text{H}_8\text{O}_7:\text{H}_2\text{O} :: 3:5:55:220$.

Making electrical contact to the channel led to several avenues at which an unintentional short could occur. The first step to overcome a short between a metal lead and the substrate was to blanket coat the wafer with Al_2O_3 grown by atomic layer deposition (ALD) at 200°C using a water and trimethylaluminum based process. A five minute anneal at 200°C under hydrogen gas preceded the ALD process in the growth chamber. A Nomarski micrograph of a device after mesa definition and the blanket Al_2O_3 growth is shown in Fig. C.2(a).

Electrical contact was made to the channel by etching vias through the Al_2O_3 with a buffered oxide etch and stopping in the $\text{Al}(\text{Ga})\text{Sb}$ top barrier, as shown in Fig. C.2(b). After the oxide etch, an etch in a basic solution was used to remove the AlSb and GaSb and stop at the InAs. Fig. C.2(c) shows a device after this step using AZ 300 MIF as the etchant.

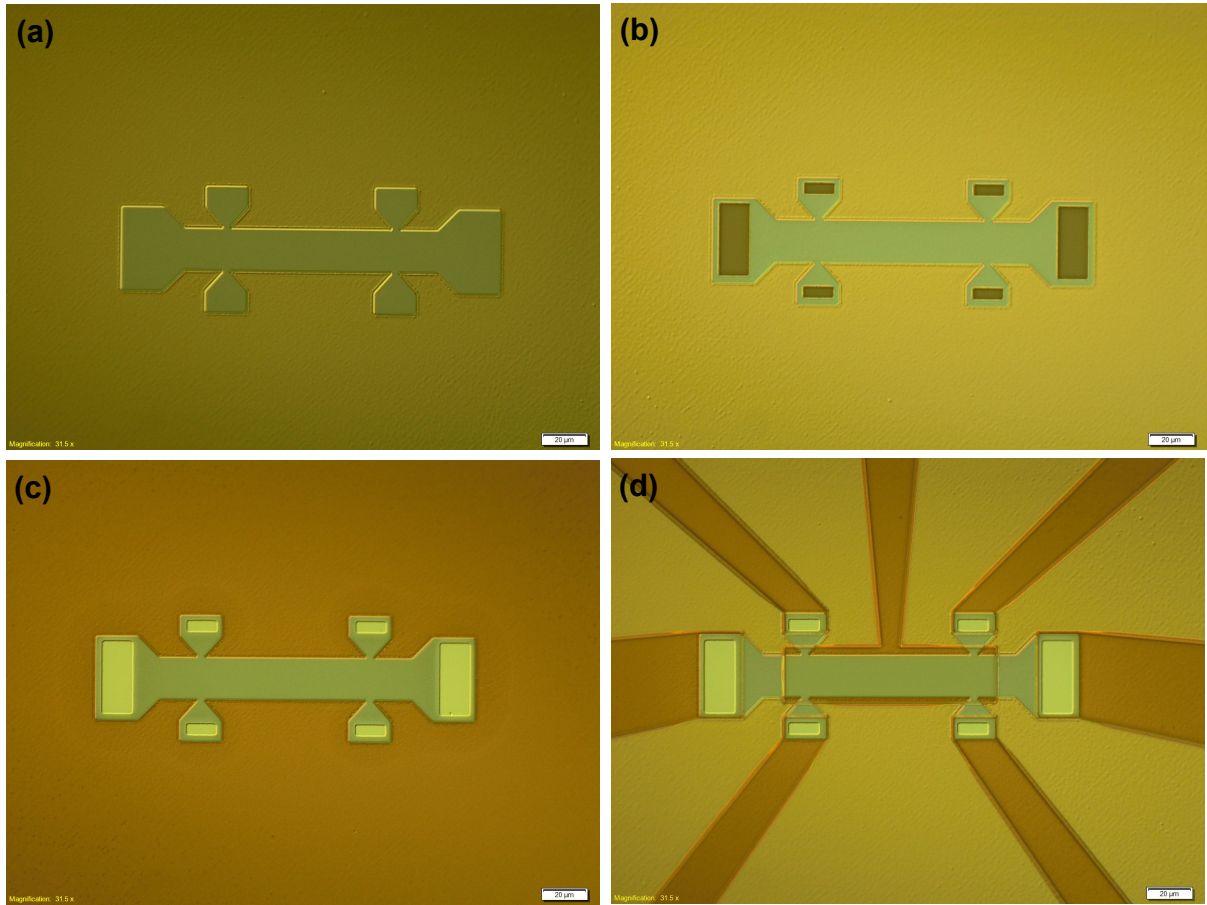


Figure C.1: (a) Mesa etched and blanket Al_2O_3 grown over an InAs-GaSb-AlSb heterostructure grown on a GaSb:Te substrate. (b) BHF etch through the Al_2O_3 and stopped at the AlSb top barrier. (c) 300 MIF etch through AlSb and GaSb layers, etch stop at InAs layer. (d) Ohmic and gate metallization lift-off resist prior to metal evaporation and lift-off.

Ohmic and gate metallization were performed simultaneously with a single lift-off process. The developed resist is shown in Fig. C.2(d). The blanket Al_2O_3 prevents the metal leads from shorting to the substrate through randomly distributed leakage paths on the etched surface.

To improve yield, multiple Hall bars could be patterned on a single chip, and each could be examined under a Nomarski microscope to select the best bar for moving forward with the fabrication process. Note that the device shown in Fig. C.2 has vias that are

smaller than the mesa dimensions. This is acceptable for low field measurements and studying transport in InAs/GaSb bilayers. However, to probe the integer quantum Hall regime in these materials, the vias need to overlap with the mesa edges so that the metal leads can make contact to edge states and not be isolated by an insulating bulk.

All cleaning procedures before device processing and during device processing use only the solvents acetone, isopropyl alcohol and methanol. Common resist strippers are avoided because they typically use bases, such as tetramethylammonium hydroxide, that etch the antimonides. An SEM micrograph of a mesa defined over an InAs/GaSb bilayer heterostructure and after the photoresist was removed using solvents is shown in Fig. C.2(a)-(c).

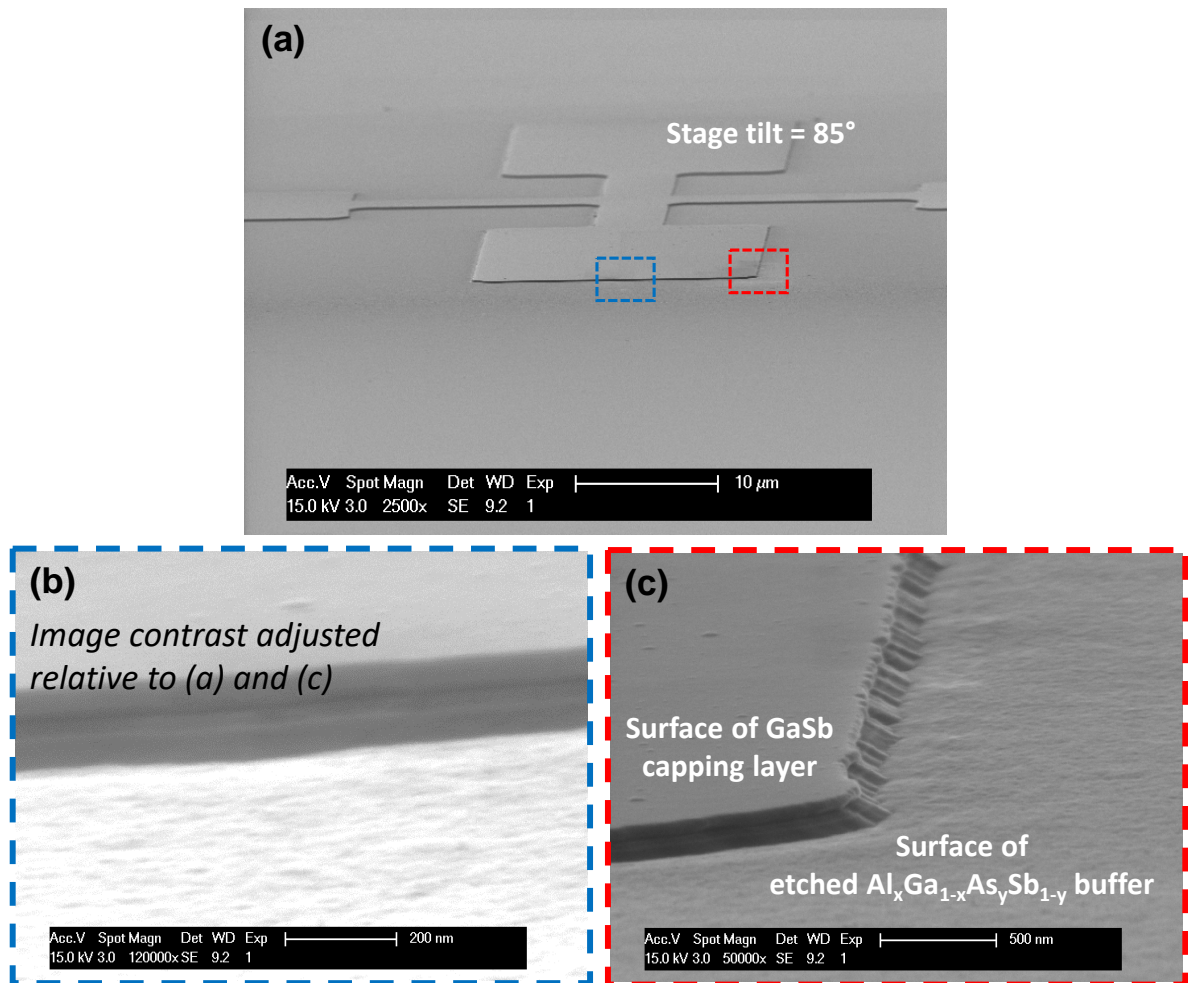


Figure C.2: (a) SEM micrograph of mesa etch over an InAs-GaSb-AlSb heterostructure. (b) Magnified SEM micrograph of the region in (a) encompassed by the blue (left) box. (c) Magnified SEM micrograph of the region in (a) encompassed by the red (right) box.

Do not move quickly when AlSb is exposed to air until it is in some way passivated. As a final note, pay attention to every detail at every step of your fabrication process. The antimonides will work against you if you give them the opportunity.

Appendix D

Cryogenic Measurements

The design of the cryogenic measurement equipment used for acquiring the majority of the transport data in this thesis is presented.

D.1 A custom probe for a Quantum Design PPMS

Studies of the current-voltage characteristics in materials often require device fabrication that incorporates features susceptible to damage from electrostatic discharge (ESD). Examples include insulated gate, point contact and tunneling magnetoresistance devices[129, 130]. A common characteristic of device components sensitive to ESD is a highly resistive channel with no parallel resistive or junction-like path that can discharge static electricity as it is building up[131]. to Motivation for developing a probe that would prevent ESD arose after experiencing ESD induced damage to insulated gate and point contact devices during sample puck installation in a Quantum Design PPMS. In this section the construction of a probe that prevents ESD during sample installation and the measurement of ESD sensitive devices are presented.

Fig. D.1 shows the probe with critical elements labeled. The design incorporated

features to allow an installed device to maintain a single electrical ground during installation and measurements in the PPMS sample chamber. The probe avoids using the PPMS sample chamber wiring by routing the sample wiring through the electrical feedthrough assembly. The electrical feedthrough assembly includes a 25 pin D-sub vacuum feedthrough. On the vacuum side, 16 leads are provided by 8 twisted pair manganin cryogenic wires running from the D-sub connector through the stainless steel tube and connecting to two filter boards that hold a 16 pin DIP chip carrier on which a sample can be mounted. This wiring design allows the device to be connected to measurement electronics and an analog ground while the probe is outside of the PPMS sample chamber. The path to the electronics and analog ground is not broken during probe installation into the PPMS sample chamber.

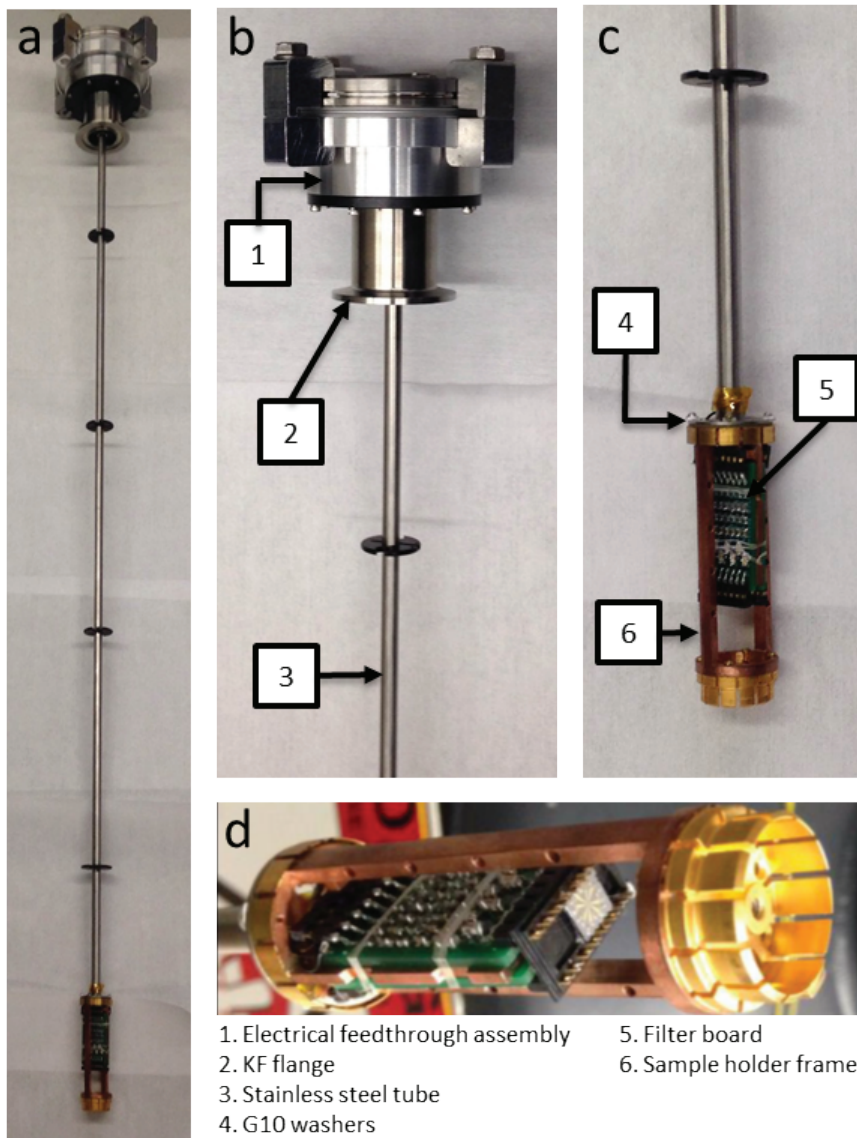


Figure D.1: A custom probe for a Quantum Design PPMS.

Furthermore, the probe and sample ground may be isolated from the chamber ground. The chamber is electrically connected to the KF flange and the sample holder frame. However, the KF flange is isolated from the probe by rubber seals and the sample holder frame is isolated from the probe by G10 washers. Therefore, the electrical feedthrough assembly, stainless steel tube and filter boards can be connected to a ground isolated from

the chamber ground. Using an isolated ground allows shielding of the sample wiring from capacitive coupling to the chamber ground.

Fig. D.2 shows a schematic of the filters incorporated into each of the 16 leads. The filtering is not necessary for protection against ESD, but was incorporated to reduce high frequency noise at the sample.

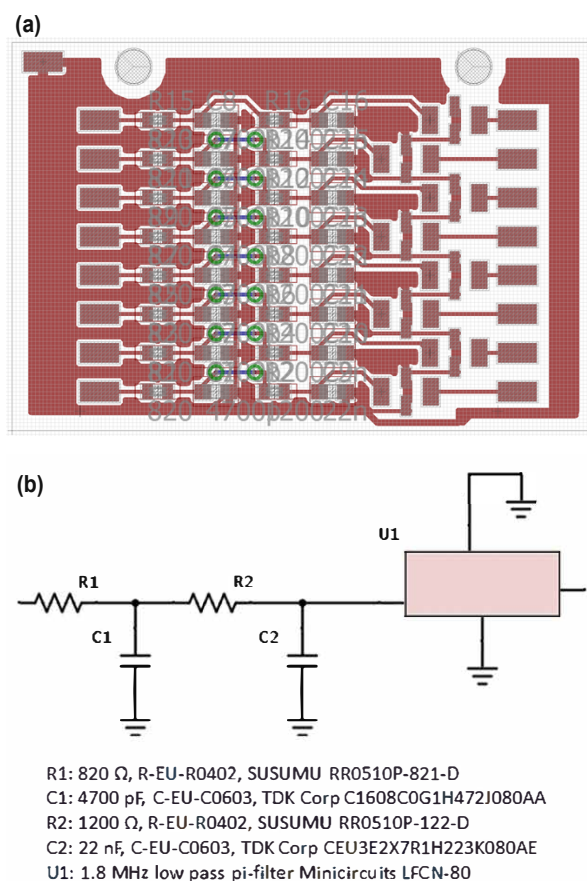


Figure D.2: (a) A schematic of the filter board designed using the EAGLE PCB Design software package. (b) Circuit diagram and component list of the low pass filter implemented on the filter board.

The temperature at the sample was calibrated using a LakeShore model CX-1050-SD Cernox temperature sensor. With helium exchange gas in the sample space the temperature measured by the Cernox temperature sensor to match the PPMS sample thermometer temperature over the range 2 Kelvin to 300 Kelvin. A small amount of

hysteresis is observed during temperature cycling with a heating or cooling rate of 3 degrees Kelvin per minute. Without helium exchange gas in the sample space the temperature measured by the Cernox temperature sensor at the sample could not reach the base temperature of the PPMS. A modification to the probe design that would increase thermal conduction between the probe and wiring with the cooling annulus should allow for operation down to 2 Kelvin under high vacuum conditions. The measurements discussed in the remainder of this application note were taken with helium exchange gas in the sample space.

The probe was successfully used to measure ESD-sensitive insulating gate and point contact devices. Fig. D.3 shows the conductance as a function of gate voltage of a quantum point contact (QPC) fabricated over a GaAs/AlGaAs heterostructure hosting a two-dimensional electron gas (2DEG) measured on our probe using a 4-point configuration. Depletion of the 2DEG beneath the split gates occurs at approximately -0.2 V. The conductance through the QPC approaches zero at approximately -1.22 V. Similar devices have suffered from failure by ESD during sample insertion into the PPMS sample space using standard PPMS pucks.

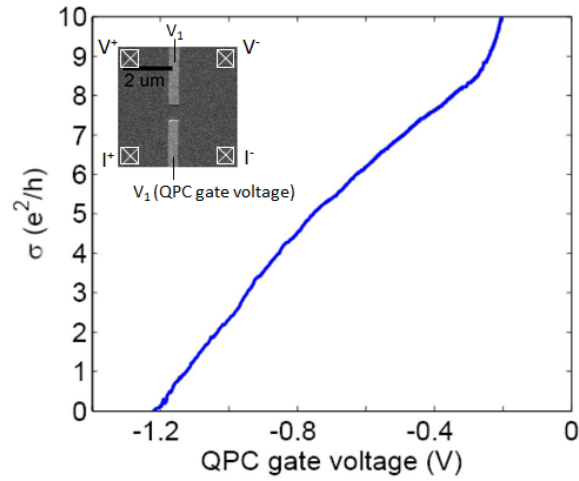


Figure D.3: Conductance as a function of split-gate gate voltage for the device depicted in the inset. The QPC was fabricated over a GaAs/AlGaAs heterostructure set back 110 nm from the structure's surface.

D.2 Adiabatic demagnetization refrigeration for mK measurements

An HPD Model 103 ADR was configured for magnetotransport measurements at sample temperatures as low as 50 mK. The system was configured with DC measurement wiring at the 60 Kelvin, 3 Kelvin, 500 mK and 50 mK stages. Filters were incorporated at the 60 K and 3 K stages. A 16 pin DIP chip carrier sample holder was designed and installed at the 50 mK stage. Magnetic fields up to 5 T could be applied at the sample using a 5T American Magnetics superconducting magnet. The system configured as described is shown in Fig. D.4.

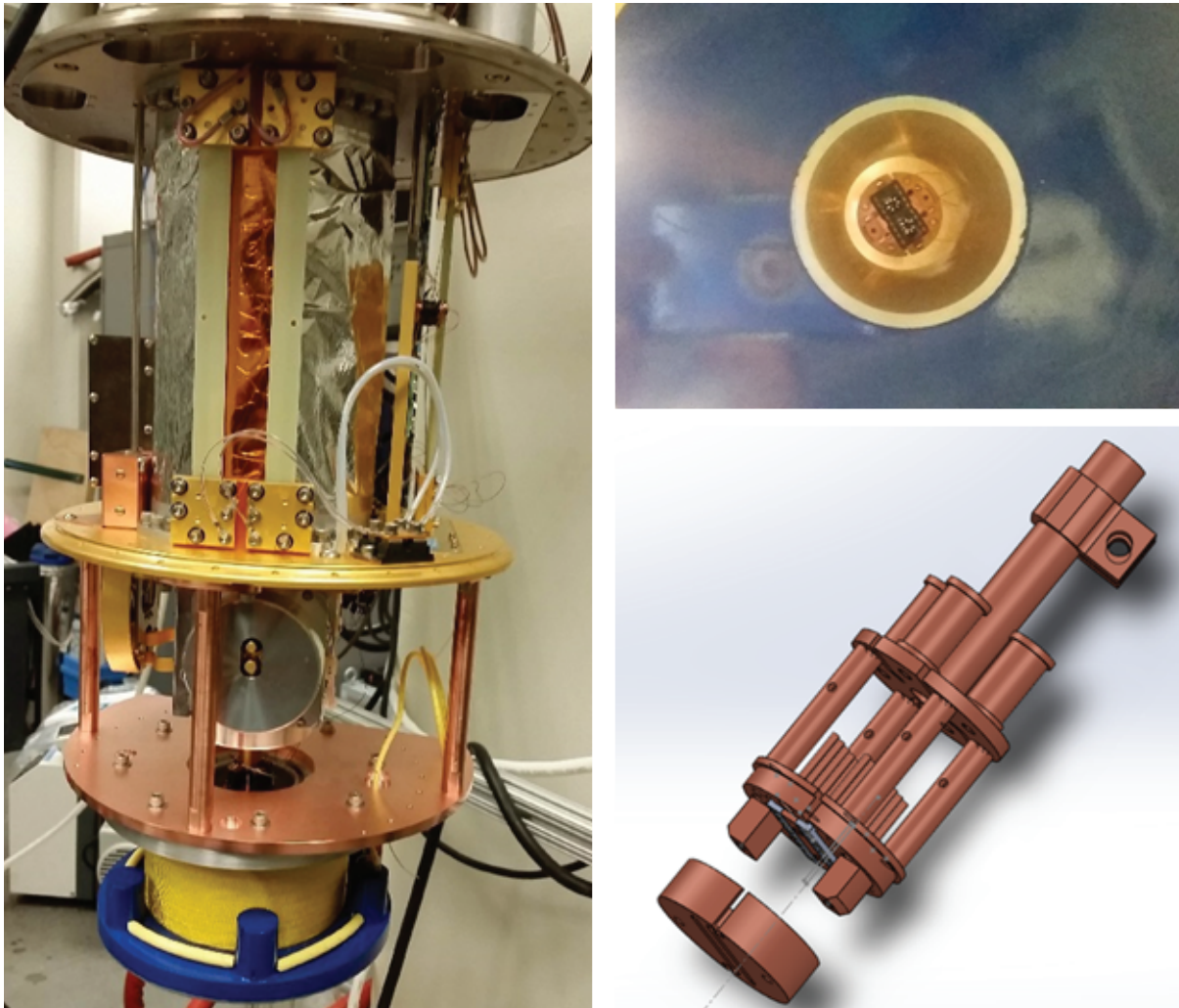


Figure D.4: Adiabatic demagnetization refrigerator with 5 T superconducting sample magnet and custom chip carrier mount and wiring.

The reader should refer to the HPD manuals and the ADR laboratory notebook for operating instructions.

Appendix E

Analysis of Shubnikov de Haas oscillations.

A MATLAB code for taking a Fourier analysis of magnetoresistance oscillations is presented.

E.1 Fourier analysis of Shubnikov de Haas oscillations

```
function [SdH_fft_result] = SdH_fft_function(field,rhoxx,min_field,...
max_field,sampling_frequency)

field_idx = find(field > min_field & field < max_field);

temp_field = field(field_idx);
temp_rhoxx = rhoxx(field_idx);
```

```
oneover_field = smooth(1./temp_field);

oneover_field_range = max(oneover_field) - min(oneover_field);

oneover_field_forinterp = [0:(sampling_frequency)]/...
sampling_frequency*oneover_field_range+min(oneover_field);

oneover_rhoxx_forfft = interp1(oneover_field,temp_rhoxx,...
oneover_field_forinterp);

field_range = sampling_frequency/oneover_field_range;

field_forfft=zeros(sampling_frequency+1,1);

for i = 1:sampling_frequency+1
    field_forfft(i) = field_range*(i-1)/(sampling_frequency);
end

SdH_fft_result.field = field_forfft;
SdH_fft_result.rhoxx_fft = abs(fft(oneover_rhoxx_forfft));
SdH_fft_result.unnormalized_rhoxx_fft = SdH_fft_result.rhoxx_fft;
SdH_fft_result.rhoxx_fft = SdH_fft_result.rhoxx_fft/...
max(SdH_fft_result.rhoxx_fft(80:4000));
```

Appendix F

Growth of GaAs/AlGaAs

Two-dimensional Electron Systems

for Quantum Computing

Applications

The growth and transport properties of GaAs/AlGaAs heterostructures in close proximity to the structure surface are presented.

F.1 The growth and transport properties of

GaAs/AlGaAs heterostructures for spin qubits

Two-dimensional electron gases (2DEGs) confined to GaAs/AlGaAs heterostructures were fabricated for their application in developing spin qubits using gate-defined quantum dots. The heterostructure requirements were their set back from the structure's surface

had to be 100 nm or less and that their density had to be in the range of $1-3 \times 10^{11} \text{ cm}^{-2}$ at zero gate bias, both conditions being stipulated so depletion under gates could be achieved at reasonable voltages. The development of low density 60 nm set back 2DEGs resulted from feedback from low temperature magnetotransport measurements on MBE grown GaAs/AlGaAs heterostructures with small perturbations to the heterostructure design guided by a self-consistently calculated band profile. Silicon modulation doping was refined by growing structures with identical layer dimensions while varying MBE growth conditions and making small changes to doping concentrations. In addition to the development of optimum heterostructures and growth conditions, technological improvements to the MBE system were made to yield higher quality materials. The two most significant material quality gains resulted from the following: (1) Improving the ability to detect growth chamber leaks by installing a residual gas analyzer in the preparation rather than the growth chamber. The continuous dynode electron multiplier on Stanford Research Systems RGA was found to be corrupted by arsenic contamination which reduced the ability to detect small leaks between UHV and atmosphere, as discussed in Appendix B. (2) Higher temperature and longer duration outgassing of an E-science Titan cell with a pyrolytic graphite crucible used for the gallium source. The graphite crucible was believed to adsorb more atmospherics than traditional PBN crucibles when the crucible was exposed to air.

Fig. F.1 shows the voltage measured over a GaAs/Al_{0.66}Ga_{0.34}As heterostructure at a sample temperature of 1.8 K, using an AC excitation current of 500 nA, and using the Van der Pauw (VdP) geometry, the VdP square measuring approximately $5 \times 5 \text{ mm}^2$, with InSn contacts. The modulation doping set back from the 2DEG was 25 nm. The Hall mobility was approximately $960,000 \text{ cm}^2/\text{V}\cdot\text{s}$.

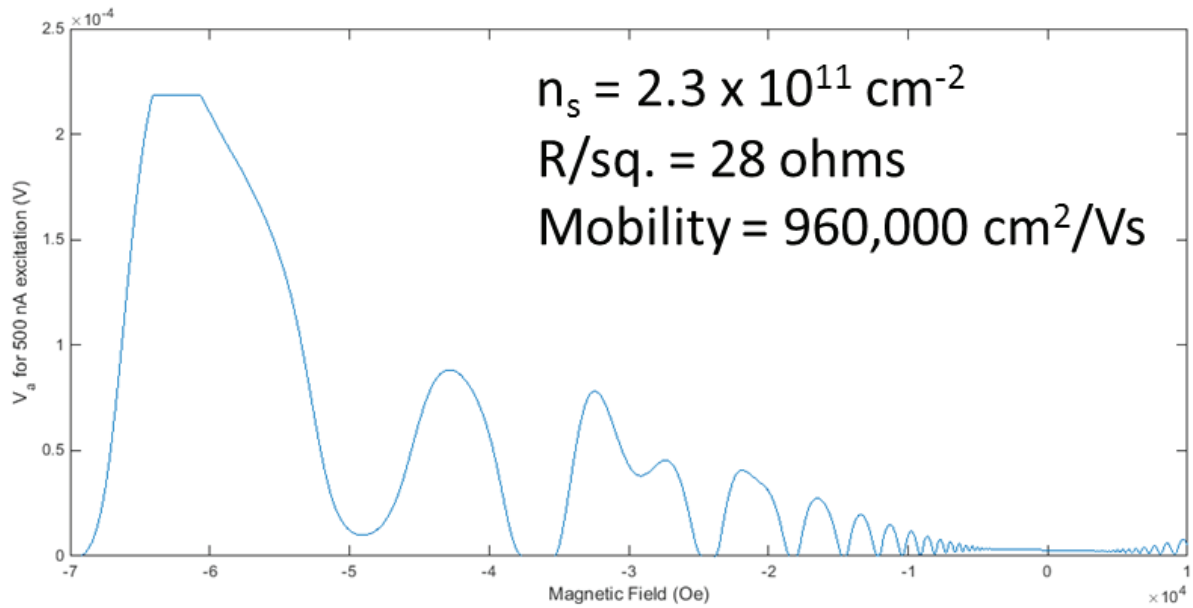


Figure F.1: Voltage measured over a GaAs/Al_{0.66}Ga_{0.34}As heterostructure at a sample temperature of 1.8 K, using an AC excitation current of 500 nA, and using the VdP geometry, the VdP square measuring approximately 5×5 mm², with InSn contacts.

This work was funded by IARPA under the Multi-Qubit Coherent Operation Project. For additional details, refer to the author’s laboratory notebooks and monthly IARPA reports.

Appendix G

Material Parameters for Band Structure Calculations

Several of the material parameters used in the one-dimensional Schrodinger-Poisson band-structure calculations presented in this thesis are listed.

G.1 Band parameters

The parameters listed below were taken from Vurgaftman et al.[15] and the references therein. The valence band offset (VBO) is relative to the valence band of InSb.

<u>InAs</u>	
E_g^Γ (eV)	0.417
m_e^*	0.026
VBO (eV)	-0.59
ϵ	14.5

<u>GaAs</u>	
E_g^Γ (eV)	1.519
m_e^*	0.067
VBO (eV)	-0.8
ϵ	13.1

<u>AlAs</u>	
E_g^Γ (eV)	3.099
E_g^X (eV)	2.24
m_e^*	0.15
VBO (eV)	-1.33
ϵ	10.1

<u>GaSb</u>	
E_g^Γ (eV)	0.812
m_e^*	0.039
VBO (eV)	-0.03
ϵ	15.7

<u>AlSb</u>	
E_g^Γ (eV)	2.386
E_g^X (eV)	1.696
m_e^*	0.14
VBO (eV)	-0.41
ϵ	11.0

Bibliography

- [1] D. Bouwmeester, A. Ekert, and A. Zeilinger, *The Physics of Quantum Information*. Springer-Verlag, Berlin, 2000.
- [2] P. Shor, *Polynomial-time algorithms for prime factorization and discrete logarithms on a quantum computer*, *SIAM Journal of Computing* **26** (1997) 1484–1509.
- [3] R. P. Feynman, *Simulating physics with computers*, *International Journal of Theoretical Physics* **21** (1982) 467–488.
- [4] P. W. Shor, *Scheme for reducing decoherence in quantum computer memory*, *Physical Review A* **52** (1995), no. 4 2493–2496, [0506097].
- [5] A. Y. Kitaev, *Fault-tolerant quantum computation by anyons*, *Annals of Physics* **303** (2003), no. 1 2–30, [9707021].
- [6] M. H. Freedman, A. Kitaev, M. J. Larsen, and Z. Wang, *Topological quantum computation*, *Bulletin of the American Mathematical Society* **40** (2002), no. 1 31–38.
- [7] S. Das Sarma, M. Freedman, and C. Nayak, *Topologically protected qubits from a possible non-abelian fractional quantum hall state*, *Phys. Rev. Lett.* **94** (Apr, 2005) 166802.
- [8] R. M. Lutchyn, J. D. Sau, and S. Das Sarma, *Majorana Fermions and a Topological Phase Transition in Semiconductor-Superconductor Heterostructures*, *Physical Review Letters* **105** (aug, 2010) 077001.
- [9] S. Mi, D. I. Pikulin, M. Wimmer, and C. W. J. Beenakker, *Proposal for the detection and braiding of Majorana fermions in a quantum spin Hall insulator*, *Physical Review B - Condensed Matter and Materials Physics* **87** (2013), no. 24 1–5, [arXiv:1304.1685].
- [10] H. Kroemer, *Nobel Lecture-Quasi-electric Fields and Band Offset: Teaching Electrons New Tricks*, *Reviews of Modern Physics* **73** (2000), no. July 449–469, [0903.4403].

- [11] A. C. Gossard, *Growth of Microstructures by Molecular Beam Epitaxy*, *IEEE Journal of Quantum Electronics* **22** (1986), no. 9 1649–1655.
- [12] O. Kubaschewski and C. Alcock, *Metallurgical Thermochemistry*. Pergamon Press, Oxford, 1979.
- [13] J. Y. Tsao, *Materials Fundamentals of Molecular Beam Epitaxy*. Academic Press, San Diego, 1993.
- [14] I. V. Markov, *Crystal Growth for Beginners*. World Scientific Publishing Co., Toh Tuck Link, Singapore, 2003.
- [15] I. Vurgaftman, J. R. Meyer, and L. R. Ram-Mohan, *Band parameters for III-V compound semiconductors and their alloys*, *Journal of Applied Physics* **89** (2001), no. 11 5815–5875.
- [16] J. H. Davies, *The Physics of Low-Dimensional Semiconductors*. Cambridge University Press, Cambridge, 1998.
- [17] I. H. Tan, G. L. Snider, L. D. Chang, and E. L. Hu, *A self-consistent solution of Schrodinger-Poisson equations using a nonuniform mesh*, *Journal of Applied Physics* **68** (1990), no. 8 4071–4076.
- [18] C. Liu, T. L. Hughes, X. L. Qi, K. Wang, and S. C. Zhang, *Quantum spin hall effect in inverted type-II semiconductors*, *Physical Review Letters* **100** (2008), no. 23 236601.
- [19] B. Shojaei, A. Mcfadden, J. Shabani, B. D. Schultz, and C. J. Palmstrøm, *Studies of scattering mechanisms in gate tunable InAs / (Al , Ga) Sb two dimensional electron gases*, *Appl. Phys. Lett* **106** (2015) 222101.
- [20] B. Shojaei, P. J. J. O’Malley, J. Shabani, P. Roushan, B. D. Schultz, R. M. Lutchyn, C. Nayak, J. M. Martinis, and C. J. Palmstrøm, *Demonstration of gate control of spin splitting in a high-mobility InAs/AlSb two-dimensional electron gas*, *Physical Review B* **93** (2016), no. 7 075302.
- [21] H. Sakaki, L. L. Chang, R. Ludeke, C. A. Chang, G. A. Sai-Halasz, and L. Esaki, *In_{1-x}Ga_xAs-GaSb_{1-y}As_y heterojunctions by molecular beam epitaxy*, *Applied Physics Letters* **31** (1977), no. 3 211–213.
- [22] W. R. Frensley and H. Kroemer, *Theory of the energy-band lineup at an abrupt semiconductor heterojunction*, *Physical Review B* **16** (1977), no. 6 2642–2652.
- [23] W. A. Harrison, *Elementary theory of heterojunctions*, *Journal of Vacuum Science and Technology* **14** (1977), no. 4 1016–1021.

- [24] A. Nakagawa, H. Kroemer, and J. H. English, *Electrical properties and band offsets of InAs/AlSb n-N isotype heterojunctions grown on GaAs*, *Applied Physics Letters* **54** (1989), no. 19 1893–1895.
- [25] C. Nguyen, B. Brar, C. R. Bolognesi, J. J. Pekarik, and H. Kroemer, *Growth of InAs-AISb Quantum Wells Having Both High Mobilities and High Concentrations*, *Journal of Electronic Materials* **22** (1993), no. 2 2–5.
- [26] M. Thomas, H. Blank, and K. C. Wong, *Buffer-dependent mobility and morphology of InAs / (Al , Ga) Sb quantum wells*, *Journal of Crystal Growth* **176** (1997) 894–897.
- [27] C. Nguyen, B. Brar, H. Kroemer, and J. H. English, *Surface donor contribution to electron sheet concentrations in not-intentionally doped InAs-AISb quantum wells*, *Applied Physics Letters* **60** (1992), no. 15 1854–1856.
- [28] S. Subbanna, G. Tuttle, and H. Kroemer, *N- type doping of gallium antimonide and aluminum antimonide grown by molecular beam epitaxy using lead telluride as a tellurium dopant source*, *Journal of Electronic Materials* **17** (1988), no. 4 297–303.
- [29] G. Tuttle, H. Kroemer, and J. H. English, *Effects of interface layer sequencing on the transport properties of InAs/AlSb quantum wells: Evidence for antisite donors at the InAs/AlSb interface*, *Journal of Applied Physics* **67** (1990), no. 6 3032–3037.
- [30] C. R. Bolognesi, H. Kroemer, and J. H. English, *Interface roughness scattering in InAs/AlSb quantum wells*, *Applied Physics Letters* **61** (1992), no. 2 213.
- [31] M. Altarelli, *Electronic structure and semiconductor-semimetal transition in InAs-GaSb superlattices*, *Physical Review B* **28** (1983), no. 2 842–845.
- [32] Y. Naveh and B. Laikhtman, *Band-structure tailoring by electric field in a weakly coupled electron-hole system*, *Applied Physics Letters* **66** (1995), no. 15 1980.
- [33] Y. Naveh and B. Laikhtman, *Excitonic instability and electric-field-induced phase transition towards a two dimensional exciton condensate*, *Physical Review Letters* **77** (1996), no. 5 900–903, [9605166].
- [34] J. Quinn and J. Quinn, *Semimetal-semiconductor transition in InAs-GaSb heterostructures*, *Surface Science* **361/362** (1996) 930–932.
- [35] M. J. Yang, C. H. Yang, B. R. Bennett, and B. V. Shanabrook, *Evidence of a Hybridization Gap in Semimetallic " InAs GaSb Systems*, *Phys. Rev. Lett.* **78** (1997), no. 24 4613–4616.

- [36] H. Kroemer, *The family (InAs, GaSb, AlSb) and its heterostructures: a selective review*, *Physica E: Low-dimensional Systems and Nanostructures* **20** (jan, 2004) 196–203.
- [37] B. R. Bennett, R. Magno, J. B. Boos, W. Kruppa, and M. G. Ancona, *Antimonide-based compound semiconductors for electronic devices: A review*, *Solid-State Electronics* **49** (2005), no. 12 1875–1895.
- [38] S. Huang, G. Balakrishnan, and D. L. Huffaker, *Interfacial misfit array formation for GaSb growth on GaAs*, *Journal of Applied Physics* **105** (2009), no. 10 1–6.
- [39] B. Brar and D. Leonard, *Spiral growth of GaSb on (001) GaAs using molecular beam epitaxy*, *Applied Physics Letters* **463** (1995), no. 001 463.
- [40] Y. Wang, P. Ruterana, L. Desplanque, S. El Kazzi, and X. Wallart, *Strain relief at the GaSb/GaAs interface versus substrate surface treatment and AlSb interlayers thickness*, *Journal of Applied Physics* **109** (2011), no. 2 023509.
- [41] W. Qian, M. Skowronski, R. Kaspi, M. DeGraef, and V. P. Dravid, *Nucleation of misfit and threading dislocations during epitaxial growth of GaSb on GaAs(001) substrates*, *Journal of Applied Physics* **81** (1997), no. 11 7268–7272.
- [42] S. H. Huang, G. Balakrishnan, a. Khoshakhlagh, a. Jallipalli, L. R. Dawson, and D. L. Huffaker, *Strain relief by periodic misfit arrays for low defect density GaSb on GaAs*, *Applied Physics Letters* **88** (2006), no. 13 131911.
- [43] H. Blank, S. Mathis, E. Hall, S. Bhargava, A. Behres, M. Heuken, H. Kroemer, and V. Narayanamurti, *Al (As , Sb) heterobarriers on InAs : growth , structural properties and electrical transport*, *Journal of Crystal Growth* **187** (1998) 18–28.
- [44] B. R. Bennett, B. V. Shanabrook, and M. E. Twigg, *Anion control in molecular beam epitaxy of mixed As/Sb III-V heterostructures*, *Journal of Applied Physics* **85** (1999), no. 4 2157–2161.
- [45] E. Luna, I. Guzmán, A. Trampert, and G. Ivarez, *Critical role of two-dimensional island-mediated growth on the formation of semiconductor heterointerfaces*, *Physical Review Letters* **109** (2012), no. 12 1–5, [1206.6983].
- [46] M. Z. Hasan and C. L. Kane, *Colloquium : Topological insulators*, *Reviews of Modern Physics* **82** (2010), no. 4 3045–3067.
- [47] A. H. Kramer *Proc. Amsterdam Acad.* **33** (1930) 959.
- [48] G. Dresselhaus, *Spin-Orbit Coupling Effects in Zinc Blende Structures*, *Physical Review* **100** (1955), no. 2 580–586.

- [49] Y. A. Bychkov and E. I. Rashba, *Oscillatory effects and the magnetic susceptibility of carriers in inversion layers*, *J. Phys. C: Solid State Phys.* **17** (1984) 6039–6045.
- [50] G. Lommer, F. Malcher, and U. Rossler, *Spin splitting in semiconductor heterostructures for $B \rightarrow 0$* , *Phys. Rev. Lett.* **60** (1988), no. 8 728–731.
- [51] R. Winkler, *Spin Orbit Coupling Effects in Two-Dimensional Electron and Hole Systems*. Springer, Berlin, 2003.
- [52] Y. Oreg, G. Refael, and F. von Oppen, *Helical Liquids and Majorana Bound States in Quantum Wires*, *Physical Review Letters* **105** (oct, 2010) 177002.
- [53] J. D. Sau, S. Tewari, and S. Das Sarma, *Experimental and materials considerations for the topological superconducting state in electron- and hole-doped semiconductors: Searching for non-Abelian Majorana modes in 1D nanowires and 2D heterostructures*, *Physical Review B* **85** (feb, 2012) 064512.
- [54] B. A. Bernevig, T. L. Hughes, and S.-C. Zhang, *Quantum spin Hall effect and topological phase transition in HgTe quantum wells.*, *Science (New York, N.Y.)* **314** (dec, 2006) 1757–61.
- [55] A. Das, Y. Ronen, Y. Most, Y. Oreg, M. Heiblum, and H. Shtrikman, *Zero-bias peaks and splitting in an AlInAs nanowire topological superconductor as a signature of Majorana fermions*, *Nature Physics* **8** (nov, 2012) 887–895.
- [56] I. Knez, C. T. Rettner, S.-H. Yang, S. S. Parkin, L. Du, R.-R. Du, and G. Sullivan, *Observation of Edge Transport in the Disordered Regime of Topologically Insulating InAs/GaSb Quantum Wells*, *Physical Review Letters* **112** (jan, 2014) 026602.
- [57] J. D. Sau, S. Tewari, R. M. Lutchyn, T. D. Stanescu, and S. Das Sarma, *Non-Abelian quantum order in spin-orbit-coupled semiconductors: Search for topological Majorana particles in solid-state systems*, *Physical Review B* **82** (dec, 2010) 214509.
- [58] A. Gold, *Electronic transport properties of a two-dimensional electron gas in a silicon quantum-well structure at low temperature*, *Physical Review B* **35** (1987), no. 2 723–733.
- [59] Y. Li, Y. Zhang, and Y. Zeng, *Electron mobility in modulation-doped AlSb/InAs quantum wells*, *Journal of Applied Physics* **109** (2011), no. 7 073703.
- [60] Y. Zhang, Y. Zhang, M. Guan, L. Cui, C. Wang, and Y. Zeng, *Theoretical study of transport property in InAsSb quantum well heterostructures*, *Journal of Applied Physics* **114** (2013), no. 2013.

- [61] S. Das Sarma and F. Stern, *No Title*, *Physical Review B* **32** (1985), no. 12.
- [62] S. Brosig, K. Ensslin, B. Brar, M. Thomas, and H. Kroemer, *Scattering mechanisms in InAsAlSb quantum wells*, *Physica E: Low-dimensional Systems and Nanostructures* **2** (1998) 214–217.
- [63] T. Ando, A. B. Fowler, and F. Stern, *Electronic properties of two-dimensional systems*, *Reviews of Modern Physics* **54** (1982), no. 2 437–672.
- [64] S. Ideshita, A. Furukawa, Y. Mochizuki, and M. Mizuta, *Electron accumulation in AlGaSb-InAs-AlGaSb quantum well system*, *Applied Physics Letters* **60** (1992), no. 20 2549–2551.
- [65] P. T. Coleridge, *Small-angle scattering in two-dimensional electron gases*, *Physical Review B* **44** (1991), no. 8 3793.
- [66] E. O. Kane, *Band structure of indium antimonide*, *Journal of Physics and Chemistry of Solids* **1** (1957) 249–261.
- [67] D. Jena, A. C. Gossard, and U. K. Mishra, *Dislocation scattering in a two-dimensional electron gas*, *Applied Physics Letters* **76** (2000), no. 13 1707.
- [68] M. J. Manfra, L. N. Pfeiffer, K. W. West, H. L. Stormer, K. W. Baldwin, J. W. P. Hsu, D. V. Lang, and R. J. Molnar, *High-mobility AlGaIn/GaN heterostructures grown by molecular-beam epitaxy on GaN templates prepared by hydride vapor phase epitaxy*, *Applied Physics Letters* **77** (2000), no. May 2888.
- [69] M. L. Huang, Y. C. Chang, C. H. Chang, T. D. Lin, J. Kwo, T. B. Wu, and M. Hong, *Energy-band parameters of atomic-layer-deposition Al₂O₃/InGaAs heterostructure*, *Applied Physics Letters* **89** (2006), no. 1 012903.
- [70] E. H. Hwang and S. Das Sarma, *Limit to two-dimensional mobility in modulation-doped GaAs quantum structures: How to achieve a mobility of 100 million*, *Physical Review B - Condensed Matter and Materials Physics* **77** (2008), no. 23 4–9, [arXiv:0804.4684].
- [71] A. C. H. Rowe, J. Nehls, and R. A. Stradling, *Origin of beat patterns in the quantum magnetoresistance of gated InAs/GaSb and InAs/AlSb quantum wells*, *Physical Review B* **63** (2001), no. 20 201307–1–4.
- [72] R. Dingle, H. L. Stormer, A. C. Gossard, and W. Wiegmann, *Electron mobilities in modulation-doped semiconductor heterojunction superlattices*, *Applied Physics Letters* **33** (1978), no. 7 665–667.
- [73] J. P. Eisenstein, K. B. Cooper, L. N. Pfeiffer, and K. W. West, *Insulating and Fractional Quantum Hall States in the First Excited Landau Level*, *Physical Review Letters* **88** (2002), no. 7 076801.

- [74] V. Umansky, M. Heiblum, Y. Levinson, J. Smet, J. N?bler, and M. Dolev, *MBE growth of ultra-low disorder 2DEG with mobility exceeding 35??106 cm²/V s*, *Journal of Crystal Growth* **311** (2009), no. 7 1658–1661.
- [75] J. D. Watson, S. Mondal, G. A. Csáthy, M. J. Manfra, E. H. Hwang, S. Das Sarma, L. N. Pfeiffer, and K. W. West, *Scattering mechanisms in a high-mobility low-density carbon-doped (100) GaAs two-dimensional hole system*, *Phys. Rev. B* **83** (2011), no. 24 241305, [arXiv:1105.2808].
- [76] S. Datta and B. Das, *Electronic analog of the electro-optic modulator*, *Applied Physics Letters* **56** (feb, 1990) 665–667.
- [77] I. Žutić, J. Fabian, and S. D. Sarma, *Spintronics: Fundamentals and applications*, *Reviews of Modern Physics* **76** (2004), no. 2 323–410, [0405528].
- [78] D. D. Awschalom and M. E. Flatte, *Challenges for semiconductor spintronics*, *Nature Physics* **3** (2007) 153–159.
- [79] J. D. Sau, R. M. Lutchyn, S. Tewari, and S. D. Sarma, *Generic New Platform for Topological Quantum Computation Using Semiconductor Heterostructures*, *Physical Review Letters* **104** (2010), no. 4 040502–1–040502–4.
- [80] J. Alicea, *Majorana fermions in a tunable semiconductor device*, *Physical Review B* **81** (2010), no. 12 125318.
- [81] M. M. Uddin, H. W. Liu, K. F. Yang, K. Nagase, K. Sekine, C. K. Gaspe, T. D. Mishima, M. B. Santos, and Y. Hirayama, *Gate depletion of an InSb two-dimensional electron gas*, *Applied Physics Letters* **103** (2013), no. 12 123502.
- [82] A. H. Aifer and S. I. Maximenko, *US 20122715 A1, US 20122715 A1* (2013).
- [83] R. K. Jana and D. Jena, *Stark-effect scattering in rough quantum wells*, *Applied Physics Letters* **99** (2011), no. 2011 1–4, [arXiv:1105.4173].
- [84] G. Bastard, *Energy levels and alloy scattering in InP-In (Ga)As heterojunctions*, *Applied Physics Letters* **43** (1983), no. 6 591–593.
- [85] F. Stern and W. E. Howard, *Properties of semiconductor surface inversion layers in the electric quantum limit*, *Physical Review* **163** (1967), no. 3 816–835.
- [86] C. R. Bolognesi, H. Kroemer, and J. H. English, *Interface roughness scattering in InAs/AlSb quantum wells*, *Applied Physics Letters* **61** (1992), no. 1992 213–215.
- [87] K. Suzuki, Y. Harada, F. Maeda, K. Onomitsu, T. Yamaguchi, and K. Muraki, *Gate Operation of InAs/AlGaSb Heterostructures with an Atomic-Layer-Deposited Insulating Layer*, *Applied Physics Express* **4** (dec, 2011) 125702.

- [88] J. Shen, H. Goronkin, J. D. Dow, and S. Y. Ren, *Tamm states and donors at InAs/AlSb interfaces*, *Journal of Applied Physics* **77** (1995), no. 4 1576.
- [89] D. Åberg, P. Erhart, A. J. Williamson, and V. Lordi, *Intrinsic point defects in aluminum antimonide*, *Physical Review B* **77** (2008), no. 16 165206.
- [90] P. Erhart, D. Åberg, and V. Lordi, *Extrinsic point defects in aluminum antimonide*, *Physical Review B* **81** (2010), no. 19 195216.
- [91] A. Manchon, H. C. Koo, J. Nitta, S. M. Frolov, and R. A. Duine, *New perspectives for Rashba spinorbit coupling*, *Nature Materials* **14** (2015), no. 9 871–882.
- [92] P. Debray, S. M. S. Rahman, J. Wan, R. S. Newrock, M. Cahay, A. T. Ngo, S. E. Ulloa, S. T. Herbert, M. Muhammad, and M. Johnson, *All-electric quantum point contact spin-polarizer.*, *Nature nanotechnology* **4** (2009), no. 11 759–764.
- [93] M. Kohda, S. Nakamura, Y. Nishihara, K. Kobayashi, T. Ono, J.-i. Ohe, Y. Tokura, T. Mineno, and J. Nitta, *Spin-orbit induced electronic spin separation in semiconductor nanostructures*, *Nature Communications* **3** (2012), no. May 1–8.
- [94] S. Nadj-Perge, S. M. Frolov, E. P. A. M. Bakkers, and L. P. Kouwenhoven, *Spin-orbit qubit in a semiconductor nanowire.*, *Nature* **468** (2010), no. 7327 1084–1087, [arXiv:1011.0064].
- [95] K. D. Petersson, L. W. McFaul, M. D. Schroer, M. Jung, J. M. Taylor, A. A. Houck, and J. R. Petta, *Circuit quantum electrodynamics with a spin qubit*, *Nature* **490** (2012), no. 7420 380–383, [1205.6767].
- [96] J. Wunderlich, B.-G. Park, A. C. Irvine, L. P. Zârbo, E. Rozkotová, P. Nemeč, V. Novák, J. Sinova, and T. Jungwirth, *Spin Hall effect transistor.*, *Science (New York, N.Y.)* **330** (2010) 1801–1804.
- [97] P. Chuang, S. C. Ho, L. W. Smith, F. Sfigakis, M. Pepper, C. H. Chen, J. C. Fan, J. P. Griffiths, I. Farrer, H. E. Beere, G. A. C. Jones, D. A. Ritchie, and T. M. Chen, *All-electric all-semiconductor spin field-effect transistors*, *Nature Nanotechnology* **10** (2014), no. 1 35–39.
- [98] J. Nitta, T. Akazaki, H. Takayanagi, and T. Enoki, *Gate Control of Spin-Orbit Interaction in an Inverted In_{0.53}Ga_{0.47}As/In_{0.52}Al_{0.48}As Heterostructure*, *Physical Review Letters* **78** (feb, 1997) 1335–1338.
- [99] D. Grundler, *Large Rashba splitting in InAs quantum wells due to electron wave function penetration into the barrier layers.*, *Physical review letters* **84** (jun, 2000) 6074–6077.

- [100] T. Koga, J. Nitta, T. Akazaki, and H. Takayanagi, *Rashba Spin-Orbit Coupling Probed by the Weak Antilocalization Analysis in InAlAs/InGaAs/InAlAs Quantum Wells as a Function of Quantum Well Asymmetry*, *Physical Review Letters* **89** (jul, 2002) 046801.
- [101] J. B. Miller, D. M. Zumbühl, C. M. Marcus, Y. B. Lyanda-Geller, D. Goldhaber-Gordon, K. Campman, and a. C. Gossard, *Gate-controlled spin-orbit quantum interference effects in lateral transport.*, *Physical review letters* **90** (2003), no. 7 076807, [0206375].
- [102] J. P. Heida, B. J. van Wees, J. J. Kuipers, T. M. Klapwijk, and G. Borghs, *Spin-orbit interaction in a two-dimensional electron gas in a InAs/AlSb quantum well with gate-controlled electron density*, *Physical Review B* **57** (may, 1998) 11911–11914.
- [103] S. Brosig, K. Ensslin, R. Warburton, C. Nguyen, B. Brar, M. Thomas, and H. Kroemer, *Zero-field spin splitting in InAs-AlSb quantum wells revisited*, *Physical Review B* **60** (nov, 1999) R13989–R13992.
- [104] D. Nečas and P. Klapetek, *Gwyddion: an open-source software for SPM data analysis*, *Central European Journal of Physics* **10** (2012), no. 1 181–188.
- [105] P. T. Coleridge, R. Stoner, and R. Fletcher, *Low-field transport coefficients in GaAs/Ga_{1-x}Al_xAs heterostructures*, *Phys. Rev. B* **39** (1989), no. 2 1120–1124.
- [106] V. L. Gurevich and Y. A. Firsov, *On the theory of the electrical conductivity of semiconductors in a magnetic field*, *Journal of Experimental and Theoretical Physics* **13** (1961), no. 1 137–146.
- [107] D. C. Tsui, T. Englert, A. Y. Cho, and A. C. Gossard, *Observation of magnetophonon resonances in a two-dimensional electronic system*, *Phys. Rev. Lett.* **44** (1980), no. 5 341–344.
- [108] M. A. Zudov, I. V. Ponomarev, A. L. Efros, R. R. Du, J. A. Simmons, and J. L. Reno, *New class of magnetoresistance oscillations: Interaction of a two-dimensional electron gas with leaky interface phonons*, *Physical Review Letters* **86** (2001), no. 16 3614–3617, [0005036].
- [109] M. Raikh and T. Shahbazyan, *Magnetointersubband oscillations of conductivity in a two-dimensional electronic system*, *Physical Review B* **49** (1994), no. 8 5531–5540.
- [110] T. H. Sander, S. N. Holmes, J. J. Harris, D. K. Maude, and J. C. Portal, *Determination of the phase of magneto-intersubband scattering oscillations in*

- heterojunctions and quantum wells*, *Physical Review B* **58** (1998), no. 20 13856–13862.
- [111] G. Engels, J. Lange, T. Schapers, and H. Luth, *Experimental and theoretical approach to spin splitting in modulation-doped InGaAs-InP quantum wells for $B > 0$* , *Physical Review B* **55** (1997), no. 4 1958–1961.
- [112] E. A. de Andrada e Silva, G. C. La Rocca, and F. Bassani, *Spin-split subbands and magneto-oscillations in III-V asymmetric heterostructures*, *Phys. Rev. B* **50** (1994), no. 12 8523–8533.
- [113] I. Knez, R. R. Du, and G. Sullivan, *Evidence for helical edge modes in inverted InAs/GaSb quantum wells*, *Physical Review Letters* **107** (2011), no. 13 1–5, [arXiv:1105.0137].
- [114] L. Du, I. Knez, G. Sullivan, and R.-R. Du, *Robust Helical Edge Transport in Gated InAs/GaSb Bilayers*, *Physical Review Letters* **114** (2015), no. 9 096802.
- [115] K. Suzuki, Y. Harada, K. Onomitsu, and K. Muraki, *Edge channel transport in the InAs/GaSb topological insulating phase*, *Physical Review B - Condensed Matter and Materials Physics* **87** (2013), no. 23 1–6, [arXiv:1306.4234].
- [116] W. Pan, J. F. Klem, J. K. Kim, M. Thalakulam, M. J. Cich, and S. K. Lyo, *Chaotic quantum transport near the charge neutrality point in inverted type-II InAs/GaSb field-effect transistors*, *Applied Physics Letters* **102** (2013), no. 3 0–4, [arXiv:1204.0561].
- [117] J. I. Väyrynen, M. Goldstein, Y. Gefen, and L. I. Glazman, *Resistance of helical edges formed in a semiconductor heterostructure*, *Physical Review B - Condensed Matter and Materials Physics* **90** (2014), no. 11 115309, [arXiv:1406.6052].
- [118] L. Cooper, N. Patel, V. Drouot, E. Linfield, D. Ritchie, and M. Pepper, *Resistance resonance induced by electron-hole hybridization in a strongly coupled InAs/GaSb/AlSb heterostructure*, *Physical Review B* **57** (may, 1998) 11915–11918.
- [119] F. Qu, A. J. a. Beukman, S. Nadj-Perge, M. Wimmer, and B.-m. Nguyen, *Electric and Magnetic Tuning Between the Trivial and Topological Phases in InAs / GaSb Double Quantum Wells*, *Arxiv preprint* (2015) 1–7, [arXiv:1502.0571].
- [120] M. Knap, J. D. Sau, B. I. Halperin, and E. Demler, *Transport in two-dimensional disordered semimetals*, *Physical Review Letters* **113** (2014), no. 18 1–5, [arXiv:1405.0277].
- [121] B. J. Van Wees, G. I. Meijer, J. J. Kuipers, T. M. Klapwijk, W. Van De Graaf, and G. Borghs, *Breakdown of the quantum Hall effect in InAs/AlSb quantum wells due to counterflowing edge channels*, *Physical Review B* **51** (1995), no. 12 7973–7976.

- [122] V. Tripathi and M. P. Kennett, *Magnetotransport in disordered delta-doped heterostructures*, *Physical Review B - Condensed Matter and Materials Physics* **74** (2006), no. 19 1–9, [0607263].
- [123] L. Fu and C. L. Kane, *Topology, delocalization via average symmetry and the symplectic anderson transition*, *Physical Review Letters* **109** (2012), no. 24 1–5, [arXiv:1208.3442].
- [124] I. Lo, W. Mitchell, M. Manasreh, and C. Stutz, *Negative persistent photoconductivity in the Al Ga Sb/InAs quantum wells*, *Appl. Phys. Lett* **60** (1992), no. February 751–753.
- [125] G. C. Gardner, S. Fallahi, J. D. Watson, and M. J. Manfra, *Modified MBE hardware and techniques and role of gallium purity for attainment of two dimensional electron gas mobility >35106 cm²/V s in AlGaAs/GaAs quantum wells grown by MBE*, *Journal of Crystal Growth* **441** (2016) 71–77.
- [126] M. J. Uren, D. J. Day, and M. J. Kirton, *1/f and random telegraph noise in silicon metal-oxide-semiconductor field-effect transistors*, *Appl. Phys. Lett.* **47** (1985) 1195.
- [127] M. J. Kirton and M. J. Uren, *Noise in solid-state microstructures: A new perspective on individual defects, interface states and low-frequency (1/f) noise*, *Advances in Physics* **38** (1989), no. 4 367–468.
- [128] D. K. Ferry, *Alloy scattering in ternary III-V compounds*, *Physical Review B* **17** (1978), no. 2 912–913.
- [129] S. M. Sze and K. K. Ng, *Physics of Semiconductor Devices*. John Wiley and Sons, Inc., Hoboken, 3 ed., 2007.
- [130] A. Wallash, J. Hillman, M. Sharma, and S. X. Wang, , *IEEE Transactions on Magnetism* **36** (2000), no. 5.
- [131] P. Horowitz and W. Hill, *The Art of Electronics*. Cambridge University Press, Cambridge, 2 ed., 1989.